X-Ray Optical Diagnostic of Laser Produced Plasmas for Nuclear Fusion and X-Ray Lasers

DISSERTATION

zur Erlangung des akademischen Grades

doctor rerum naturalium (Dr. rer. nat.)

vorgelegt dem Rat der Physikalisch-Astronomischen Fakultät der
Friedrich-Schiller-Universität Jena

von Dipl.-Phys. Randolf Butzbach
geboren am 16.02.1969 in Kassel

Gutachter:

1. Prof. Dr. E. FÖRSTER
2. Prof. Dr. U. SCHUMACHER
3. Prof. Dr. G. DRÄGER

Eingereicht am: 23. Oktober 2000

Prüfungstermine: 15. und 21. Dezember 2000

Tag der öffentlichen Verteidigung: 4. Januar 2001

For my parents
and Cecília

Zusammenfassung

In der vorliegenden Arbeit werden Konzeption, Einsatz und Anwendung von torisch gebogenen Kristallen für die röntgenoptische Untersuchung von laserproduzierten Plasmen zur lasergetriebenen Kernfusion sowie zur verstärkten spontanen Emission („Röntgenlaser“) nahe dem sogenannten Wasserfenster dargelegt. Aus den gewonnenen Daten können elementare Plasmaparameter bestimmt werden.

Der erste Teil der Arbeit stellt einen Beitrag zur Untersuchung von Rayleigh-Taylor-Instablitäten dar, die der gewünschten Verdichtung und Zündung des Brennstoffes der lasergetriebenen Kernfusion durch Trägheitseinschluss entgegenwirken.

Ziel dieses Teils der vorliegenden Arbeit war es, eine abbildende Röntgenoptik zu entwickeln, die den hohen Ansprüchen zur Beobachtung der Rayleigh-Taylor-Instabilitäten genügt, d.h. ein röntgenoptisches System zur zweidimensionalen monochromatischen Abbildung bei gleichzeitig hoher Lichtstärke, hoher Auflösung ($\lesssim 3\ \mu$m) sowie mindestens 400 μm Schärfentiefe. Die Optik sollte am Hochleistungslaser GEKKO XII am Institute of Laser Engineering (ILE) an der Universität Osaka/Japan im Rahmen des HIPER-Forschungsprogramms (High-Intensity Plasma Experimental Research) zum Einsatz kommen.

Grundlage dieser abbildenden Optik ist ein 7×7 mm^2 großer torisch gebogener Quarz Kristall, der bei einer Vergrößerung von zunächst $30\times$ und später $70\times$ verwendet werden soll.

Die Simulation der konstruierten Optik durch Strahlbahnverfolgungsrechnungen zeigt, daß mittels torisch gebogener Kristalle die geforderten Bedingungen nicht nur erreicht, sondern sogar übertroffen werden können: Die Rechnung ergibt eine zu erwartende Auflösung von $< 1\ \mu$m bei einer Kristallapertur von 3.5 mm und einer Vergrößerung von $30\times$.

Jedoch konnte der experimentelle Nachweis der geforderten Auflösung aufgrund

von erhöhten Anforderungen an die Justage und technischen Problemen in der zur Verfügung stehenden Strahlzeit am benötigten Hochleistungslaser noch nicht erfolgen. Die beste in dieser Arbeit nachgewiesene Auflosung war 6 μm.

Als Weiterführung der Arbeit zum Nachweis der theoretisch zu erwartenden Auflösung wird alternativ ein detailliert ausgearbeiteter Versuchsvorschlag unter Verwendung eines Röntgengenerators vorgestellt.

Der erste Teil dieser Arbeit schließt mit der qualitativen Diskussion der ersten erhaltenen Bilder der beobachteten Rayleigh-Taylor-Instabilitäten. Für eine detaillierte Auswertung der Daten ist einerseits die erhaltene Datenmenge zu gering und andererseits das Signal aufgrund von Problemen mit dem Lasersystem zu schwach.

Da einerseits die Untersuchung der Rayleigh-Taylor-Instabilitäten größte Wichtigkeit für die Fusionsforschung hat und andererseits die hier entwickelte Optik das „Herzstück“ des HIPER-Programms darstellt, wird diese Arbeit über das Ende des hier gegebenen Zeitrahmens hinaus weitergeführt. Es wird erwartet, daß die hier konstruierte Röntgenoptik wichtige Erkenntnisse für das Design von zukünftigen Brennstoffkapseln liefert.

Der zweite Teil dieser Arbeit beschäftigt sich mit der spektral und eindimensional räumlich aufgelösten Beobachtung von laserproduzierten Plasmen zur verstärkten spontanen Emission („Röntgenlaser“) nahe dem sogenannten Wasserfenster. Ziel der Arbeit war es, mittels eines abbildenden Röntgenspektrometers einen Zusammenhang zwischen der verstärkten Emission des nickelähnlichen $4d-4p$–Übergangs und der nickelähnlichen $4f-3d$ Resonanz nachzuweisen. Hierbei sollte das Röntgenspektrum entweder zeitlich oder eindimensional räumlich aufgelöst aufgezeichnet werden und aus den gewonnenen Daten sollten weitergehende plasmaphysikalische Fragestellungen wie Bestimmung der Elektronentemperatur und Elektronendichte in Abhängigkeit der räumlichen Position im Plasma erfolgen.

Dazu wurde ein abbildendes Spektrometer auf Basis von torisch gebogenen Kristallen entwickelt, welches entweder in Verbindung mit einer CCD-Kamera räumlich aufgelöste, aber zeitintegrierte Spektren lieferte oder in Verbindung mit einer Schmierbildkamera eine räumlich integrierte, aber zeitaufgelöste Aufzeichnung der Spektren ermöglichte.

Das Spektrometer wird für den verwendeten Arbeitsbereich von 5.7–6.4 Å vollständig durch Strahlbahnverfolgungsrechnungen in Bezug auf den Einfluß der Quellgröße, Auslenkung der Quelle aus der Beugungsebene sowie Größe der Kristallapertur charakterisiert, gefolgt von dem experimentellen Nachweis, daß die erreichbare Auflösung im vorliegenden Fall durch die Auflösung der CCD-Kamera begrenzt wird.

Das Spektrometer wurde durch Vergleich der beobachteten Linienpositionen von Al-Plasmen mit deren wohlbekannten Wellenlängen in-situ kalbriert. Aus dem Vergleich können die genauen geometrischen Abstände des Spektrometers erhalten werden, durch welche umgekehrt die Dispersionsrelation vollständig beschrieben werden kann. Wenn weiterhin eine kalibierte CCD-Kamera als Detektor verwendet wird, kann die absolute Anzahl der vom Plasma emittierten Photonen erhalten werden.

Die plasmaphysikalischen Experimente wurden ebenfalls am Hochleistungslaser GEKKO XII am ILE in Japanisch-Chinesisch-Französisch-Deutscher Zusammenarbeit durchgeführt. Die Experimente bestätigen den vermuteten Zusammenhang zwischen der Emission der $4f-3d$-Linie und der verstärkten Emission des $4d-4p$ Übergangs. Als optimale Pumplaserintensität wurde für Tantal (Ta) $\sim 1.5\times10^{15}$ W/cm^2 ermittelt; ein Vorpuls von 4 % erhöht die Ionisation in den Ni-ähnlichen Zustand um das bis zu 35–fache. Die weitergehende Auswertung der zeitlich und räumlich integrierten Spektren ergibt für Ta eine beobachtete Elektronentemperatur, die unabhängig von der Pumplaserintensität im Bereich von $(0.2-2.2)\times10^{15}$ W/cm^2 ~ 150 eV beträgt. Mögliche Ursachen für diese beobachtete konstante Temperatur werden diskutiert. Die Auswertung der Elektronendichte der Ta-Plasmen zeigt einen linearen Zusammenhang zwischen Pumplaserintensität und erreichter Dichte bei konstant gehaltener Plasmagröße.

Weiterhin konnte die Wellenlänge der $4f-3d$-Linien gemessen werden. Die Übereinstimmung der gemessenen Werte mit theoretischen Literaturwerten ist bei einer Abweichung von $\pm(<1\ldots10)$ mÅ, abhängig vom Autor und der Spektrallinie, sehr gut bis gut.

Die Auswertung der Daten zeigt, dass eine detaillierte Aussage über die Elektronentemperatur nur in Verbindung mit zeitaufgelösten Spektren möglich ist. Diese konnten jedoch in der zur Verfügung stehenden Strahlzeit bisher nicht gewonnen werden, sind aber für die nächste Experimentserie in voraussichtlich zwei Jahren geplant.

Contents

Introduction

High intense light amplification by stimulated emission of radiation opens the laboratory access to physical phenomena as they exist in the interior of stars. The interaction of high intense laser light with matter can cause the generation of a practically totally ionized gas which is called *Plasma* [1]. Even though this 'fourth state of matter' is an exception on earth, it is the most common state of matter in the nature [2]. The sun and the stars can be considered as an ensemble of plasmas.

Besides the pure fundamental research of the behavior of nature in this extreme region, it is possible to simulate astrophysical phenomena in the laboratory on a much smaller scale like the thermonuclear fusion process [3–8], the probable energy source of the stars, or the explosion of super novae [9–11]. The former one is particularly interesting since one expects to use the released energy of the fusion process once as a terrestrial energy source. To realize laser-driven nuclear fusion with energy gain, huge laser systems are required, which can deliver more than one mega-joule in several nanoseconds [12].

Another application of such large laser facilities required for the thermonuclear fusion is the quest for X-ray lasers [13–17] with emission line inside the so called water window, the region between the K–absorption edges of oxygen and carbon. This range is particularly interesting for biological applications: The absorption of the water, or more precisely, the oxygen in the water of biological solutions is relatively small while the carbon of the organic molecules absorb very well.

In all cases, the main emission from the laser produced plasma is in the X-ray regime [18, 19]. Therefore, X-ray diagnostics play a crucial role for the understanding of the plasma physics. By analyzing the emission or absorption spectra of the plasma, one can obtain information such as the electron temperature or electron density of the plasma [18, 19]. The electron temperature can be obtained for instance by measuring the intensity distribution of the spectral lines or by precisely measuring the wavelength of the emission line which is shifted due to the altered Coulomb potential of the atom [18, 19]. The distribution of the ionization state of atoms in the plasma causes the appearance of satellite lines near the emission line, from which again one can obtain the electron temperature [18–22].

The width of the spectral line is directly related to the life time of the excited state [18, 19], which in turn is shortened due to collisions with other particles: The higher the density of the plasma, the more likely is a collision, *i.e.* the broader the line becomes. Thus, the width of the line can be directly related to the density of the plasma [18, 19, 23–26].

In order to measure the line width or shift of the spectral lines, a high spectral resolution of about $\Delta\lambda/\lambda = 10^{-4}\ldots10^{-3}$ is required.

Other informations which might be obtained from the spectra are *e.g.* the detection of hot electrons by observing an un-shifted Kα-line, since hot electrons are a precondition for the emission of Kα photons from cold matter.

Moreover, the plasma dynamics can be studied by the spatially and temporally resolved observation of the emission lines from tracer atoms as markers of the different parts of the plasmas [27–30]. Thus, ideally the diagnostic instrument gives high spectral resolution combined with high spatial and high temporal resolution [27–31].

Among all imaging and spectral resolving elements like *e.g.* pinholes, gratings and Kirkpatrick-Baez microscopes, two-dimensionally bent crystals are best-suited [32–34]. While pinholes are simple devices and can give two-dimensional images of moderate ($\sim 5\ldots10\ \mu$m) spatial resolution [35], the luminosity is very poor and the images are polychromatic and thus cannot provide informations about the spectrum of the plasma.

Kirkpatrick-Baez microscopes [36] have a much higher luminosity than pinholes combined with a high spatial resolution of about $\leq 3\ \mu$m [37] and an under cut-off wavelength due to the use of specular reflection at large bent mirrors which collect the emitted photons over a large solid angle. But the spectral window, whose upper cut-off wavelength can be obtained by the use of filters, is still very large and therefore not suited for spectroscopy. An enhancement of the Kirkpatrick-Baez microscope can be obtained by using multilayer coating of the reflecting surfaces which acts as a Bragg diffractor [35, 38]. However, the spectral resolution is in the order of 1 keV [35], corresponding to $\Delta E/E \sim 0.2$ and depends strongly on slope errors of the surface [39].

Only two-dimensionally bent crystals can combine the large dispersion and thus high spectral resolution obtained at the diffraction of X-rays at crystals with one- or two-dimensional focusing at large ($\sim 0.1 \ldots 10$ msr) aperture sizes and thus very bright spectra and/or imaging of the source: Either two-dimensional (2-D) high ($\lesssim 3\,\mu$m) spatial resolution in one narrow spectral channel ($\Delta\lambda/\lambda = 10^{-2} \sim 10^{-4}$) or 1–D spatial- and spectral ($\Delta\lambda/\lambda \sim 10^{-4}$) resolution can be obtained. The temporal resolution can be obtained by using streak- and framing cameras with respectively sub-picosecond [40] and ~ 40 ps [31, 41] temporal resolution as a detector, or by a short pulse plasma as a 'speed light' for shadowgraphy.

In the present work toroidally bent crystal systems were applied to two different experiments: The high spatially resolved observation of the growth of Rayleigh-Taylor instabilities, which are a harmful effect for the compression and ignition of the fusion capsule in the inertial confinement fusion process (Chapter 1) and the diagnostic of the lasing plasma of a collisional X-ray laser with the aim of obtaining lasing inside the so-called water window (Chapter 2). For both experiments, a particular optical instrument was designed and constructed which fits the particular requirements of the experiment.

These experiments can be only carried out at large laser systems such as NOVA in Livermore/USA, PHEBUS in Limeil/France or, like here, GEKKO XII in Osaka/Japan in combination with toroidally bent crystals. The beam time at such large laser facilities is very limited due to the large number of research issues and a low repetition rate of the laser due to the required cooling time: The repetition rate of GEKKO XII, for instance, is only one shot per two hours. Thus, there are at most four shots per day possible. The time required for setting up the experiment and alignment as well as frequent problems with the laser system reduce the number of available shots to effective 2–3 shots per day. For normally, the quality of the data is influenced by several problems and there is no possibility within two years to repeat an experiment under improved conditions. Since only the most important research issues have a chance to get a second time beam time allocated, the data obtained at these large facilities (and presented in this work) are unique, even though their quality might be reduced.

On the other hand, only the X-ray optics group at the University of Jena is currently able to manufacture toroidally bent crystals with a sufficiently high quality, *i.e.* an error in the bending radii of $\Delta R/R \sim 10^{-3}$. The independent control over both bending radii offers the possibility to design the optical instrument according to the experimental requirements. As a result, a high spatial resolution in both, the sagittal and meridional plane at large aperture sizes [30, 31, 34] and thus high luminosity (*cf.* Ch. 1) might be obtained. Also, it is possible to design a highly resolving 1–D imaging spectrometer for the operation at a distance of more than 1 m from the plasma source, which might be used in combination with a streak camera (*cf.* Ch. 2). Since these features are a precondition for the experiments presented in this work as well as the requirement of a large laser system, these experiments are unique in the world.

Chapter 1

Studies on Hydrodynamic Instabilities

1.1 Introduction

1.1.1 Inertial Confinement Fusion

The fusion of deuterium (D) and tritium (T), two heavier isotopes of hydrogen (H), produce helium plus a neutron and releases 2.85×10^{-12} J or 17.6 MeV of energy. Even if this number on its own appears very small, it is about 10 000 000 times more than the chemical binding energy, and, when scaled to macroscopic numbers, the enormous energy becomes obvious: 1 mg DT releases 340 MJ, this is equivalent to 85 kg TNT [12]. Since in normal water one Deuterium atom comes with every 5500 normal Hydrogen atoms, one can obtain from one liter normal water the fusion energy equivalent of 300 liter of gasoline [4]. Thus the oceans keep an energy reservoir for 100 billion years (assuming the present energy consumption and an exclusive use of fusion energy) [42]. Moreover, fusion energy is a ‘clean’ energy: The waste product is the nobel gas Helium.

To start the fusion process, one has to bring the nuclei close enough together so that the strong interaction of the nuclei can act. However, both fusion nuclei are positively charged, *i.e.* there are repulsive forces which have to be overcome before the nuclear forces can act.

The required energy of about 1 MeV to pass this ‘Coulomb-wall’ can be easily produced with particle accelerators. This so-called ‘neutron generator’ is available at research institutes as a ‘clean’ alternative to fission reactors for neutron research [43]. However, the efficiency of this scheme is by far too low that one could expect more

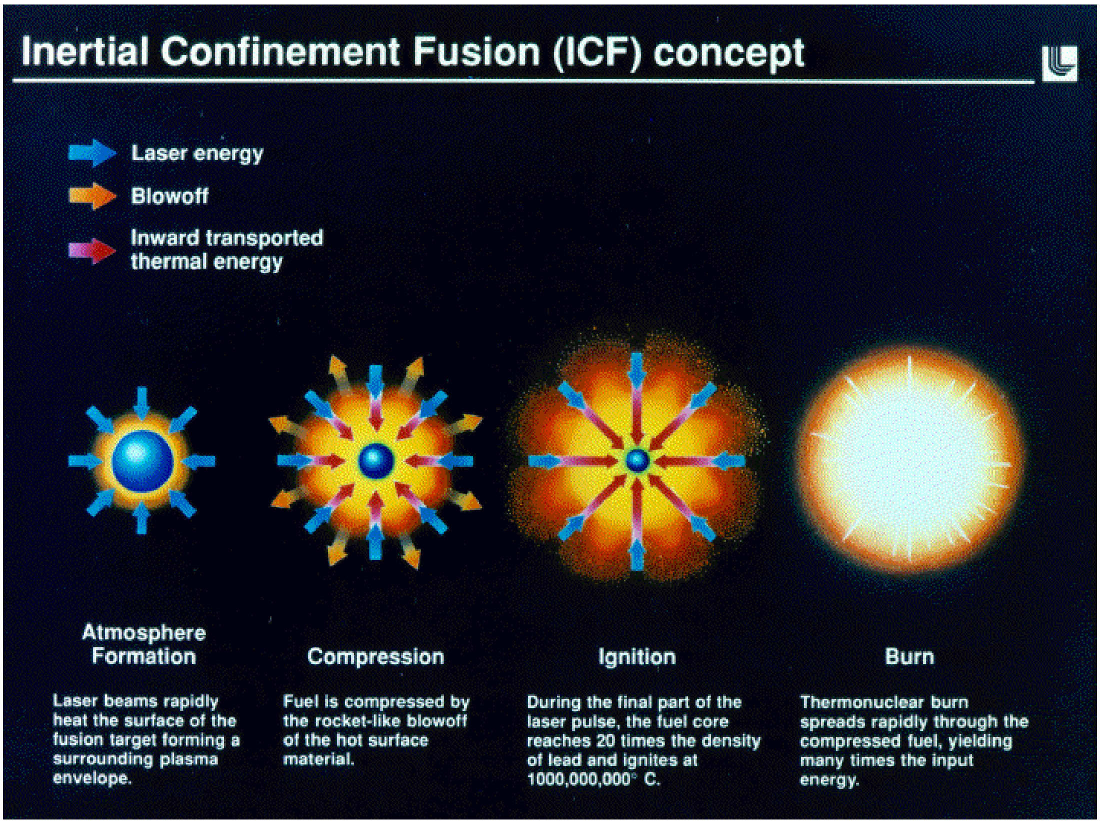

Inertial Confinement Fusion (ICF) concept

Laser energy

Blowoff

Inward transported thermal energy

Atmosphere Formation

Laser beams rapidly heat the surface of the fusion target forming a surrounding plasma envelope.

Compression

Fuel is compressed by the rocket-like blowoff of the hot surface material.

Ignition

During the final part of the laser pulse, the fuel core reaches 20 times the density of lead and ignites at 1000,000,000° C.

Burn

Thermonuclear burn spreads rapidly through the compressed fuel, yielding many times the input energy.

Figure 1.1. The concept of Inertial Confinement Fusion (LLNL diagram).

released energy from the fusion than required to start the fusion process [4].

A more efficient scheme, which would allow fusion on a larger scale, is to heat the fuel to sufficiently high temperatures (10–100 keV). At this relatively low energy, the tunnel probability is already sufficiently high. However, the particles will be scattered from each other and only very rarely, one particle will tunnel through the Coulomb wall [4]. Therefore one has to increase the tunnel probability by increasing the particle density n by confinement for a long confinement time τ. The product $n\tau$ is a measure for the scientific feasibility of the reaction, and the threshold value at which ignition is possible, is called ‘Lawson-criterium’. For DT, *e.g.* , $n\tau > 10^{14}$ s/cm^3. Inside the stars, the confinement is ensured by the large gravitational force, which is much too low on earth. For man-made fusions, one has to find other means of confinement [4].

One way is to try to get large confinement times, *i.e.* about 1 second, in a storage ring so called magnetic fusion. The nuclei are accelerated in a particle accelerator and circulate in a storage ring. On their trajectory the nuclei are focused, *i.e.* confined, via magnetic fields by the Lorentz-force. However, to reach such high confinement times, one has to correct all higher order trajectory 'errors' in these so called *tokamaks*, which leads to complicated magnetic fields and trajectories [6].

Another approach to fulfill the Lawson criterium is to use high particle densities, but low confinement times. *I.e.* one compresses the fuel to the required density so that the fuel ignites and burns before the particles separate again. Since one uses the inertia for the confinement, one speaks of *Inertial Confinement Fusion* (ICF). On a large scale, this scheme has been demonstrated successfully in 1950 in the Hydrogen Bomb, where the compression is done by 'conventional' A-bombs [44].

Immediately after the invention of the laser by Mayman in 1960, Nuckolls *et al.* proposed in 1961 [3, 6] to use lasers for the realization of the ICF scheme on a much smaller scale: A hollow shell of frozen D–T fuel is filled with low density D–T gas (≤ 10 mg/cm^3) and covered by a plastic layer, the so called ablator. Now, one shoots with high-power lasers onto the ablator, which expands rapidly in a low density plasma and accelerates the fuel shell rocket-like to the center of the sphere. At the collision at the center of the fusion capsule, the kinetic energy of the imploding shell is converted to inner (thermal) energy, which heats the fuel to the fusion temperature. The fuel ignites in a small spot, the so called 'hot spark'. The energy of the α-particles produced in the hot spot will be deposited in the fuel and heats up the fuel further: The fuel will burn self-substaining.

To give some rough numbers for energy gain conditions [12] in order to achieve a hot spot, the shell has to be accelerated within the capsule radius to a velocity, *i.e.* a specific energy, of $v \approx 3 \times 10^7$ cm/s. For 3 mg fuel, this corresponds to 135 kJ kinetic energy of the shell. Assuming a coupling efficiency of 10 % between the driver laser and the shell, the driver laser has to deliver 1.35 MJ. For an assumed initial shell radius $R_0 = 1$ mm this energy has to be delivered in 7 ns, corresponding to an acceleration of 4×10^{15} cm/s^2 and an average power delivered to the fuel of 19×10^{12} W, or an average driver power of 190×10^{12} W. The new laser facilities like the National Ignition Facility (NIF) at Lawrence Livermore National Laboratory in California/USA or the Laser MegaJoule project (LMJ) in France will be able to deliver 1.8 MJ in 192 and 240 beams from 2002 and 2012 on, respectively [45]. Thus these facilities will be able to meet the requirements for energy gain.

Another critical point in order to achieve compression is that one has to make sure that the driving forces are well balanced, *i.e.* that the sum of the forces with respect to the center of mass vanishes. Otherwise, the center of mass is accelerated and the compression will not be sufficient to ignite the fuel [46, 47]. To realize the symmetric illumination of the ablator, two schemes are pursued: Direct drive and indirect drive.

In indirect drive, the fusion capsule is placed into a cavity (Hohlraum) made from gold for instance. The laser beams are directed to the inner walls of the cavity where they produce X-ray Hohlraumstrahlung. The (ideally) very homogeneous Hohlraumstrahlung then drives the fusion capsule. The advantage of this scheme is that it is relatively easy to obtain a homogeneous illumination of the target and the coupling efficiency for X-rays to the ablator is much better than for the direct laser light. However, the Hohlraumstrahlung is not ideal due to the entrance windows for the laser beams as well as observation windows for diagnostics. Also, the required laser intensity is higher, since the laser energy has to be first converted into X-rays before it can be used for the drive of the capsule.

In direct drive, the fusion capsule is illuminated directly by several laser beams. The advantage of this scheme is that the required laser intensity is less than in indirect drive, but there are much higher requirements to the laser beam optics: The beam profile has to be extremely smooth in order to avoid non-uniformities in the capsule surface due to laser imprint, which triggers Rayleigh-Taylor instabilities, which in turn can quench the ignition. Also, the laser energy in the different laser beams has to be very well balanced in order to ensure uniform compression [46, 47].

An alternative to the above described schemes was proposed by Tabak *et al.* in 1994 [48]. In this so-called ‘Fast Ignitor’ scheme, the fuel is conventionally compressed and then heated up further by an additional laser pulse in order to ignite the fuel.

1.1.2 Rayleigh–Taylor Instabilities

One of the most important issues in ICF research is hydrodynamic instability, in particular Rayleigh–Taylor instabilities, which play an essential role in the confinement process of inertial confinement fusion plasma:

Rayleigh–Taylor instabilities [49, 50] (RTI) occur when a high density fluid is accelerated against a fluid with a lower density. Classically it occur, for example when one tries to float a layer of water on top of a layer of lighter fluid such as oil. Carefully done it might be possible, but slight disturbance in the contact surface between water and oil will trigger oscillations of the contact surface that will grow until globs of oil begin to pass through the water to the surface under buoyancy forces $\vec{F}_a$ driven by gravity g.

In ICF we encounter a similar situation during the acceleration and deceleration of the shell: In the acceleration phase, the exploding light ablation plasma pushes the dense shell inward and in the stagnation phase, the light central plasma slows down the incoming denser material. In both cases, the inertial force of the shell acts like the buoyancy force in the example above while the acceleration and de-acceleration, respectively, act like the gravitation force.

The RTI can cause quenching of the ignition, since during the acceleration phase the RTI causes a mixing between the ablator and the main fuel while in the stagnation phase the RTI causes a mixing of the hot spark with the cold main fuel. A good understanding of the RTI and how to mitigate them are therefore mandatory. Thus the RTI is for the moment one of the main research issues in ICF research.

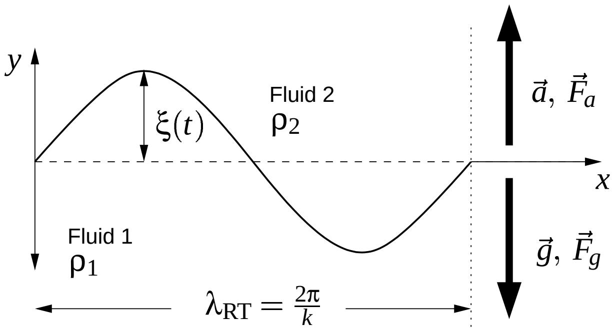

Figure 1.2. Definition of the Rayleigh–Taylor instability.

Classically, the RTI in the linear growth phase can be described by a consideration of the variation of the potential and kinematical energy (*cf. i.e.* [51]) which leads to the classical standard model

$$\xi(t) = \xi_0 \cdot e^{\gamma t}, \qquad (1.1)$$

where ξ is the perturbation amplitude from the equilibrium position and $\xi_0 \equiv \xi(t = 0)$ *i.e.* the initial amplitude of the non-uniformities at the interface between two liquids of different densities. t is the time and γ is the growth rate which can be expressed by

$$\gamma^2 = \underbrace{\frac{\rho_2 - \rho_1}{\rho_2 + \rho_1}}_{A} gk = Agk \qquad (1.2)$$

with the densities ρ_1 and ρ_2 of the two facing liquids, the acceleration g and the wave number $k = 2\pi/\lambda_{\mathrm{RT}}$, where λ_{RT} is the wavelength of the perturbation (*cf.* Fig. 1.2). A is called the Atwood number.

For $\rho_2 > \rho_1$ γ becomes positive and $\xi(t)$ grows exponentially: The system is unstable. For $\rho_1 > \rho_2$ γ^2 is negative, *i.e.* γ is imaginary and the $\xi(t)$ describes undamped oscillations.

However, in ICF, the situation is much more complicated than the classical model described by Eq. (1.2). The fuel is no longer incompressible and the (main fuel) layer has a finite thickness. The ablation process of the outer layer causes a mass- and heat flow as well as a density gradient. Also, the thermal conduction by radiation and energetic particles has to be taken into account. While Eq. (1.2) assumes a flat interface, in ICF a spherical convergence occurs. Also, in the simple classical model above, non-linear multiple wavelength effects like coupling, mixing and bubbles remain unconsidered as well as 3-D effects. The finite layer thickness of the fuel causes on the one hand a reduction of the growth rate [51–53] and on the other hand, synergetic effects between the RTI invoked at the ablation front and at the collapse: The RTI invoked at the ablation front due to outer surface roughness and non-uniformities in the laser beams, which imprints a drive-beam structure onto the surface, can feed-through the fuel and interfere with the RTI during the collapse from the roughness of the inner surface.

Nevertheless, all these effects can be summarized by a simple fit formula, the so called ‘Takabe-formula’ [54, 55]

$$\gamma = 0.9\sqrt{kg} - \beta k V_a \tag{1.3}$$

with the fit parameter $\beta = 3 - 4$ and the ablation velocity

$$V_a = \dot{m}/\rho_a \tag{1.4}$$

where ρ_a is the peak density at the ablation front and $\dot{m}$ is the areal mass ablation rate. The density gradient at the ablation front is so sharp ($\rho_1 \sim 1$, $\rho_2 \sim 10^{-4}$) that one may assume $A = 1$. Thus, the term Akg reduces to kg.

Equation (1.3) is intended for direct-drive experiments, but can be generalized as

$$\gamma = \sqrt{\frac{kg}{1+kL}} - \beta k V_a, \tag{1.5}$$

the so called ‘modified Takabe formula’ [56]. Here, $L = [\rho/(d\rho/dz)]_{\min}$ is the density gradient scale length in the ablation front.

More recently, Betti *et al.* [57] developed an improved model for RTI in the presence of ablation that obtains the density and velocity equilibrium profiles self consistently from a model of thermal conduction. The growth rates obtained from this model are in general complex, but have the same behavior as Eqs. (1.3) and (1.5).

Contrary to the classical growth rate, as described by Eq. (1.2), where γ increases with higher perturbation wave number k, the ablation causes a reduction of the growth rate [54] at higher perturbation wave numbers up to a cut-off wave number, where $\gamma = 0$ and no growth occurs as shown in Fig. 1.3.

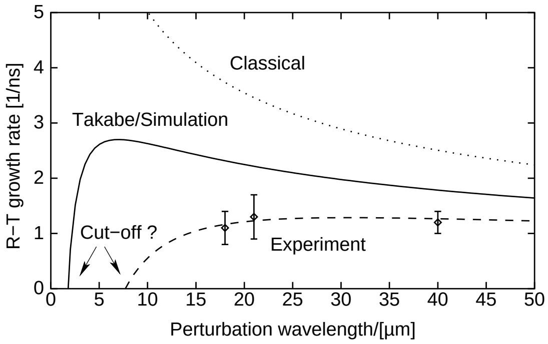

Figure 1.3. The growth rate of the Rayleigh–Taylor instability. The dotted line shows the classical growth rate (Eq. (1.2)), while the solid and dashed line show the growth rate from the Takabe formula (Eq. (1.3)) for the simulated RTI (ILESTA 1-D code) and experimental values (Ref. [58]), respectively.

Experimental values for β vary: Remington *et al.* [59] obtained in 1991 with indirect drive $\beta = 1-2$; Nakai *et al.* [60] obtained in 1992 with direct drive $\beta = 3$. Azechi *et al.* [61] obtained in 1997 at the ILE $\beta/\rho_a \sim 2.5$ cm^3/g or $\beta \sim 4$. Shigemori *et al.* [58] observed in 1997 a much stronger stabilization effect than predicted by Takabe *et al.* [55]: They measured $\beta/\rho_a = 2.6$ cm^3/g which gives $\beta = 6.5-9.1$ for a simulated ablation density $\rho_a = 3.5-2.5$ g/cm^3. Compared to the classical growth rate from Eq. (1.2) this gives $\gamma_{\text{exp}}/\gamma_{\text{class}} \approx 50\,\%$. Some of their experimental values are presented in Fig. 1.3 together with the classical growth rate and the expected growth rate from the ILESTA 1-D simulation code [62]. This stabilization is interpreted by nonlocal electrons that may penetrate deep into the target, thereby reducing the target density via pre-heating, and enhancing ablative stabilization [63]. Glendinning *et al.* [64] observed $\gamma_{\text{exp}}/\gamma_{\text{class}} \approx 50\,\%$, too, for very different experimental conditions: longer laser wavelength, lower laser intensity and higher target Z. Compared to their simulations, the observed growth rate is about 18 % lower than predicted.

Despite its great importance for ICF target design, all these experimental data show that the RTI are still not well understood: The growth rate measurements are still not conclusive, the physical origin of the fit parameter β is still unknown. It could be only demonstrated that there is a stabilizing effect which is much stronger than expected. Also, the predicted cut-off wavelength could not yet be observed which is primarily due to the technical difficulty of the experiment (*cf.* Sec. 1.1.3).

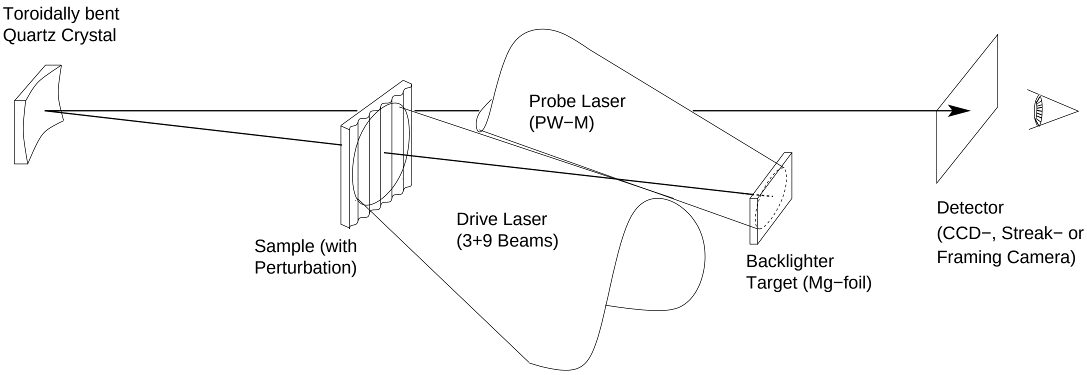

Figure 1.4. The generic experimental setup for the observation of Rayleigh-Taylor instabilities in the case of the present work.

The experiment presented here was intended to clarify the situation under the simulated conditions of future high-gain fusion capsules and to observe the cut-off wavelength, which is expected to be somewhere around $3 - 10\ \mu$m.

1.1.3 The principle layout of the experiment

The principle layout of all experiments for the observation of RTI is as follows (Fig. 1.4): One irradiates a planar sample target with laser light in order to create the plasma. Depending on the experiment itself, one provokes RTI *e.g.* by non-uniformities in the incident laser beam or by imposed non-uniformities on the surface of the sample. Another plasma is generated ‘behind’ the sample plasma as a backlighter source. By choosing an appropriate wavelength of the backlighting X-ray source, together with a monochromatic imaging optic, *i.e.* knowing the wavelength λ of the backlighter and the density of the plasma, one can obtain the optical thickness of the sample by measuring the transmitted intensity and compare it with the incident intensity: A variation of the thickness of the sample will cause a variation in the transmitted intensity. By acquiring the transmitted intensity at different times by using a framing- or streak camera or a short pulse backlighter at different times, one can obtain the growth rate γ.

The backlighter wavelength λ has to be chosen as a compromise between three constraints: For a precise observation of slight variations ($\sim \mu$m) of the thickness of the sample, one needs a high absorption coefficient and therefore a relatively large wavelength. However, the initial thickness of the sample is very thick compared to the thickness variations due to the RTI so that most of the intensity of the backlighter radiation will be absorbed in the main body of the sample. Thus, in order to increase the amount of transmitted photons, one would prefer a shorter wavelength in order to obtain a smaller absorption coefficient. In addition one needs a bright backlighter source, *i.e.* one needs to find an intense spectral line in the small range where the mass absorption coefficient is large enough to provide a precise observation of the RTI and small enough to ensure that sufficiently many photons are transmitted through the sample. In other words, when defining the transmission

$$T = \frac{I_{\text{trans}}}{I_{\text{inc}}} \times \exp(-\mu\rho t) \tag{1.6}$$

with the incident and transmitted intensity I_{inc} and I_{trans}, respectively, the mass absorption coefficient μ, the density ρ and the thickness t, μ should be selected as small as possible in order to get a large transmission T. However, for large 'resolution' of the thickness variations

$$\Delta T/T = -\mu \cdot \Delta(\rho t) \tag{1.7}$$

μ should be as large as possible. For an assumed thickness of the plastic sample of 50 μm, a thickness variation due to the Rayleigh-Taylor instabilities of $\sim 3\%$, and an absorption cross section of 2×10^{-20} cm^2 a suitable wavelength, which is small enough to pass the sample and large enough to give a reasonable contrast, the probe wavelength has to be around 9 Å. In this wavelength region the H-like ^{12}Mg Lyα emission line with a center transition wavelength of the H-like doublet of $\lambda = 8.42235$ Å is a suitable compromise between wavelength and high intensity [63].

Additionally, the imaging optic has to have a small energy bandpass in order to ensure that only the desired photon energy of the backlighter is detected and the self emission from the sample is suppressed [65, 66].

In summary, this sets high demands on the X-ray imaging system: The optic should provide a high spatial resolution of better than ~ 3 μm in order to resolve the expected cut-off perturbation wavelength, the image has to be monochromatic in order to have a well defined absorption coefficient, which enables a precise determination of the thickness variation, and to suppress the self-emission from the sample. Since the emission lines of the backlighting plasma have fixed discrete wavelengths, the spectral window of the optic should be chosen freely in order to match the selected spectral line. Moreover, the aperture of the optic should be as large as possible in order to focus as many as possible of the few transmitted photons on the detector.

Only two-dimensionally bent crystals can fulfill all of the above mentioned requirements at once [32, 33], and are thus suitable for the X-ray imager.

1.2 Monochromatic X-ray imager

1.2.1 Definition of resolution

Before describing the basics, design, and performance of the constructed imager for the observation of Rayleigh-Taylor instabilities, the (in this work omnipresent) term *resolution* should be defined:

The image of a point on the detector will be, due to imaging errors, not a point, but a complicate function, called *Point Spread Function*

$$\mathrm{PSF} = \mathrm{PSF}(x,y) \tag{1.8}$$

where x and y are orthogonal coordinates in a system with its origin at the image center. Using the point spread function as a starting point, we can calculate other descriptive functions in common use:

The *Line Spread Function* can be computed from the PSF according to [67]

$$\mathrm{LSF}(x) = \int_{-\infty}^{+\infty} \mathrm{PSF}(x,y)\, dy. \tag{1.9}$$

The LSF gives the result of scanning, in x-direction, over the image of a point source using a slit which has infinitesimal width and is infinitely long in y-direction. It is the response of the system to a line input [68].

A widely used form of characterization is the *Modulation Transfer Function,* given as the Fourier transform of the LSF [67]:

$$\mathrm{MTF}(k) = \frac{1}{2\pi} \int_{-\infty}^{+\infty} e^{-ikx}\, \mathrm{LSF}(x)\, dx \tag{1.10}$$

where k is the spatial frequency given by $2\pi/\lambda$ where λ is the period. The MTF describes the modulation of the image of a sinusoidal object as a function of the spatial frequency. One of its useful characteristics is that the MTF of a system is the product of the MTFs of the series system components [68]. Alternatively, we can define the *Contrast Transfer Function* as [69]

$$\mathrm{CTF}(\nu) = \frac{(\text{response max.} - \text{response min.})}{(\text{response max.} + \text{response min.})} \tag{1.11}$$

where the response maximum and minimum are those for the detector illuminated by a 100 % contrast bar pattern of spatial frequency ν line pairs per unit length. The MTF may then be expressed as [69]:

$$\mathrm{MTF}(\nu) = \frac{\pi}{4}(\mathrm{CTF}(\nu) + \mathrm{CTF}(3\nu)/3 - \mathrm{CTF}(5\nu)/5 + \mathrm{CTF}(7\nu)/7\ldots). \tag{1.12}$$

In the ideal case of an optical system having a Gaussian PSF, the resolution can be expressed by the $\mathrm{FWHM}(x) = 0.44/\nu_{50\,\%}$, where FWHM is the full width at half maximum of the Fourier transform of the MTF and $\nu_{50\,\%}$ is the spatial frequency in units of inverse length x^{-1} for which the MTF is 50 % [69].

Finally, the *Edge Spread Function*, defined as the response of the system to step function illumination, is given by [67]

$$\mathrm{ESF}(x) = \int_{-x}^{+\infty} \mathrm{LSF}(x')\, dx' \tag{1.13}$$

The step function source is assumed to have zero intensity for negative x and unit intensity for $x \geq 0$ [68].

All of these functional descriptions are interrelated mathematically. Thus, if any of them is measured, the data can be used to obtain the others [68].

In this work, the PSF is obtained by simulations, and the LSF is obtained by the integration of the PSF over one direction. In the following text, the term ‘profile’ is as a synonym for the LSF. To measure the resolution in the experiment, the image of an edge is considered. The integration over the edge gives the ESF and its derivative again the LSF. Thus, in this work, the full width at half maximum of the LSF obtained in the simulation and the experiment is used for comparison. Unless otherwise stated, this FWHM is used as a definition of the resolution.

1.2.2 Two-dimensional imaging using bent crystals

For the high-resolution observation of the plasma instabilities, a new X-ray crystal camera, based on a toroidally bent crystal, was designed to fit the requirements of a high resolution microscopy.

The imaging at concave mirrors with circular bending can be described by the well-known lens equation [70]

$$\frac{1}{f} = \frac{1}{a} + \frac{1}{b} \tag{1.14}$$

where f, a and b are the focal length, the object distance and the image distance, respectively. In the sagittal plane, the focal length can be described by [70]

$$f_s = \frac{R_s}{2\sin\theta} \tag{1.15}$$

and in the meridional plane approximately by [70]

$$f_m = \frac{R_m}{2}\sin\theta. \tag{1.16}$$

Here, R_s and R_m is the bending radius in sagittal and meridional plane, respectively, and θ the angle of incidence, measured to the surface.

In order to obtain a two-dimensional image, the focal length in meridional plane f_m has to be equal to the focal length in sagittal plane f_s, which is the case if

$$\sin\theta = \sqrt{\frac{R_s}{R_m}}, \tag{1.17}$$

i.e. for an angle of incidence $< 90°$, both bending radii have to be different, which leads us to the toroidal shape of the mirror (crystal).

When using a crystal for ‘reflection’, the angle of incidence θ has to be equal to the Bragg-angle θ_B, which is given by the Bragg equation [71, 72]

$$2d\sin\theta_B = n\lambda \tag{1.18}$$

with the interplanar lattice spacing d of the crystal, the X-ray wavelength λ and n is an integer number.

The spectral window of the crystal can be estimated by [73]

$$\frac{\Delta\lambda}{\lambda} = \left|\frac{M-1}{M+1}\right| \frac{A_m}{R_m\tan\theta} \tag{1.19}$$

where $M = b/a$ is the magnification of the image and A_m is the aperture (size) of the crystal in meridional plane. This estimation excludes the influence of the reflection curve and the source size. Also, Eq. (1.19) is not valid for the case $M = 1$, which would give a spectral window of $\Delta\lambda = 0$. Thus, by changing the aperture size of the crystal in meridional plane, one can control the band width of the reflected X-rays, which is important if one is interested *e.g.* in the 2-D imaging of a single spectral line.

Spherically bent crystals

The ideal shape of the mirror (crystal) for aberration-free imaging of a point source is an ellipsoid. In all other cases, the aberrations depend on the angular aperture of the mirror [74]. Aberration free imaging of an extended source, however, can only be achieved by means of two mirrors [75]. However, these schemes are very difficult to realize.

A first approximation towards aberration free imaging is to ensure that the focal lengths, *i.e.* the position of the images, in both, the sagittal and meridional plane, coincide: From Eq. (1.17) it is obvious that one has to control both bending radii independently and that only for an incident angle of 90° $R_s = R_m$, *i.e.* a spherical crystal, can be used.

However, spherical crystals are frequently used [76–79] with astonishingly good results. Therefore, the use of spherical crystals at incident angles $< 90°$ will be briefly discussed here:

Assuming that the imaging geometry is well aligned to the image in the meridional plane, *i.e.* at the distance b_m, the image in the sagittal plane will lie behind the detector plane and the 'image' is broadened according to the opening angle of the beam cone, defined by the image distance in sagittal plane b_s and the aperture of the crystal in sagittal plane A_s. In the following discussion, a simple geometrical approximation is applied, where the size of the 'image' in the sagittal plane is estimated by the deviation of the detector from the image in the sagittal plane

$$\Delta b = b_s - b_m = \frac{a\ f_s}{a - f_s} - \frac{a\ f_m}{a - f_m}. \tag{1.20}$$

The estimated size of the 'image' of a point source on the detector ΔX is then given by the relation

$$\Delta X = A_s \cdot \frac{\Delta b}{b_s} = A_s \left(1 - \frac{f_s\ (a - f_s)}{f_m\ (a - f_m)} \right). \tag{1.21}$$

where f_s and f_m are given by Eq. (1.15) and Eq. (1.16), respectively.

In order to estimate the smallest structure which can be resolved, one has to divide Eq. (1.21) by the magnification $M = b/a$, where $b = b_m$, so that the resolution in the object plane

$$\Delta x = \frac{\Delta X}{M}. \tag{1.22}$$

As a further step, one might substitute a by M, *i.e.*

$$a = \frac{M+1}{M} f_m \tag{1.23}$$

so that finally, we obtain—after substituting the appropriate expressions for f_s and f_m—explicitly

$$\Delta x = A_s \, \frac{M+1}{M} \cdot \cos^2\theta, \tag{1.24}$$

which depends only on the magnification M, the aperture of the crystal in the sagittal plane A_s, and the angle of incidence θ and is independent of the radius of curvature of the crystal R.

From Eq. (1.24) one can see that the obtainable resolution in the sagittal plane is the higher, the smaller the aperture A_s, the larger the magnification M and the closer the angle of incidence is to $\pi/2$.

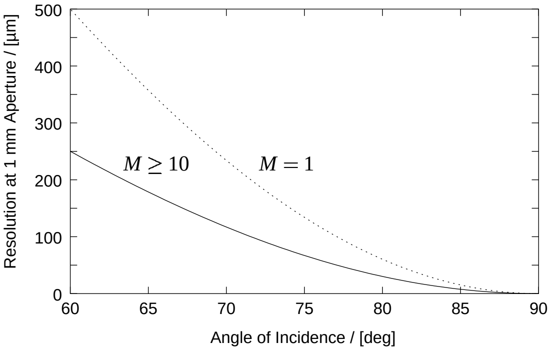

Figure 1.5. The resolution in the sagittal plane at spherical crystals, estimated by Eq. (1.24) for 1 mm crystal aperture.

Figure 1.5 illustrates Eq. (1.24) for the case of an aperture size in the sagittal plane $A_s = 1$ mm and for two magnifications, namely $M = 1$ and $M \gtrsim 10$. For higher magnifications, the term $(M+1)/M$ does not change anymore considerably so that the solid curve marks the limit. For a Bragg angle of 60°, the obtainable resolution is limited to 250 μm for the high magnification case, and in order to reach 10 μm, the Bragg angle has to be larger than 84°.

However, the Bragg angle cannot be chosen arbitrarily, but depends on the discrete wavelength of the X-ray source[1] and the discrete interplanar lattice spacing of the crystal. Additionally, for plasma diagnostics, the wavelength is defined by other experimental conditions so that only the lattice spacing remains for the selection of the Bragg angle. However, the suitable lattice spacing has to be found in an elastically bendable crystal so that the angle of incidence can be hardly changed.

The other possibility to increase the resolution is to reduce the aperture of the crystal. Note that only the effective aperture size is important, not the actual size of the crystal. Aglitskiy *et al.* [76, 77, 80] could demonstrate a spatial resolution of 1.7 μm using a crystal size of 5×10 mm^2 at a Bragg angle of 81.8° and a magnification $M =$

---

[1] Not considering here the continuous Bremsstrahlung and Synchrotron radiation, where the wavelength can be freely chosen

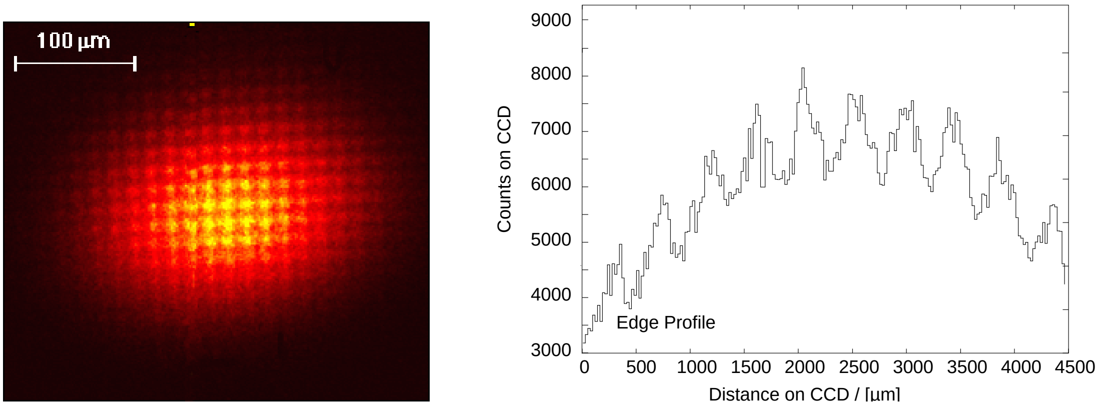

Figure 1.6. 2-D Image test using a toroidally bent Ge(311) crystal and a 1000 lpi gold mesh.

20. However, since the backlighting source of 400 μm diameter was placed 50 mm behind the test grid, while the distance from the grid to the crystal was 105 mm. Thus, the effective aperture was only about 840 μm (*cf.* Section 1.3.1).

Even if this high resolution of 1.7 μm is very impressive as demonstration, its practical use might be doubtful, since the aperture is artificially reduced. For photon critical experiments, where one is interested in a large aperture, this artificially small aperture might have an insufficient luminosity and might therefore be of of limited use.

1.2.3 Requirements of the camera

For the high-resolution observation of the plasma instabilities, a new X-ray crystal camera was designed to fit the requirements of a high resolution microscopy.

In an earlier experiment in the frame of this work [31, 46, 47], a spatial resolution of better than 6 μm was already obtained as shown in Figure 1.6, using a Ge (311) crystal with $R_m = 200$ mm and $R_s = 194.7$ mm bending radii. The size of the crystal was 7×7 mm and a CCD camera with a pixel size of 22.5 μm was used as a detector at a distance of 1849 mm. A test mesh with 1000 lines per inch, *i.e.* a period of 25 μm, and 9 μm bar width was used as a test object at an object distance of 104.2 mm. The resulting magnification $M = 17.7$. As a backlighter source, the M-shell lines from a gold plasma were used while the crystal was set to an angle of incidence of 80.63°. Contrary to the above mentioned demonstration experiment by Aglitskiy *et al.* [76,77], the full aperture of the crystal was used.

The bars are resolved, which demonstrates that the spatial resolution is better than

9 μm. To get more precise information about the resolution, the grid image was analyzed by the following procedure [31]: By Fourier analysis of the image the noise was removed by filtering high frequencies. Then, the Fourier data of the real image was divided by the Fourier data of the real grid to obtain the point spread function by back transformation. By using Rayleigh criteria [70], the obtained spatial resolution was determined to 6.2 μm in the object plane or 110 μm in the detector plane. These 110 μm correspond to five pixels of 22.5μm, which is at the physical limit of resolution of the CCD array.

Therefore, one approach to obtain the required spatial resolution of less than 3 μm in this experiment was to increase the magnification in order to overcome the limiting resolution by the CCD array.

In order to protect the crystal from damage by plasma debris, the object distance has to be larger than 100 mm [74]. However, the larger the object distance, the larger is the image distance, too, and the smaller the covered solid angle from which the photons are focused, *i.e.* the smaller the luminosity. As a compromise, an object distance of 140 mm was chosen, resulting in an image distance of 4200 mm for $M = 30$, which can be still realized in the target chamber hall of GEKKO XII. These distances are linked by a focal length of 135.48 mm.

Another constraint concerns the wavelength of the backlighter source, which was selected according to the boundary conditions of a high transmittance and high resolution as the H-like ^{12}Mg Lyα emission line with a center transition wavelength of the H-like doublet of $\lambda = 8.42235$ Å (*cf.* Section 1.1.3).

Based on these conditions, the crystal layout was designed: A suitable d-spacing was found in the Quartz $(10\bar{1}0)$ crystal lattice plane with $d = 4.254783$ Å, resulting in a Bragg angle of $\theta_B = 81.80°$.

For the given focal length $f = 135.48$ mm and Bragg angle $\theta_B = 81.80°$, the required bending radii of the crystal can be calculated by Eqs. (1.15) and (1.16) as $R_s = 268.2$ mm and $R_m = 273.8$ mm, respectively.

1.2.4 Simulation

In order to check the performance of the imager described above, ray-tracing calculations using the T-RAY code [81] were carried out.

The original version of the T-RAY code was developed particularly for the Apple Macintosh platform, taking advantage of the graphical user interface (GUI) of the

MacOS. However, for heavy number crunching, the GUI is a nuisance since it is designed for the *interaction* between user and machine. But for number crunching, one wants the machine to do the job silently without any further interaction. Additionally, the GUI is platform dependent. Thus the original program will not run under other machines except for the Macintosh.

Therefore, all GUI directives in the T-RAY code were removed so that a pure ANSI C/C++ code remained, which could be now compiled and executed on any machine. The calculation parameters are provided in a simple ASCII file and the output is provided again in ASCII and simple binary files. For the convenience of the user, a GUI was programmed, too, in the TCL/Tk scripting language, which is available on (almost) any platform. The GUI writes the T-RAY input file, starts the T-RAY code, and displays the output files in a convenient form to the user. In this format, T-RAY is now platform independent.

Thanks to the removal of all interactive parts from the T-RAY code, T-RAY can now be run as a subprocess of any other program. While the interactive character of the original T-RAY version forces the user to change a parameter manually, starting T-RAY, waiting a few minutes for the result, analyze the result with another program, change a parameter, starting T-RAY again, and so on, it is now possible, for a shell program to do the job automatically: The user has just to write a small program/script in a scripting language like TCL, Perl, IDL, Matlab, etc, which writes or modifies the T-RAY input file, starts the T-RAY code, analyzes the calculation result, writes the result of the analyzation in a file, and starts T-RAY again. The advantage is clear: While at the original version, the user tends to make calculations only for a specific point (*e.g.* the best focal position) it is now easy to calculate long scans, which can give new insights in the complicated optical relations of the toroidal crystal (*cf.* Ref. [74]).

Figure 1.7 shows the point spread function (PSF), calculated by the T-RAY code, for three different representative points. For the calculations, the actual achieved bending radii of the crystal of $R_m = 275.6$ mm and $R_s = 269.8$ mm were used instead of the design values mentioned in the last section. Thus, the focal length is 136.34 mm and the object and image distance are 140.88 mm and 4226.5 mm, respectively, in order to get a magnification of 30. The reflection curve was calculated by the Takagi-Taupin equation [82–84] and as width of the emission line 16×10^{-3} Å was assumed. For the calculation, a pixel size of $5.0 \times 5.0\ \mu\text{m}^2$ was assumed in order to get a more informative result than one would obtain with the actual pixel size of the CCD array. All

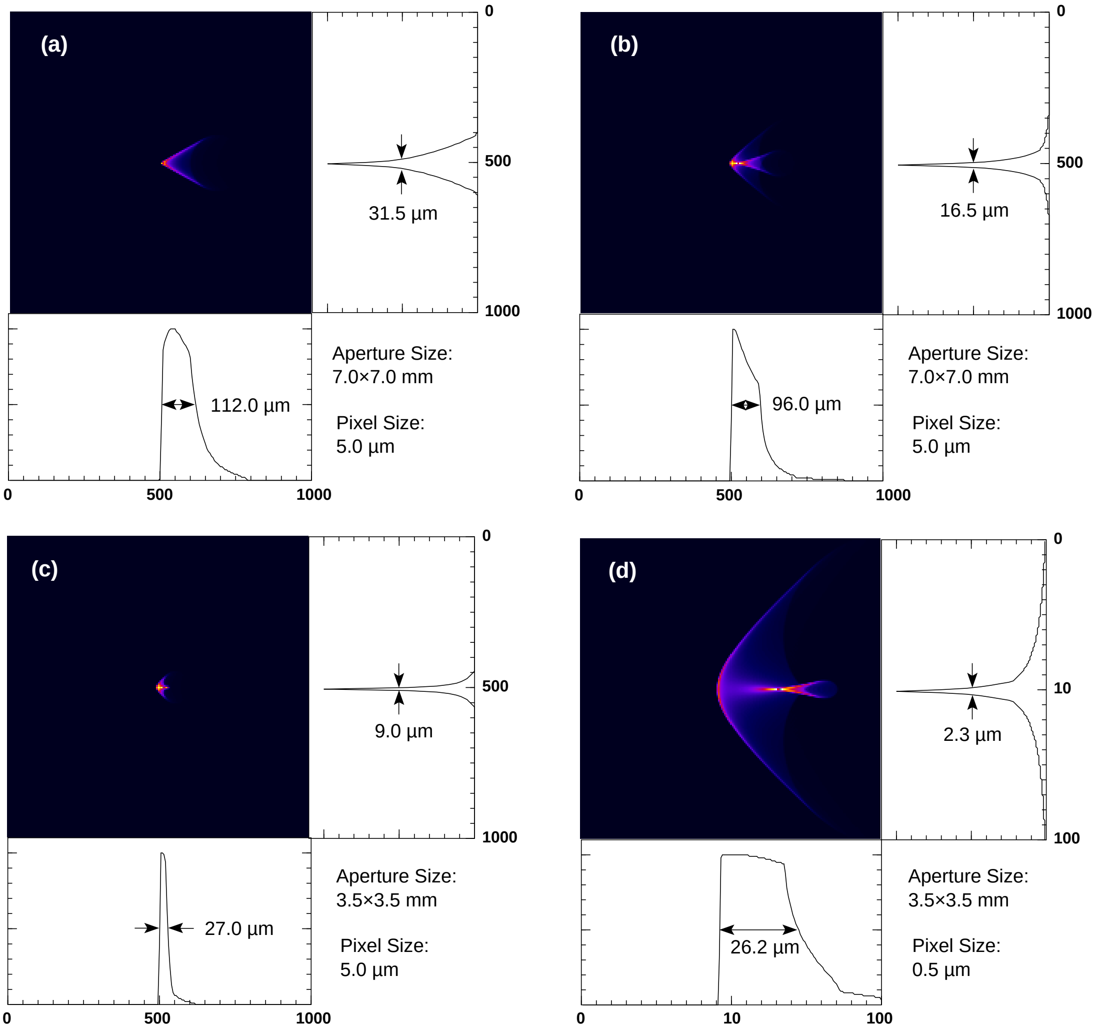

Figure 1.7. The point spread function for different aperture sizes and focalization at 30× magnification (see text).

distances in Fig. 1.7 are given in micrometers and are related to the detector plane. In order to obtain the achievable resolution, these distances have to be divided by the magnification, *i.e.* 30.

Figure 1.7a shows the point spread function for the toroidally bent crystal with 7.0×7.0 mm^2 aperture size of the crystal and the object and image distance aligned according to Eq. (1.14), *i.e.* 140.88 mm and 4226.5 mm, respectively. The image of the point is broadened due to imaging errors like focus, astigmatism, coma, field curvature, and spherical aberration[2], which cause the image of the point to be spread over a 'triangle', *i.e.* the spreading occurs in the meridional plane in one direction, only. The FWHM of the image is 112.0 μm and 31.5 μm in the meridional and sagittal plane and by dividing this size by the magnification, one obtains 3.7 μm and 1.0 μm resolution, respectively.

By shifting the detector slightly ($\sim 2\,\%$) towards a larger image distance (4320 mm), shown in Fig. 1.7b, the detector will be in a plane where the first order image is de-focalized, *i.e.* broadened, but the higher order images, *i.e.* the 'imaging errors', are narrowed so that the overall point spread function can reach a minimum. The size of the image in the meridional and sagittal plane becomes 96.0 μm and 16.5 μm, corresponding to a resolution of 3.2 μm and 0.6 μm, respectively.

Figure 1.7c shows the same configuration as in Fig. 1.7b but for a smaller aperture size of the crystal, namely 3.5×3.5 mm^2 instead of 7.0×7.0 mm^2. Since only the region close to the center is used, the imaging errors are reduced, too. From Fig. 1.7c one can see that an image size of the source on the detector of 27.0 μm and 9.0 μm in meridional and sagittal plane, respectively, can be achieved. Dividing these numbers by the magnification of 30×, the achievable resolution amounts to 0.9 μm and 0.3 μm in sagittal and meridional planes, respectively.

Finally, Fig. 1.7d shows the calculation for the same parameters as in Fig. 1.7c, but the pixel size was assumed to be 0.5 μm in order to get a magnified image of the point spread function on the one hand and on the other hand, to get a higher resolved number for the FWHM of the profile of the point spread function since the 9.0 μm in Fig. 1.7c correspond to less than 2 pixels. These higher resolved calculations confirm the FWHM value in meridional plane but promise a width of the point spread function in sagittal plane of 2.3 μm, which correspond to an achievable resolution of 0.08 μm

---

[2] An analytical description of the complicate optical relation of toroidal surfaces is given by Dirksmöller in Ref. [74] and should not be repeated here.

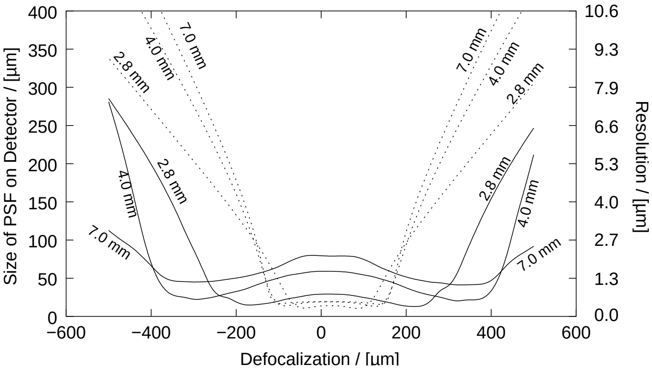

Figure 1.8. The FWHM of the point spread function in sagittal (·····) and meridional (—) plane for 2.8 mm, 4.0 mm and 7.0 mm aperture size as well as the resulting resolution as a function of the de-focalization.

in sagittal plane!

Using an analytical approach to consider diffraction inside the crystal by Chukhovskii *et al.* [85], the obtainable resolution in meridional and sagittal plane can be estimated as

$$\Delta x_m = \frac{\lambda R_m}{A_m}, \qquad \Delta x_s = \frac{\lambda R_m \sin\theta_B}{A_s} \tag{1.25}$$

respectively. For the example considered here ($R_m = 275.6$ mm, $A_m = A_s = 3.5$ mm, $\lambda = 8.42$ Å, $\theta_B = 81.8°$) $\Delta x_m = 0.07$ μm and $\Delta x_s = 0.06$ μm.

However, these simulations assume a perfect toroidal shape of the crystal and perfect crystalline structure. In reality, it is very difficult to achieve a precision of 10^{-3} in the bending radii. Moreover, the calculations are based on a surface reflection. In the nature, the X-rays penetrate typically a few to a few tens of micrometers into the crystal and exit at a location different from the entrance point [86]. This penetration depth depends on the wavelength of the incident X-rays and, contrary to the simulations, there are always higher order reflections present, *i.e.* X-rays with $\lambda/n\ n = 2,3,4,\ldots$ with different penetration depths in the crystal, which will give superimposed images. These effects will limit the achievable resolution [87] too, and are not taken into account here. Therefore the above presented numbers for the sub-micrometer case are optimistic. In addition, one has to consider at these high resolutions the limitation by diffraction, which can be estimated for the case considered here (*cf.* Eq. (1.30)) as about 0.03 μm. Nevertheless, it would be worthwhile testing whether a sub-micrometer resolution can be obtained by means of toroidally bent crystals and a large magnification (*cf.* Sec. 1.3.2).

Another crucial point in the imager, is a large focal depth, since the target will be accelerated by 5×10^{15} cm/s^2 in 4 ns to 2×10^7 cm/s and the Rayleigh-Taylor instabilities should be observed within the first 2 ns, corresponding to a flight distance

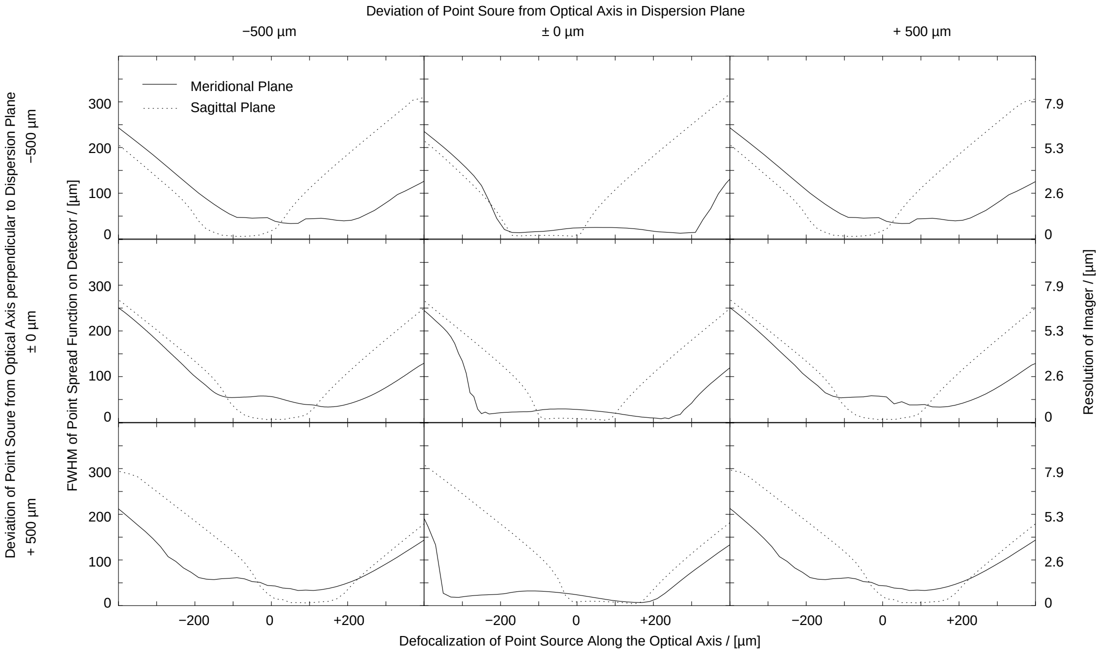

Figure 1.9. The calculated width of the PSF for 2.8 mm crystal aperture and and deviations of the point source from the optical axis.

of ~ 400 μm.

In order to check the focal characteristics of the imaging system, a script was written which starts T-RAY for the calculation of the PSF for a particular imaging geometry. The FWHM of PSF in both the sagittal and meridional plane were computed by another program, called PROFILER, which was written for the evaluation of the T-Ray output. Then, the object distance was varied in each step by 20 μm and T-RAY was started again until the complete scan was performed.

The calculations assume a toroidally bent crystal with $R_m = 275.6$ mm and $R_s = 269.8$ mm, as achieved in the manufacturing process for the here presented experiment. Nominal object and image distance of 139.9 mm and 5284 mm, respectively, were assumed for the calculations, since these were the realized values of the imaging test (*cf.* below). The resulting magnification $M = 37.75$.

In a first step, the PSF as a function of the de-focalization was calculated for three different aperture sizes, namely 7.0 mm, 4.0 mm and 2.8 mm and the FWHM of the PSF for both, the meridional and sagittal plane is plotted in Fig. 1.8. The solid line marks the FWHM in the meridional plane and the dotted line the FWHM in the sagittal plane. While the left hand side ordinate gives the size of the image on the detector, the right hand side ordinate gives the size of the image divided by the magnification, *i.e.* the resolution of the instrument. Far away from the theoretical optimal focal position, the FWHM in sagittal plane follows a simple geometrical approximation (*cf.* Eq. (1.34) and Fig. 1.15) which would become zero for the best focal position. However, due to the higher order imaging errors, the point spread function becomes very fast narrower and has a flat bottom around the best focal position. This flat bottom can be explained by the imaging errors, which cause the reflected light from the outer crystal region to cross the optical axis before or behind the focal point. The length and the width of this 'line focus' along the optical axis is the longer, or wider, the larger the crystal aperture is.

In the meridional plane, for 7 mm aperture, the focal length is about 800 μm, with a size of the point spread function on the detector of about 75 μm, corresponding to an obtainable resolution of about 2 μm, while for 2.8 mm aperture size, the FWHM of the PSF amounts about 30 μm in a range of 400 μm, corresponding to 0.8 μm resolution. In the sagittal plane, the focal length for all three aperture sizes amounts about to 200 μm with a FWHM of about 15 μm, or an obtainable resolution of 0.4 μm.

Since a large field of view is required, the focal scan was calculated for the point source on the optical axis as well as for a deviation of the source point of ± 500 μm in both the meridional and the sagittal plane. The FWHM of the scans are shown in Fig. 1.9 for each deviation in each plane. The PSF in Fig. 1.9 is calculated for 2.8 μm aperture size. For larger aperture sizes, the result is similar, taking into account the changes in Fig. 1.8.

For a deviation of the source point perpendicular to the dispersion plane, the best focus position in sagittal plane is shifted by ± 100 μm for a deviation of the source of ± 500 μm, while the focal depth remains unaffected. A deviation of the source point in dispersion plane, however, has almost no influence on the behavior of the FWHM in sagittal plane of the PSF.

In the meridional plane, a deviation of the source point perpendicular to the dispersion plane of ± 500 μm causes a shift of the focal depth by about ± 50 μm, only, while a deviation of ± 500 μm in dispersion plane causes the focal depth to be distorted. The interesting point is that the distortion is identical for the deviation in both directions.

In summary, a high resolution from the crystal optic can be expected, with a very long focal depth even at such high magnifications as 30× and a very large aperture of 7 mm.

1.2.5 Design of the X-ray imager

To ensure a proper alignment of the crystal concerning focus and position of the image on the detector, a new camera, shown in Fig. 1.10 was designed which enables all movements to be made by remote control so that an on-line alignment is possible.

The main component of the camera is a toroidally bent Quartz $(10\bar{1}0)$ crystal of 7×7 mm^2. The bending radii are 275.6 mm in the meridional (dispersion) plane and 269.8 mm in the sagittal plane. The resulting 'stigmatic angle' $\theta_0 = 81.66°$. The interplanar lattice spacing is $2d = 8.5096$ Å which gives a Bragg angle $\theta_B = 81.7898°$ for the central wavelength of the Mg Ly$_\alpha$ doublet of $\lambda = 8.42235$ Å, where the difference in the wavelength amounts 5.9 mÅ. For a typical line width of $\Delta\lambda/\lambda \sim 10^{-3}$, the width of the doublet can be estimated as $\sim$ 14 mÅ. The spectral window of the crystal at a magnification of $M = 30$ amounts to $\sim$ 29 mÅ, which does not change further for higher magnifications since the term $|(M-1)/(M+1)|$ in Eq. (1.19) for $M = 30$ is already in 'saturation'.

The crystal is mounted on a mini-goniometer where the Bragg angle can be set using a step motor. Once this goniometer is calibrated (*cf.* Sec. 1.2.6), the Bragg angle can be easily set just by moving it to the corresponding counter value. Also, an *in-situ* alignment is possible by measuring the reflection curve.

A debris shielding in front of the crystal is necessary to protect the crystal from debris which destroy the surface of the crystal and make it 'blind'. Thus Pawley *et al.* [80] had to replace their crystal after several shots, which is a very expensive solution of the problem. The 'standard' solution, namely a thick fix beryllium window in front of the crystal, is not possible here due to the high absorption coefficient of Be at this wavelength. A 50 μm thick Be-window (linear absorption coefficient $\mu(8.4192\text{ Å}) = 357.0/\text{cm}$) would absorb 97 % of the signal since the beam has to pass the window twice. Later in the imaging test, we tested a 10 μm thin Be-window, too, which absorbs only 51 % of the intensity. But this window was perforated after one shot.

We therefore chose 1.5 μm thin polyester foil ('Mylar') evaporated with 200 nm aluminum, which transmits 63 % of the X-rays (total linear absorption coefficient $\mu = 1553/\text{cm}$). The Al coating is necessary since the intense visible light from the plasma is suspected to destroy the glue, making the crystal unusable [88]. Since we expected the foil to be not stable enough for permanent operation, a 'shielding wheel' was mounted in front of the crystal. This shielding wheel consists of twelve windows, covered by the shielding foil. All windows, apart from the one in front of the crystal,

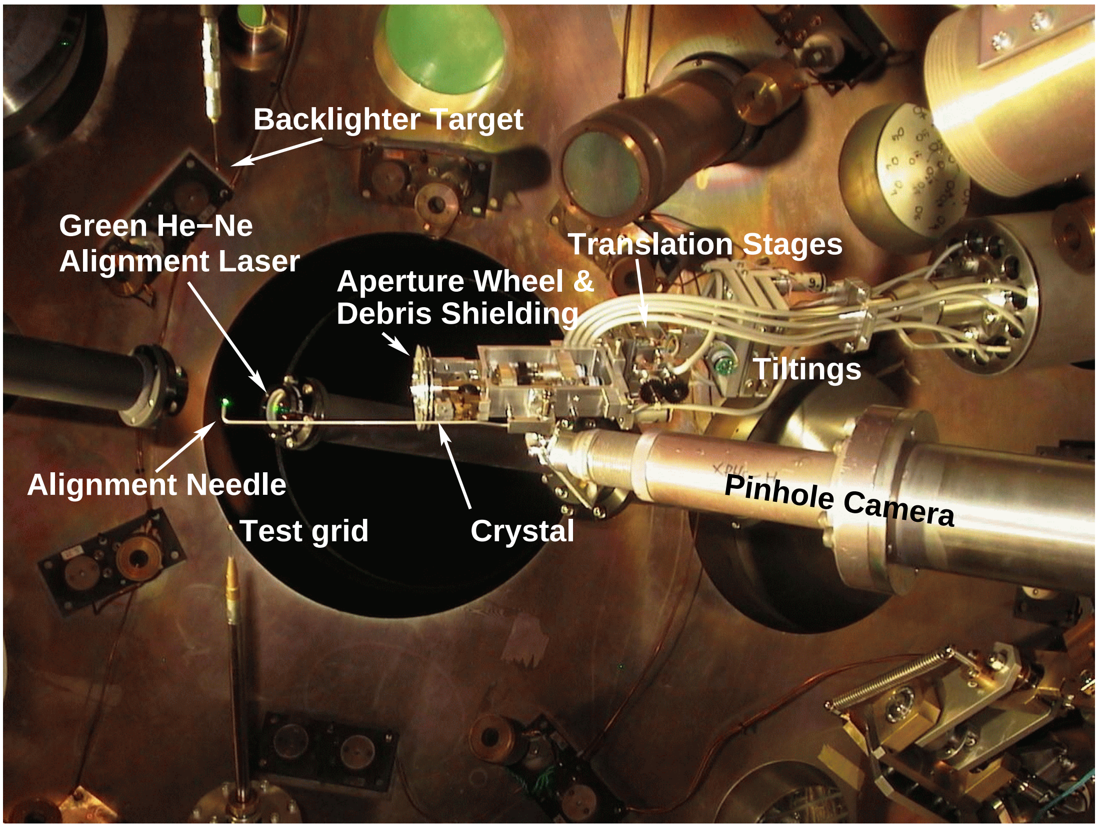

Figure 1.10. The HIPER Imager inside the target chamber.

are again hidden behind a thick fix Al-plate. When the debris destroys one window, the wheel can be rotated so that another shielding foil is in front of the window.

For alignment purpose a motorized removable pointer, or ‘needle’, was integrated in the camera: For the pre-alignment outside the target chamber, the tip of the needle marks the position of the plasma to be imaged. Thus all alignments could be done relative to the tip of the needle. When the camera is in operation, the needle could be removed. When the camera had to be taken off the target chamber, *e.g.* for exchanging the shielding wheel, the needle can be moved again to the plasma position, the work can be done outside the target chamber and later one has to ensure that the tip of the needle is back at the same position.

During the construction phase, it was not clear how many photons could be expected, since this was a completely new experiment at the ILE. Therefore, an aperture wheel was mounted in front of the crystal with eleven different aperture sizes, namely 8.0 mm, 5.6 mm, 4.0 mm, 2.8 mm, 2.0 mm, 1.4 mm, 1.0 mm, 0.7 mm, 0.5 mm, 0.35 mm, and 0.25 mm in diameter. These values were chosen so that the diameter was always reduced by a factor $\sqrt{2}$, resulting in a reduction of the area, and thus the transmitted intensity, by a factor two. Additionally, there was a position which hides the crystal completely from the X-rays. This position could be used for test purposes or to protect the crystal efficiently when it is not in use.

In order to align the image on the detector, the crystal could be shifted motorized in three- and tilted in two directions. The translation stage was set up so that one direction is parallel to the incident beam. With this translation direction, the focus could be set properly.

The detector was mounted at an extension tube outside the target chamber. Close to the target, a collimator tube was installed inside the extension tube, so that only X-rays which are diffracted at the crystal could reach the detector. In order to suppress the scattered laser light, a filter holder was forseen close to the detector.

To make the alignment using X-rays possible, there was a new so-called ‘diagnostics laser’ installed at the ILE with 6 Hz repetition rate. This laser could be used to create a small plasma for the generation of X-rays.

1.2.6 Calibration of the goniometer

One important advantage of this crystal stage is the step motor driven variation of the Bragg angle. It is therefore no longer necessary first to pre-align the Bragg angle on a separate goniometer, to mark the direction of incidence by a needle, aligning then this needle to the marker of the center of a skeleton, which models the target chamber for pre-alignment, then removing the marker needle from the crystal holder and aligning the needle of the crystal manipulator to that position [89].

With this new crystal stage, the integrated marker needle has just to be aligned to the target chamber center and all the alignment can be done without removing the crystal or copying the plasma position from one instrument to another. Thanks to the step motor driven mini-goniometer, the angle can be set by moving the goniometer head to the well-defined position. To find the relation between the motor steps and the angle, the mini-goniometer was calibrated as follows:

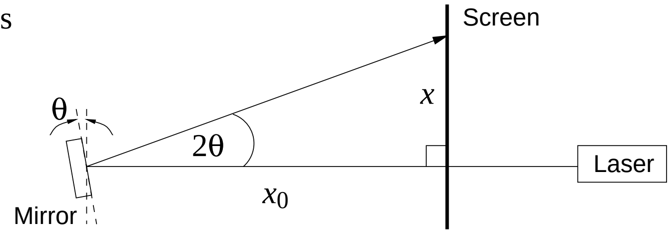

Figure 1.11. Setup for the calibration of the goniometer.

For the calibration, the set-up as shown in Fig. 1.11 was used. Instead of the crystal, a front-side mirror was mounted on the mini-goniometer. A laser was pointed auto-collimated to the mirror and the reflected beam was monitored on a screen perpendicular to the auto-collimated beam at a distance of $x_0 = 1000$ mm. As a ‘screen’, a 10 mm thick and 600 mm long metal plate with a hole in it at one corner was used. Now the mirror was turned on the goniometer head by the angle θ causing the reflected beam to be deviated from the auto-collimated position by

$$x = x_0 \tan 2\theta. \tag{1.26}$$

Thus the angle θ can be determined by measuring the deviation x of the reflected beam on the screen as

$$\theta = \frac{1}{2}\arctan\left(\frac{x}{x_0}\right). \tag{1.27}$$

The relation steps–deviation was measured three times. The measured values are plotted in Fig. 1.12 together with the linear fit and the deviation of the measured values from it.

The linear fit was determined by a least-square-fit as[3]

$$\boxed{\boxed{\theta[\mathrm{deg}] = \left(1.3206\times10^{-4} \pm 6.7\times10^{-8}\right)\times \mathrm{Steps}}} \tag{1.28}$$

---

[3] Since the off-set angle is arbitrary and thus not interesting for the calibration, it is omitted here.

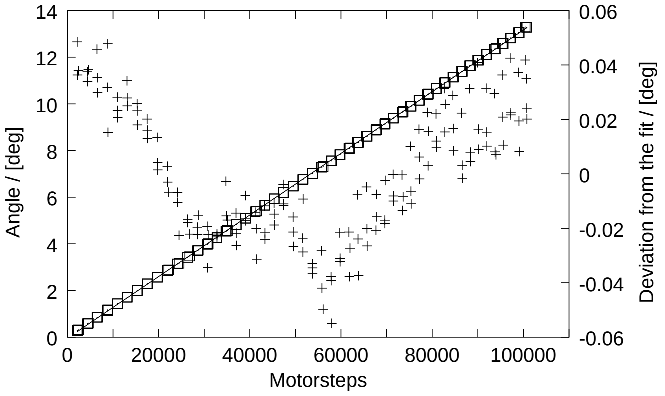

Figure 1.12. Calibration curve of the mini-goniometer: The boxes (□) present the measured values together with the linear fit (straight line; both left ordinate) and the pluses (+) are the deviation of the measured values from the linear fit (right ordinate). Note the large different scale of both ordinates, the error bars of measured values are smaller than the line width.

or, inverted,

$$\boxed{\boxed{\text{Steps} = (7572.3 \pm 3.8) \times \theta[\text{deg}].}} \tag{1.29}$$

Besides the statistical scattering, a clear structure is visible in the deviation from the linear relation (“+” in Fig. 1.12), which seems to appear from the mechanical precision of mini-goniometer, which is reasonable for the manufactured precision of the mini-goniometer [90]: This deviation is reproducible and all other influences (like a large deviation from the 90 degrees angle between screen and incident laser beam) would give a much larger structure. Also, if it were a statistical effect, it would not be reproducible.

However, even if this structure is reproducible, it was not taken into account in the calibration relation here, since this structure is a function of the position of the cradle of the mini-goniometer and not of the angle between the incident and reflected beam. But only the angle between the incident and reflected beam was measured, which is interesting for calibration. A marker at the mini-goniometer would give a possibility to calibrate the mini-goniometer to the position of the cradle, but then, one would have to measure always relative to the this marker. *I.e.* when aligning the Bragg angle one would first have to measure the angle between normal incidence and this marker and then to turn—according to the complicated calibration function—the cradle to the Bragg angle. Since it is not clear, how precisely the zero position and the angle of normal incidence can be determined, the rewards of this effort are doubtful.

Thus, even if the slope error of the calibration function is small due to statistical reasons, the error of a single point is $\pm 0.06^\circ$, which correspond to an error in the counter steps of ± 460 steps. Another error source is the systematic uncertainty, due to the misalignment of the screen from the mirror of $\Delta x_0 = \pm 1$ mm which results in an uncertainty of $\Delta\theta = \pm 0.02^\circ$ at $\theta = 10^\circ$. The play in the gear was measured to be about 7000 steps, so that a backlash of > 7000 steps has to be considered.

In summary, the achieved range of confidence of $\Delta\theta = \pm 0.06^\circ$ or ± 460 steps covers all influences of errors and is sufficiently small for the experiment, since the emission line doublet under observation is reflected in a Bragg angle range of $\Delta\theta_B = \pm 0.2^\circ$.

1.3 Imaging test

1.3.1 Imaging test at GEKKO XII

One major aim of the experiment is the demonstration of the cut-off perturbation wavelength of the Rayleigh–Taylor instability, *i.e.* the perturbation wavelength at which no RTI will occur which is expected to be in the order of about $3 - 10$ μm. Therefore the demonstration of the resolving properties of the diagnostics is crucial, since one has to be sure that the non-observation of RTI below a certain spatial frequency is due to the non-existence of the RTI and not due to the limited resolution of the diagnostics.

Therefore, an imaging test was performed. The crystal and the detector should be set-up similar as in the real experiment, but with a grid as a dummy sample. The setup is shown schematically in Fig. 1.13 and the geometry is summarized in Tab. 1.1.

Five attempts have been made in order to carry out the demonstration of the performance of the imager. However, due to technical problems with the laser system, only one experiment could be carried out under very restrictive conditions as a so-called ‘background experiment’ at GEKKO XII. *I.e.* another experiment, called ‘foreground experiment’, has the first priority of laser conditioning, but in that experiment not all laser beams are used. The unused laser beams are redirected to the other target chamber and can there be used parasitically by another experiment, the background experiment. However, the background experiment has no influence on the laser shot; neither over the pulse energy nor the delivering time of the shot nor over the alignment of the focal position because re-positioning of the focal point needs one day, which was not accepted. The latter point was a crucial point for the imaging test, since the sample is normally aligned to the center of the target chamber and the backlighting source is

Crystal		Quartz $(10\bar{1}0)$
Meridional bending radius	R_m	275.6 mm
Sagittal bending radius	R_s	269.8 mm
Stigmatic angle	θ_0	81.66°
Bragg angle	θ_B	81.79°
Focal length	f	136.34 mm
Object distance	a	139.954 mm
Image distance	b	5284 mm
Distance Object–Image	c	5150 mm
Magnification	M	37.75
Aperture of the crystal	A	4 mm diameter
X-ray wavelength	λ	8.42235 Å
Spectral window	$\Delta\lambda$	17 mÅ
Source size	S	$\sim$ 10 mm
Source distance	d_S	$\sim$ 1700 mm
Effective aperture	A_{eff}	$\sim 0.8 \times 0.8$ mm^2
Pixel size of the CCD		22.5 μm
Step width of focus		0.04 μm/step

Table 1.1. Setup of the imaging test. Distances are given for the optimal alignment.

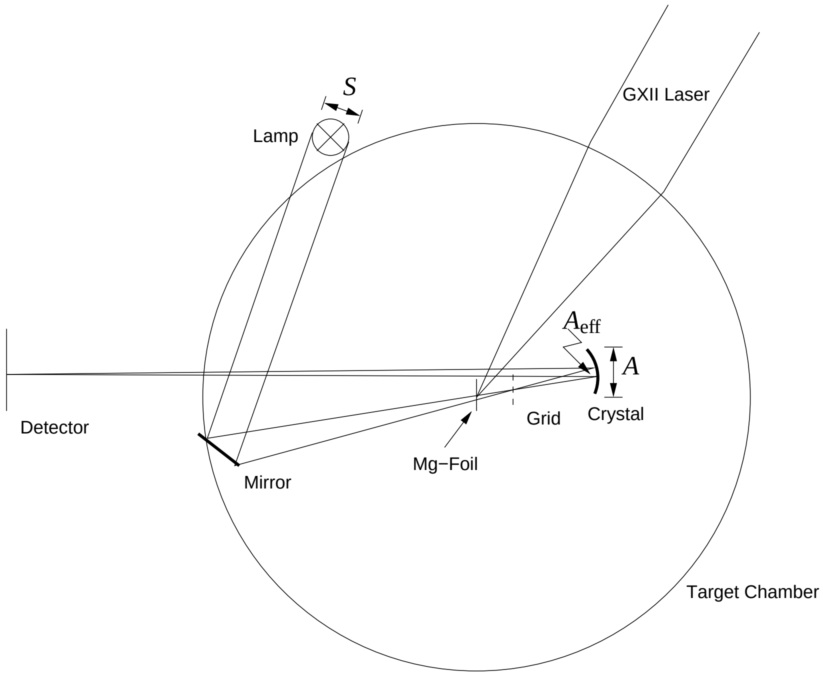

Figure 1.13. The schematic layout of the imaging test.

set with a certain offset behind the center. Thus, the laser beam for the backlighting source has to be aligned to a position away from the center. But this is not possible in the background experiment. Here, the laser beams can only be aligned to the center of the target chamber.

To work around this limitation, the alignment procedure was as follows: First the test grid was aligned to the center of the target chamber, using the target monitors and the well controllable step-motor driven target positioner. Then, the aligned target was shifted by 2 mm off the center position towards the crystal, which itself had to be shifted back by 2 mm, too, taking advantage of the motorized target positioner and focus, so that the object distance remained constant.

In order to find the best focal position, a focal scan using visible light was carried out. As an object, the edge of a grid was set at the center of the target chamber and back-lighted by a tungsten condenser lamp. In order to place the light source on the axis which links the object and the crystal, a mirror was mounted inside at the target chamber wall, which reflected the light from the condenser lamp towards the crystal, which itself was placed outside the target chamber behind a window port. Thus, the distance of the source from the object was about twice the radius of the target chamber.

Table 1.2. The parameters of the fabricated glass forms.

Glass form		"3"	"4"
Radius in meridional plane	R_m	275.6 ± 0.1 mm	276.0 ± 0.3 mm
Radius in sagittal plane	R_s	269.8 ± 0.1 mm	270.0 ± 0.2 mm
Stigmatic angle	θ_0	81.66°	81.52°
Focal length	f	136.34 mm	136.49 mm
Associated Crystal Nr.		126	127

As figure of merit, the full width at half maximum (FWHM) of the derivative of the edge profile of the image of the grid was considered.

For the imaging test using Mg Lyα backlighting radiation, a Mg-foil was aligned at the center of the target chamber using a simple target positioner and the target monitors. Laser beams #07 and #08 were used.

However, it was not possible to obtain sufficiently good results for this set-up. The analysis of the experiment showed that there were three problems: The visible light alignment was not possible due to a too small source size, a crystal with a double image was used due to a mistake in the labeling and finally, due to a problem in the step motor controller, the crystal was shifted just by the half way as intended. After fixing these problems, there was no more beam time available to get good results. In the following, the analysis of the problems are described in detail:

Identification of the better crystal

For this imager, a new replica glass form was manufactured. To ensure a sufficiently high quality toroidal shape, four glass forms were prepared and tested as described in Ref. [91], of which the best one was to be selected.

Since the quality test of the replica form could not be carried out with a sufficiently small uncertainty due to the limited mechanical precision, the two best glass forms were used for the preparations of the crystals. The final imaging test of the crystals, using an X-ray generator, was to identify the best crystal.

In the protocol of the laboratory imaging test, the test image labeled with 'crystal 127' gave the better image, and accordingly, crystal 127 was selected for the HIPER experiment. As the obtained imaging quality was poor, both crystals were tested again outside the target chamber by a focal scan at visible light. The intention of this test

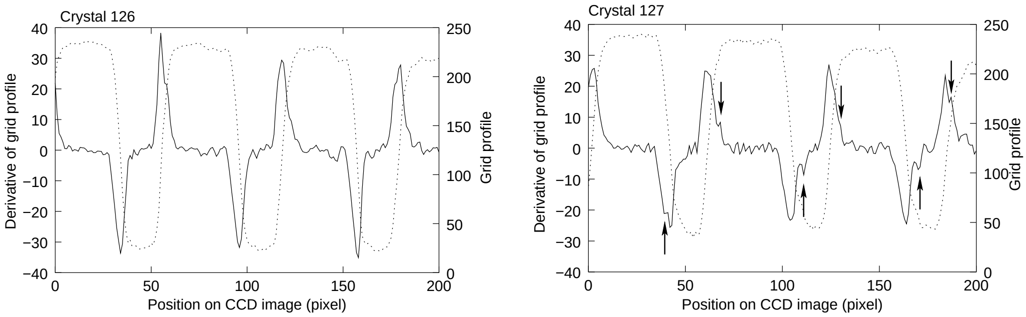

(a) (b)

Figure 1.14. The edge profile of the grid image (····) and the derivative (—).

was to identify the bending radii, labeling and, of course, find the crystal with the best imaging quality.

The setup was as follows: A test mesh was set up at a distance of about 158 mm and illuminated from the rear side by a tungsten condenser lamp. The image of the backlighted grid was observed at a distance of about one meter by a microscope with an attached digital camera with manual control over the focus (Nikon Coolpix 950). The object distance was varied along the optical axis by shifting the grid using a micrometer screw. The resulting images were recorded so that it was possible to compare the best object distance of both, crystal 126 and 127. The analysis of the focal scan showed that the best object distance for crystal 126 appeared to be about 0.3 mm shorter than that of crystal 127.

Since both glass forms have slightly different radii of curvature, the resulting focal length of both prepared crystals are slightly different, too (*cf.* Tab. 1.2). From the different radii of curvature alone, *i.e.* without assigning them to a particular crystal, one would expect from the crystal prepared with the glass form with $R_m = 275.6$ mm and $R_s = 269.8$ mm, resulting in a focal length of $f = 136.34$ mm, the best image at an object distance of 157.7 mm. For the crystal with bending radii $R_m = 276.0$ mm and $R_s = 270.0$ mm, *i.e.* $f = 136.5$ mm, the object distance amounts 158.1 mm, *i.e.* 0.4 mm longer than that of the other crystal.

By comparing the experimental result and the calculated distances, one would expect that crystal 126 was prepared with the glass form with $R_m = 275.6$ mm and $R_s = 269.8$ mm. This conclusion is in agreement with the labeling of the crystal itself so that this result is evident.

By comparing the images of both crystals by visible impression, the image of crystal 126 seems to be the better image. Also, it was much easier to identify the best focal position for that crystal. When we look at the derivative of each best focalized image (solid line in Fig. 1.14), the average FWHM of the edges of the grid structure amounts respectively 5.9 and 6.4 pixels for crystal 126 and 127, which is in accordance to the better visible impression. Also, the maxima of the derivative of crystal 126 are much higher, *i.e.* the edges are much steeper, than that of crystal 127. Moreover, while the derivative of the edges of the image from crystal 126 consists of single gauss peaks, the derivative of the image from crystal 127 shows double peaks (arrows in Fig. 1.14b), which might be due to a double image from the crystal as a result of the not homogene bending radii. Additionally, the glass form associated with crystal 127 was more difficult to measure since the imaging quality of the glass form as a lens seemed to give a double image, so that this result is confirmed. In summary, the imaging test of the crystals and glass forms are in agreement. Accordingly crystal 126 gives the better image than crystal 127.

However, this result is contrary to the labeling of the test protocol, where the good image is labeled as to be due to crystal 127 and the bad image as to be due to crystal 126. Thus, one might conclude that the labeling of the image test is wrong. In order to obtain further evidence of this conclusion, the sizes of the test images of the protocol were compared. In the laboratory imaging test, the position of the test object and the crystal position, *i.e.* the object distance, were conserved, while the image was focalized by changing the image distance. Due to the slightly different focal lengths the image sizes are expected to be slightly different. For the 1 mm large test object and an object distance of 182 mm, the size of the image should be 3.00 mm and 2.98 mm for 136.5 mm and 136.34 mm focal length, respectively. For the about 13 times enlarged image in the test protocol, this image difference should amount about 0.2 mm. Such a small difference can be observed in the test protocol, too. However, the larger image is labeled with “Crystal 126” and the smaller image is labeled with “Crystal 127”, *i.e.* the focal lengths of crystal 127 and 126 would be, respectively, 136.34 mm and 136.5 mm, thus contrary to the expectation and the measurement above. Therefore, the labeling is obviously exchanged.

Visible light focusing at the target chamber

After installation of the imaging system to the target chamber, the best focal position should be determined by means of visible light. This has the advantage that an intense

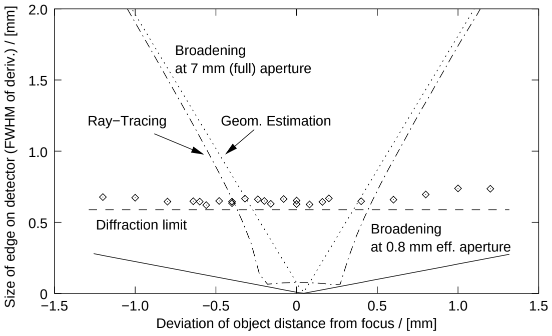

Figure 1.15. The measured FWHM of an edge as the function of the relative deviation from the focus together with the geometrical estimation of the broadening at full 7 mm (···) and effective 0.8 mm (——) aperture, respectively, and the limit due to diffraction (- - -). For comparison, the ray-tracing result for 7 mm aperture is plotted, too (—·—·—).

visible light source is very easy to obtain, and convenient to use. However, the quality of the alignment is limited by the diffraction of the light at the aperture of the crystal. Thus, the final precise alignment can be done by X-rays only, but the pre-alignment by visible light limits the range for the expensive and time consuming alignment by X-rays.

Figure 1.15 shows the measured FWHM of the derivative of the image of an edge, which was aligned to the center of the target chamber together with the geometrically estimated broadening of the image of a point (the edge) at full aperture size due to de-focalization (see below) and the resolution limit due to diffraction of the light at the aperture of the crystal.

Diffraction limit As mentioned above, the quality of the alignment is limited by the diffraction of the visible light at the aperture of the crystal. The resolution can be described by [92]

$$d = \frac{\lambda f}{A} \sim \frac{800 \text{ nm} \times 136.3 \text{ mm}}{7 \text{ mm}} = 16\ \mu\text{m} \tag{1.30}$$

where the 800 mm wavelength is arbitrary, since no considerations were carried out concerning the emission maximum of the lamp, which is in the far-infrared region, the transmittivity and reflectivity of the windows, lenses, mirror, and the sensitivity of the CCD. For the given magnification of 37.75 the edge will be broadened on the detector to

$$16\ \mu\text{m} \times 37.75 = 604\ \mu\text{m} \sim 27 \text{ pixel.}$$

The observed minimum width of edge is in very good agreement with the prediction. However, this coincidence is more or less arbitrary, since it depends on the unknown effective wavelength of the backlighter source.

Geometrical estimation of the broadening The de-focalization, *i.e.* the distance of the crystal from the optimal object distance can be estimated geometrically by considering the broadening of an edge.

Due to de-focalization the point image will be lying at a distance δb in front of or behind the detector position, *i.e.* the design image distance b_0 (*cf.* Fig. 1.16). Depending on the aperture size A of the lens (crystal), the point will be broadened to

$$B = \frac{A}{b_0} \cdot |\delta b|. \tag{1.31}$$

The distance δb is related to a variation of the object distance δa by the derivative of the lens equation

$$b = \frac{f \cdot a}{a - f} \tag{1.32}$$

(which is equivalent to $1/f = 1/a + 1/b$, where f is the focal length) as

$$\delta b = -\left(\frac{f}{a_0 - f}\right)^2 \cdot \delta a. \tag{1.33}$$

Combining Eqs. (1.31) and (1.33) we obtain

$$B = \frac{A}{b_0} \cdot \left|\left(\frac{f}{a_0 - f}\right)^2 \cdot \delta a\right|. \tag{1.34}$$

Note, that this equation assumes a rectangular aperture of the crystal, *i.e.* that the size of the crystal is constant for all angles of incidence. For circularly (elliptically) shaped crystals, one has to apply the average size of the aperture, which is reduced by $\pi/4$ compared to the size of a quadratic (rectangular) aperture. Also, when using X-rays, Eq. (1.34) can be applied in sagittal plane only since in meridional plane, the effective aperture is influenced by the width of the spectral line and the width of the reflection curve.

Equation (1.34) is plotted in Fig. 1.15 for the sagittal plane together with the full ray-tracing calculation for comparison. Except for the center region, which is dominated by the imaging errors, Eq. (1.34) is in very good agreement with the ray-tracing result.

For the full aperture size of 7 mm, one would expect from Eq. (1.34) a broadening of the image as shown by the dashed line in Fig. 1.15. The range of uncertainty in

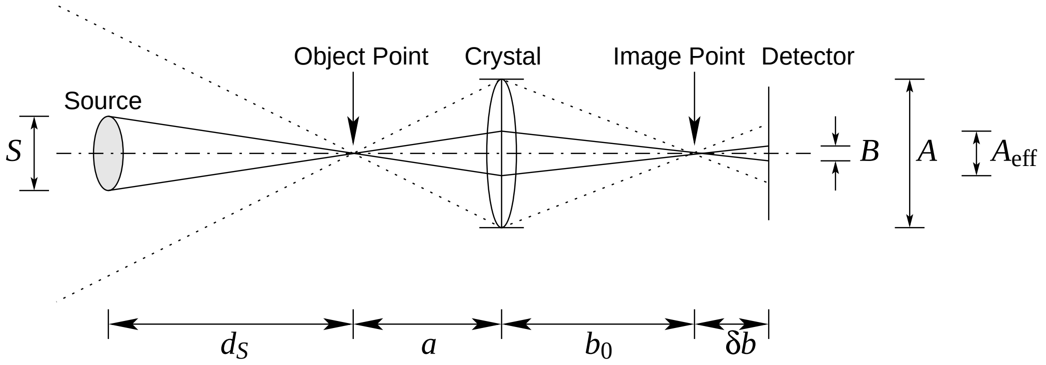

Figure 1.16. The effective aperture of the crystal. Despite of the large aperture of the crystal A, only a small fraction of it, A_{eff}, is used for imaging.

the best focal position would be therefore reduced to about ±0.25 mm, *i.e.* the range, where the geometrical estimation is hidden by the diffraction. In practice, this range is reduced again, since one would expect the best focus position in the center of the waist of the curve.

However, the observed FWHM remained almost constant over the full scan range of 2 mm, contrary to Eq. (1.34), which predicts a change in the broadening of the edge to more than 2 mm for a de-focalization of 1 mm.

At the time of the experiment, no explanation could be found for the flat curve. A later analysis showed that the reason was the small size of the source at a large distance from the object, as illustrated in Fig. 1.16: Despite the large aperture A of the crystal, only a small fraction A_{eff} of it was used for imaging, since there is no source point lying on the axis which connects the outer region of the crystal with the object point (*cf.* dotted lines in Fig. 1.16). In consequence, the opening angle of the rays is much smaller, and a shift of the image point off the detector plane will result in a smaller broadening than expected from Eq. (1.34) for the full aperture size.

In the present case, the condenser lamp was mounted outside the target chamber and the light was directed to the crystal by means of a mirror. Thus, the resulting distance of the source from the grid was about twice the radius of the target chamber, say 1700 mm. When the aperture of the condenser lamp would have been fully open, the source size would have been given by the size of the filament, say 10 mm. In this case, the effective aperture would have been about (*cf.* Fig. 1.16)

$$A_{\mathrm{eff}} = \frac{S}{d_S} \cdot a \sim \frac{10\ \mathrm{mm}}{1700\ \mathrm{mm}} \cdot 140\ \mathrm{mm} \sim 0.8\ \mathrm{mm}. \tag{1.35}$$

instead of the crystal size of 7 mm, as assumed. The resulting broadening of the image due to the delocalization at 0.8 mm aperture size is shown in Fig. 1.15, too. The broadening grows very slowly, as observed in the experimental data.

However, at the time of the experiment, the aperture of the condenser lamp was closed to see a sharp shadow of the grid on the crystal in order to ensure that the source was lying on the optical axis. Another reason for the closed aperture was to reduce the intensity of the source to avoid saturation of the CCD.

In conclusion, one has to consider the aspect of the source size in future alignment procedures. Also, this result is important for the design of backlighting experiments. Since one is in general interested in a uniform backlighting source, one likes to put the source behind the sample as far as possible in order to get a blurred image of the source on the detector. However, when one likes to use the full aperture of the crystal, too, in order to get a high efficiency of the optic, one has to make sure that the backlighting source is large enough so that the full aperture of the crystal is really used.

Imaging test using X-rays

From the visible light focus scan shown in Fig. 1.15, the best focal position was assumed at the position marked at the ordinate with zero, which refers to the target chamber center.

However, for the X-ray imaging test, the grid was aligned in the center of the target chamber as descried above and then shifted 2 mm off the center towards the crystal in order to place the backlighter source in the center of the target chamber and the crystal itself had then to be shifted by these 2 mm, too. The laser focal point was 1 mm behind the Mg foil target so that the diameter of the laser spot on the target was 1/3 mm. This resulting effective aperture according to Eq. (1.35) was large enough (21 mm) to ensure that the full aperture size of the crystal of 4 mm was used.

Only at two shots was the laser intensity high enough to obtain a reasonable evaluation. The data of these two shots are summarized in Tab. 1.3.

Based on the visible light focal scan, the best focal position for the center was assumed to be at 18000 steps, which is defined as 0–position in Fig. 1.15, as described above. When shifting the crystal by 2 mm, or $+50000$ steps, as it was done for the grid, the best focus should be at 68000, which is beyond the limit of the translation stage (62703).

Shot #24219 was taken at a focal position of 18000 steps. The FWHM of the image

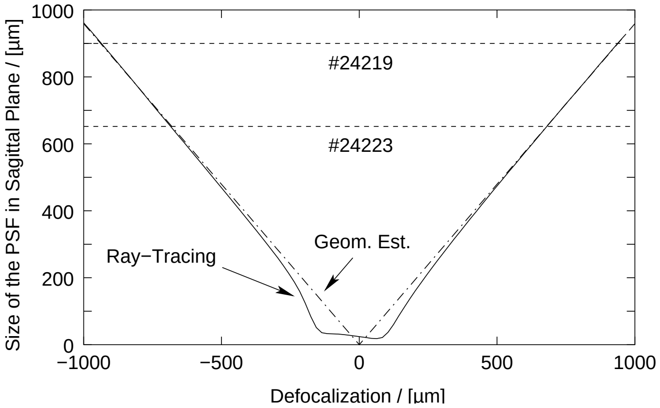

Figure 1.17. The results of the X-ray imaging test: The dashed lines mark the measured widths of the edge profile and the intersection with the calculated solid line gives the possible positions of the focus.

Shot	Rel. Focal pos.		Width of edge		Resol.	Est. misalign.
	[steps]	[mm]	[pixel]	[μm]	[μm]	$\lvert\delta a\rvert$/[mm]
#24219	18000	0.720	40	900.0	24	0.934
#24220	43000	1.720	—	—	—	—
#24223	62703	2.508	29	652.5	17	0.683

Table 1.3. Summary of the X-ray image test.

of the edge in sagittal plane is 40 pixels or 900 μm. From the simulation (Fig. 1.17) as well as Eq. (1.34) one can estimate a de-focalization of ±0.937 mm. At shot #24223 the FWHM of the image of the edge is 29 pixels or 652.5 μm, which would correspond to a defocusing of ±0.683 mm. Between both shots, the focal position was changed by 44703 steps corresponding to 1.789 mm. From Eq. (1.34) follows that these 1.789 mm would cause a broadening of the edge of 87 pixels.

When assuming that both images are lying on the same side of the detector plane, the difference between both edge widths should be 87 pixels, which is contrary to $40 - 29 = 11$ pixels.

However, when assuming that both de-focalized crystal positions are lying on opposite sides of the best focal position, one has to add $40 + 29 = 69$ pixels. This result is in better agreement with the estimated broadening of 87 pixels and the de-focalization distances of ± 0.937 mm (#24219) and ∓ 0.683 mm (#24223): $0.937 + 0.683 = 1.620$ mm compared to the shifted 1.789 mm.

The measured variation of the FWHM of the edge when comparing shot #24219 and #24223 is 405 μm smaller than one would expect from the simulation or the difference in the de-focalization is 169 μm smaller than measured. Defects in the crystal as well as slope errors of the surface would cause a broadening of the edge [68]; also the applied smoothing of the data would cause a broadening. One possibility for this narrowing might be that the translation stage did not move the expected way. However, this is unlikely, since the total distance was checked and the resolution was measured as 0.040 μm/step. Also for the backlash, this difference of 169 μm is too large. The backlash was determined to be less than 1000 steps, corresponding to less than 40 μm.

A shot was taken at a counter value of 43000 (#24220), which is relatively close to the best estimated position of 41350 steps. However, the signal in the image is too weak to distinguish the image from the background as well as the damage structure in the CCD array in order to measure the FWHM of the edge. Also, the edge cannot be uniquely assigned to the sagittal bending radius. However, from the visual impression, the width of the edge of shot #24220 is much broader than one would expect.

Summary

In summary, the detailed analysis of the experimental data of the imaging test has un-covered three mistakes: The test results of the crystals were wrongly marked, no regard was given to the size of the visible light backlighter source, which made a pre-alignment by visible light impossible and third, not mentioned above, due to a software error in the step motor controller, the crystal was shifted only half the way as intended and assumed. After finding and fixing these problems, there was no more beam time available. In this demonstration experiment, only a resolution of 17 μm could be obtained at a de-focalization of $\sim$ 650 μm within the available beam time.

1.3.2 Proposal for an imaging test at an X-ray generator

The ray-tracing calculations in Sec. 1.2.4 predict a very high achievable resolution of as small as 0.08 μm in the sagittal plane using toroidally bent crystals. Even though this result seems to be too optimistic due to the simplifications made for the ray-tracing calculations (perfect shape, only surface reflection, neglecting scattering at small defects in the crystal) and unrealistic to achieve, it is interesting to see which resolution can be actually achieved in an experiment. While the imaging test using the Mg-Lyα line as X-ray source at GEKKO XII was not successful due to the very strict conditions and short available beam time at this high-power laser facility, another imaging test is proposed using an X-ray generator as an X-ray source. Even though the imaging test will be carried out at a wavelength which is unlikely used in a plasma experiment, the advantage is that this demonstration experiment can be done in a small lab.

Besides the aim of observing the highest obtainable resolution, another constraint for the design of the experiment was the aspect of low costs, *i.e.* there should be made use as much as possible of the already available equipment on a small laboratory scale. *I.e.*, as an X-ray source, a conventional X-ray generator should be used. Since it is very difficult—and thus very time consuming—to manufacture a glas replica form with a sufficiently high quality, *i.e.* an error in the radii of $\Delta R/R \sim 10^{-3}$, an existing glas form should be used. Together, the boundary conditions are very restricted since there are only discrete wavelengths of X-Rays available, which give together with the discrete lattice spacings of the crystal, a discrete number of Bragg-angles which has to fulfill Eq. (1.17) for the discrete set of available combinations of bending radii, *i.e.* radii of the glas forms.

In order to solve this problem, a computer program was written which calculates all combinations of characteristic K-shell lines of all elements and lattice planes up to the $(10\,10\,10)$ reflection in the crystal. Another boundary condition is that the structure factor of the crystal does not vanish and should be as high as possible in order to get a high reflectivity of the Bragg reflection and thus a high luminosity of the microscope. Also this lattice plane has to be found in an elastically bendable crystal of 'perfect' quality. Therfore, Si, Ge and Quartz were searched for a suitable lattice plane. For all available glas forms, *i.e.* combinations of banding radii, the stigmatic angle θ_0 obtained by Eq. (1.17) was compared with the Bragg angle, where a misfit of 1.0° was tolerated.

A suitable combination was found in the Ge(224) reflection together with the Cr–$K\alpha$ line: The transition wavelength is $\lambda = 2.289781$ Å, the interplanar lattice spacing $d = 1.154828$, and the resulting Bragg angle $\theta_B = 82.478°$. The structure factor $|F_H| = 144.6$ for the Ge(224) reflection at this wavelength [93].

This fits with the available pair of bending radii of $R_m = 200.0$ mm and $R_s = 195.9$ mm with $\theta_0 = 81.8°$; *i.e.* the misfit $\theta_B - \theta_0 = 0.68°$ corresponding to a misfit in the wavelength of $\lambda_{\mathrm{Cr}_{K\alpha}} - \lambda_{\theta_0} = 0.00374$ Å. Since the spectral window of the crystal $\Delta\lambda \sim 0.0046$ Å at a magnification $M = 30$ and an aperture size of the crystal of 3 mm, the experiment can be carried out at the stigmatic angle θ_0 nevertheless.

The corresponding focal length of these bending radii is $f = 98.98$ mm so that a magnification $M = 30$ is obtained for an object distance $a = 102.28$ mm and an image distance $b = 3068$ mm. Figure 1.18 shows the size of the point spread function in meridional plane and sagittal plane for the here considered configuration, together with the results for the same configuration but a spherical crystal. In sagittal plane, a resolution of 1 μm can be obtained already at an aperture of $\sim$ 9 mm using the toroidally bent crystal, while for the spherical crystal, the aperture has to be smaller than 0.1 mm in order to pass the '1–μm–threshold'. In the meridional plane, both, the result for the toroidal and spherical crystal are in agreement as expected, since in the meridional plane the configuration was not changed. The '1–μm–threshold' is reached at 3.1 mm aperture size.

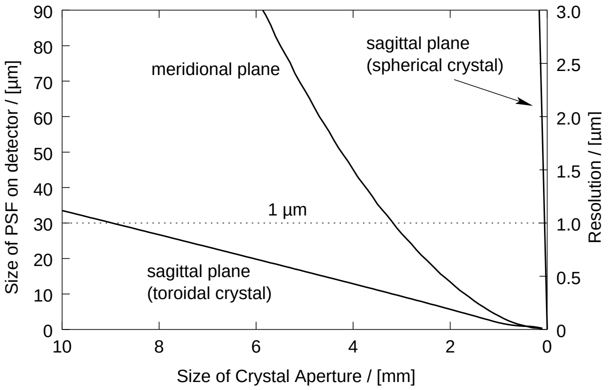

Figure 1.18. The size of the point spread function (PSF) in sagittal and meridional plane for both, a toroidal crystal ($R_m = 200$ mm, $R_s = 195.9$ mm) and a spherical crystal ($R = 200$ mm) at 30× magnification together with the corresponding achievable resolution as a function of the aperture size of the crystal.

Considering now the experimental set-up, a simple geometrical relation shows that for an X-ray source size of 1×1 mm^2 and an intended effective aperture of the crystal of 3 mm, the source has to be placed 25 mm behind the test grid, in order to get a field of view of 1 mm.

The expected flux from the X-ray generator was estimated by the formula of Honkimäki *et al.* [94] as $N/4\pi \sim 2.1 \times 10^{14}$ photons/s for an excitation tension $U = 60$ kV and a current $I = 30$ mA. Thus, a 1 mm^2 large grid in 25 mm distance is illuminated by 3.4×10^{11} photons/s. Together with the efficiency of the crystal, *i.e.* the number of reflected photons compared to the number of emitted photons from the source, (calculated by ray-tracing) of $I/I_0 = 7.1 \times 10^{-7}$, one can expect 2.4×10^5 photons/s on the detector. And since the object size has an area of 1 mm^2, which is 30× magnified, the reflected photons are distributed over 30×30 mm^2 so that the intensity on the detector is $\sim 2.7 \times 10^{-4}$ photons/s/μm^2. A typical value for the required exposure of an X-ray film is 1 photon/μm^2, which leads to a required exposure time of $\sim$ 3700 s, or $\sim$ 1 hour.

A critical point is the absorption in air: Since the linear absorption coefficient of air at normal pressure (1013 mbar) $\mu = 0.0393$/cm, the reflected X-rays would be absorbed on the image distance to $I/I_0 \sim 7 \times 10^{-6}$. Therefore, the reflected X-rays have to be guided in vacuum, where a low vacuum of 1 mbar is sufficient to reduce the absorption to 1.2 %, *i.e.* 98.8 % of the signal is transmitted (*cf.* Ref. *e.g.* [95] together with *e.g.* Ref. [96]).

1.4 Experimental setup

The set up of the experiment is schematically shown in Fig. 1.4 (page 12). As a sample, a 25 μm thick CH plastic plate was used with either a flat surface or an intentionally imposed sinusoidal surface structure. As the driving laser, all twelve beams of GEKKO XII were focalized onto the sample in focal spot size of 600 μm in diameter. The target was irradiated in two steps. In order to keep the initial imprint of the laser on the target (*i.e.* $\xi_0 = \xi(t = 0)$) as small as possible, the target was illuminated in the first 2 ns by three beams of partial coherent light (PCL), each of 25 J in 2ω mode, *i.e.* a wavelength $\lambda = 0.53$ μm, which ensures a very high uniformity of the laser pulse. The remaining nine beams, each of 100 J, were used for the main pulse in 3ω mode ($\lambda = 0.35$ μm), which results in a much higher intensity but a lower uniformity than the PCL pulse, “but still better than a normal laser profile.” [97] Concrete rms numbers for the uniformity of the beam profile are not available here.

As a backlighter source, a Mg foil was placed 10 mm behind the sample. The Mg foil was irradiated with 4×10^{13} W/cm^2 by the Peta-Watt-Module (PW-M) laser as the probe laser in a spot size of 1400 μm diameter. The pulse length was 160 ps with a delay of 2 ns compared to the driving HIPER bundle.

The transmitted intensity was imaged by the above described imager on a streak camera with 200 ps temporal and 100 μm spatial resolution at a distance of 3674 mm, providing a 25.9× magnified image. The imager was aligned by a focal scan using visible light. The effective aperture of the crystal was estimated to be about 3 mm, which was sufficiently large to identify the center of the waist of the curve (*cf.* Section 1.3.1).

1.5 Preliminary results

For the observation of the Rayleigh-Taylor growth rate, only about six shots were scheduled in this experimental campaign due to the large number of concurring ex-

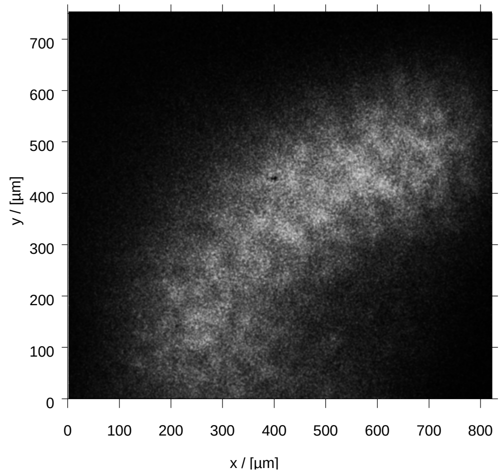

Figure 1.19. The time integrated image of the laser imprint on a flat target. The size of the speckles is in the order of ~ 38 μm.

perimental aims and problems with the laser system. The intensity of these data is very low due to problems with the probe laser. In consequence, the signal to noise ratio is very low, which makes a detailed analysis almost impossible. Nevertheless, the obtained data will be briefly presented here.

First we tried to observe the initial imprint of the laser beam on the target. A flat plastic plate without any initial structure was used as a target. For this part of the experiment, a CCD camera was used as a detector for the HIPER imager, which gave a 2-D spatially resolved but time-integrated image. Only one shot was successful and the resulting image is shown in Fig. 1.19. Despite the signal being very weak, a structure can be observed after image processing. The size of the dominating dark and bright speckles in Fig. 1.19 is in the order of ~ 38 μm. As already mentioned, rms values for the non-uniformity of the incident laser beam are not available here so that it is not possible to compare the spectral power density of the perturbation wavelengths with the non-uniformity of the profile of the laser beam.

The illuminated area in Fig. 1.19 should have a slightly elliptical shape due to the projection sequence. The banana-like shape of the illuminated area, however, points to problems with the probe laser, *i.e.* the beam profile had not the intended circular shape but that banana-like shape. A control image of the beam profile is not available.

Next, we tried to observe the temporal growth of the Rayleigh-Taylor instabilities. Therefore, the CCD camera was replaced by a streak camera with 200 ps temporal and ~ 100 μm spatial resolution. In the first step, a flat plastic plate was used again as a target. However, the obtained signal is too weak to be distinguished from the background noise.

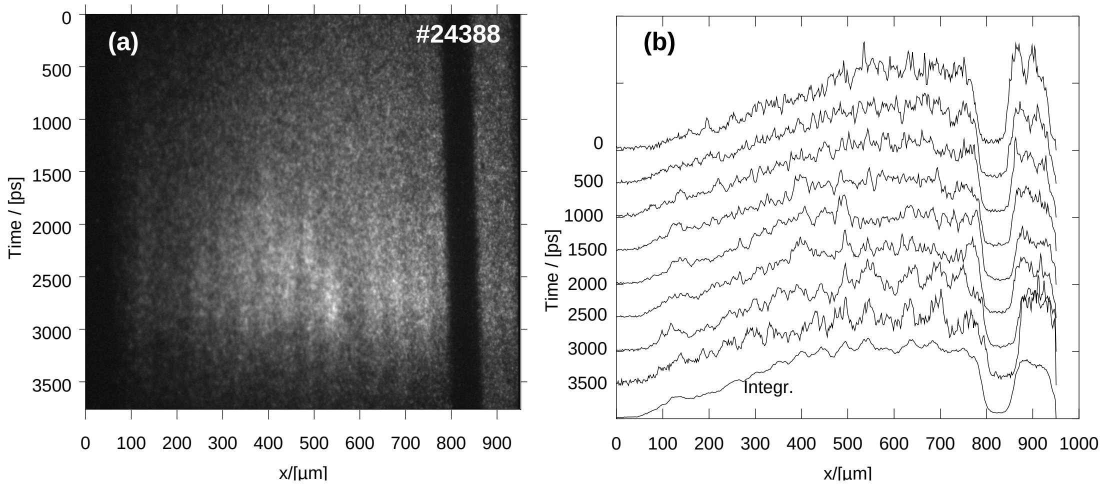

Figure 1.20. The time resolved growth of the Rayleigh-Taylor instabilities of a plastic target with imposed sinusoidal structure of 40 μm wavelength. (a) shows the obtained streak camera image and (b) shows the profiles for different times, integrated over 200 ps.

One reason for the low intensity was the diameter of the probe laser beam profile, which was about twice as large as intended, *i.e.* about 1400 μm instead of 700 μm, so that the intensity was reduced by a factor four compared to the design value. Additionally, the backlighter target was smaller than the beam profile so that only about one fourth of the probe laser beam hit the target, which caused again a reduction in the number of emitted photons by a factor four. For the next shots, the probe laser was re-aligned, but the control image of the backlighter source, taken by a pinhole camera, showed that the problem remained.

In the next step, we used a 25 μm thick plastic plate with an imposed sinusoidal structure on the surface with a wavelength of 40 μm as a target and the aperture of the crystal was opened from 4 mm to 7 mm in order to compensate for the low intensity of the backlighter. The obtained streak camera image is shown in Fig. 1.20(a) and the integrated profile as well as the profiles for different times are shown in Fig. 1.20(b), whereas each profile is integrated over 200 ps. The profiles are normalized to the same integrated intensity in oder to compensate for the varying intensity of the backlighter.

Even though the intensity is too weak for a detailed evaluation by a spectral density analyzation with a reasonable error, the growth of the amplitude can be clearly observed.

1.6 Concluding remarks

The low repetition rates of the high-power laser systems on the one hand and the many open research questions on the other hand let the progress of laser-driven nuclear fusion appear to be very slow. The quest for nuclear fusion is a journey of many little steps to physics which are unknown in the nature on earth [44]. On that way, there are many “unexpected surprises” [12]: As, for instance, Duderstadt and Moses stated in 1982 [4] that by the end of that decade all problems will be solved, the Rayleigh-Taylor instability was no subject. They mentioned only that “some scientists feel that Rayleigh-Taylor instability might be an important issue in the future.” Today, Rayleigh-Taylor instability is a main research issue. The observed stabilization effect, which is much stronger than expected (*cf.* Fig. 1.3), might be due to nonlocal heat conduction by electrons. The nonlocal electrons preheat the main fuel, which raise the fuel adiabat and make the fuel less compressible and thus raising the ignition threshold. Therefore, it is critically important to clearify whether the nonlocal transport still dominates in future targets and whether the preheating of the main fuel by nonlocal electrons can be prevented [63].

The present work is one little step on the way to answer this important question: Even though no high quality experimental data could be obtained within the available time for this work, the imager is a main diagnostic of the HIPER research project at ILE which was started to clearify the above mentioned question for future high-gain targets. The imager is expected to deliver highly resolved data in future experiments, which will help considerably in the understanding of the Rayleigh-Taylor instability and how to mitigate them.

An experimental demonstration of the here shown theoretically possible resolution of sub-micrometers would also find many applications in biology as well as material sciences.

Chapter 2

Diagnostics of X-Ray Laser Plasmas

2.1 Introduction

It is a great challenge to extend the advantages of the laser, *i.e.* high coherence, high natural collimation, small spectral line, and high brilliance in the X-ray regime, since there it is possible to resolve atoms and molecules. Several schemes have been proposed for the pumping of the X-ray lasing medium, of which the collisional scheme is currently considered as the most reliable and robust method for generating high-gain amplified spontaneous emission (ASE) in the X-UV region [98]. In this method, a target material is irradiated with a high power optical pumping laser, stripping the lasing ions to a closed-shell configuration, usually the nickel-like or neon-like ions (Fig. 2.1). For lasing in the Ni-like (or Ne-like) configuration, the conditions in the plasma should optimize simultaneously the fraction of lasing ions and the monopole collisional-excitation rate from the ground state into the $4d$ (or $3p$) manifold so that population inversion is formed on a number of transitions between $4d$ and $4p$ (or $3p$ and $3s$) as the latter is de-populated by rapid radiative decay (*cf.* Fig. 2.1(b)) [98].

The aim of the experimental series presented here is the extension of stable lasing towards the so-called water window [15, 99], *i.e.* the range between the K-absorption edges of carbon and oxygen at 2.31 nm and 4.38 nm, respectively. In this region, the water of biological solutions is relatively transparent while the carbon atoms of the biological molecules absorb very well.

The difficulty in achieving lasing towards shorter wavelengths is that higher Z materials are required with a substantial increase in the requirements in the plasma parameters [100]:

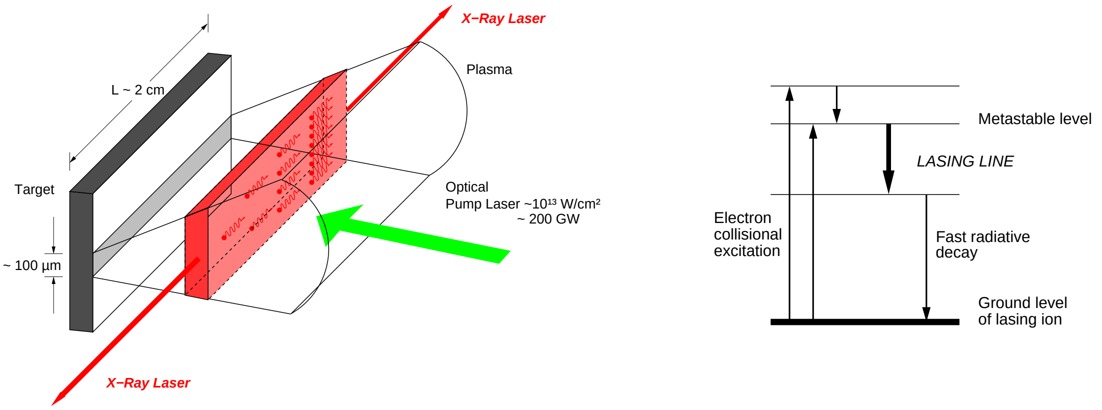

(a) (b)

Figure 2.1. The setup (a) and the inner-atomic processes (b) of the generic collisional X-ray laser experiment.

1. There must be sufficient ionization in order to exceed the Ni-like stage because the monopole excitation rate from the ground state of the Ni-like ions to the upper lasing level maximizes at electron temperatures 2–3 times higher than that at which the maximum Ni-like abundance is realized, whereas a significant proportion of the ions still needs to remain in the Ni-like stages if the laser is to function. Therefore a rapidly ionizing plasma is desired as a gain medium for which the population of the Ni-like 4*d* level, which is the upper lasing level, is maximum.

2. A high plasma density is required for high-atomic-number elements [16]. In the estimation in Fig. 2.2, the maximum density for the population inversion is restricted by the thermal limit of the lasing transitions and opacity effects such as the transition between the lower lasing level and the ground state. The desired electron temperature and density are 1–1.5 keV and 1.5×10^{21} cm^{-3} for ^{70}Yb and 1.4–1.8 keV and 3.5×10^{21} cm^{-3} for ^{74}W, respectively [16]. The higher density provides higher gain, but the duration and width of the gain are smaller, making propagation of the X-ray laser more difficult [101].

3. Finally, X-ray laser beam propagation through the lasing plasmas must be considered. The simplified ray-tracing calculation for X-ray propagation at a wavelength of less than 10 nm through the amplifying medium shows that, in contrast to the case at 20 nm, the obliquely incident X-ray laser beam penetrates into and

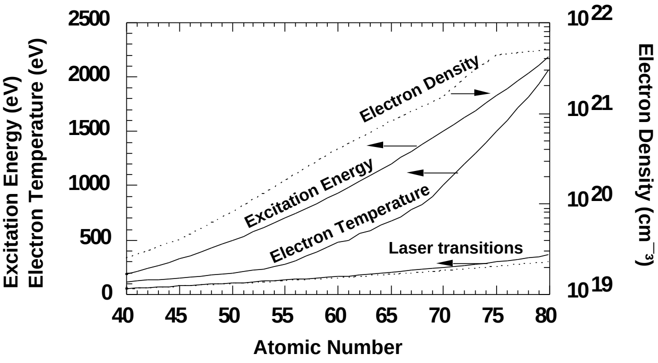

Figure 2.2. The desired plasma parameters for a Ni-like soft X-ray lasing medium as a function of the atomic number [16]

is absorbed in the solid-density plasma and does not refract back to the lower density gain region because the critical density at 10 nm is $\sim 1 \times 10^{25}$ cm^{-3}, which is much higher than that of the solid-density plasma. Therefore the ray at a 20-nm wavelength is easily guided by a controlled refractive-index profile such as a curved target [102], but such guiding does not work well for the short-wavelength X-ray lasers.

Therefore it is most important to produce a homogeneous plasma with appropriate density ρ and scale length $L = [\rho/(d\rho/dz)]_{\text{min}}$ as a gain medium by selection of a prepulse and main pulse with appropriate individual pulse duration [16, 102–104] and wavelength to yield the desired cross section with a long effective gain length. The lasing materials of consideration in this work were Ni-like ^{70}Yb, ^{72}Hf, ^{73}Ta and ^{74}W, whose lasing lines are just before (^{70}Yb – ^{73}Ta) or inside (^{74}W) the water window.

The contribution of the present work to these XRL experiments was the development and appliance of a toroidal crystal spectrometer to the collisional laser plasmas with the aim of a better understanding of the spatial and temporal behavior of the ionization state by the detection of Ni- and Co-like $4f$–$3d$ transitions in the lasing plasmas. These emission lines are particularly interesting for Ni-like XRL, since the intensity of these lines should be related to the inversion population of the lasing transition since the $4f$ level is very close to the 4*d* level, the upper state of the 4*d*–4*p* lasing transition as shown in Fig. 2.3. *I.e.* the $4f$–3*d* transition can serve as an indicator for Ni-like 4*d* ions [16].

Moreover, the lifetime of the $4f$–3*d* transition is relatively short so that a time-resolved observation of the ionization state as a function of the pump-laser pulse train is possible. In addition, the electron temperature and -density can be obtained from the intensity ratio and width of the emission lines, respectively, of the spectra [25, 26].

While the XRL wavelength is around 50 Å, the here observed Ni- and Co-like $4f$–$3d$ transitions lie at about 6 Å, which is roughly one order of magnitude away from the lasing transition. For X-ray optics, this has the advantage that the observation can be done with some ease with *e.g.* perfectly bent Quartz crystals.

The organization of this Chapter is as follows: First, the basics of the determination of the electron temperature and electron density is presented. The requirements and realization of the spectrometer is then presented in Section 2.3 together with the fundamentals and the performance of the spectrometer. Section 2.4 describes then the experimental setup, followed by a description of the data processing before experimental results are presented and discussed.

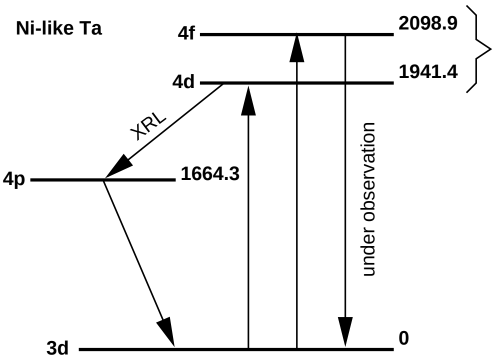

Figure 2.3. Energy level diagram for Ni-like Ta. (Energies are in eV.)

2.2 Determination of plasma parameters

2.2.1 Electron Temperature

In this work the electron temperature of the lasing plasma is obtained by a comparison of the intensity of two spectral lines using the ordinary Boltzmann distribution: The intensity ratio of the emission lines is proportional to the ratio of the population states, which is related by the Boltzmann-distribution

$$\frac{N_1}{N_0} = \frac{g_1}{g_0} e^{-\frac{E_1 - E_0}{k_B T}} \tag{2.1}$$

where N_i are number of particles with energy E_i in the states $i = 0, 1$ and $g_i = (2J_i + 1)$ are the statistical weights, *i.e.* number of states with the same energy E_i.

Since the Ni-like ion has a closed shell, the $4f - 3d$ $(J = 1 - 0)$ transition is split only in three different lines, which can be clearly distinguished. Thus, the calculation of the temperature is very convenient, since it ensures that there is only one transition in one detected line and that these lines have the same ground level, which simplifies the calculation considerably. Otherwise, one would have to calculate the theoretical contribution of the different transitions to the observed "line" and/or apply the Saha-Boltzmann-statistics and compare different ionization stages which might become very difficult or impossible [105].

By comparing the emitted intensity of two single emission lines, we get the relation

$$\frac{N_1}{N_2} = \frac{g_1}{g_2} e^{-\frac{E_{10}-E_{20}}{k_B T}} \tag{2.2}$$

where $E_{i0} = E_1 - E_0$ is the transition energy of the emission line. This expression is now independent of the unobservable number of particles in the ground state N_0. Furthermore, the emitted intensity [106, p. 15f]

$$I_{i0} \propto N_i A_{i0}. \tag{2.3}$$

where A_{i0} is the Einstein coefficient for spontaneous transition from state i to state 0.

Inserting this relation in Eq. (2.2), we obtain

$$\frac{I_{10}}{I_{20}} = \frac{A_{10} g_1}{A_{20} g_2} e^{-\frac{E_{10}-E_{20}}{k_B T}}. \tag{2.4}$$

In the literature, it is more common to give the product $g f_{ij}$ of the statistical weight g and the oscillator strength f_{ij}, where the oscillator strength is related to the Einstein coefficient A_{ij} as [106, p. 34ff]

$$f_{ij} = \frac{m_e h (4\pi\varepsilon_0)}{\pi e^2} \cdot \nu \frac{c^3}{8\pi h \nu^3} \frac{g_i}{g_j} \cdot A_{ij} = \frac{m_e \varepsilon_0 c^3}{2\pi e^2 \nu^2} \frac{g_i}{g_j} A_{ij} \tag{2.5}$$

i.e.

$$A_{i0} \propto g f_{i0} E_{i0}^2 \tag{2.6}$$

so that we can rewrite Eq. (2.4) as

$$\frac{I_{10}}{I_{20}} = \frac{g f_{10} E_{10}^2 g_1}{g f_{20} E_{20}^2 g_2} e^{-\frac{E_{10}-E_{20}}{k_B T}}. \tag{2.7}$$

Isolating $k_B T$, we finally obtain

$$k_B T = -\frac{E_{10} - E_{20}}{\ln\left(\frac{g f_{10} E_{10}^2 g_1}{g f_{20} E_{20}^2 g_2} \frac{I_{20}}{I_{10}}\right)}. \tag{2.8}$$

In our particular case $g_1 = g_2$ so that Eq. (2.8) reduces again to

$$k_B T = -\frac{E_{10} - E_{20}}{\ln\left(\frac{g f_{10} E_{10}^2}{g f_{20} E_{20}^2} \frac{I_{20}}{I_{10}}\right)}. \tag{2.9}$$

This is the final form which was used for computation. While the values for I and E can be directly obtained from the spectra, the gf values have to be calculated quantum-mechanically. Table 2.1 sums up some values from the literature together with the values which were calculated by Dong and Fritzsche [107] in the frame of this work by a multi-configuration Dirac-Fock code.

Table 2.1. Transition probabilities of the observed $3d^94f$ $(J=1)$ – $3d^{10}$ $(J=0)$ transition in Ni–like Yb, Hf, Ta and W ions

Ion	Transition	J_i	J_f	Type	gf^a	gf^b	gf^c	gf^d	$<gf>$
$^{72}\mathrm{Hf}^{44+}$	$3d^9_{3/2}4f_{5/2}-3d^{10}$	1	0	E1	5.71	6.304	5.910	6.14	6.02 ± 0.26
	$3d^9_{5/2}4f_{7/2}-3d^{10}$	1	0	E1	1.78	1.755	1.722	1.67	1.73 ± 0.05
$^{73}\mathrm{Ta}^{45+}$	$3d^9_{3/2}4f_{5/2}-3d^{10}$	1	0	E1	6.06	6.248	5.846	6.09	6.00 ± 0.11
	$3d^9_{5/2}4f_{7/2}-3d^{10}$	1	0	E1	1.87	1.847	1.72	1.76	1.83 ± 0.11
	$3p^5_{3/2}3d^{10}4s_{1/2}-3d^{10}$	1	0	E1	0.350	0.376	0.368	0.347	0.37 ± 0.01
$^{74}\mathrm{W}^{46+}$	$3d^9_{3/2}4f_{5/2}-3d^{10}$	1	0	E1	6.01	6.189	5.815	6.04	6.01 ± 0.15
	$3d^9_{5/2}4f_{7/2}-3d^{10}$	1	0	E1	1.96	1.939	1.900	1.85	1.91 ± 0.05
	$3p^5_{3/2}3d^{10}4s_{1/2}-3d^{10}$	1	0	E1	0.369	0.377	0.368	0.347	0.37 ± 0.01

[a] Ref. [107]: Fritzsche & Dong, 1999
[b] Ref. [108]: Quinet & Biemont, 1991
[c] Ref. [109]: Zhang & Sampson, 1991
[d] Ref. [110]: Zigler *et al.*, 1980

2.2.2 Electron Density

Calculation by the width of the emission line

The electron density of the plasma can be obtained *e.g.* from the width of the emission line. There are three main contributions to the width of the emission line: The natural linewidth, the Doppler broadening and the resonance broadening [23, 24]:

Natural linewidth: The natural width of the emission line is given by the Heisenberg uncertainty relation

$$\Delta E\cdot\Delta t=\Delta E\cdot\tau\geq\hbar/2 \tag{2.10}$$

Table 2.2. Transition wavelengths of the observed $3d^9 4f$ $(J=1)$ – $3d^{10}$ $(J=0)$ transition in Ni–like Yb, Hf, Ta and W ions

Ion	Transition	J_i	J_f	Type	λ/[Å][a]	λ/[Å][b]	λ/[Å][c]	λ/[Å][d]
^{72}Hf^{44+}	$3d^9_{3/2}4f_{5/2} - 3d^{10}$	1	0	E1	6.128	6.126	6.122	6.1322(6)
	$3d^9_{5/2}4f_{7/2} - 3d^{10}$	1	0	E1	6.322	6.323	6.322	6.3225(6)
^{73}Ta^{45+}	$3d^9_{3/2}4f_{5/2} - 3d^{10}$	1	0	E1	5.901	5.900	5.895	5.9041(5)
	$3d^9_{5/2}4f_{7/2} - 3d^{10}$	1	0	E1	6.090	6.092	6.089	6.0892(3)
	$3p^5_{3/2}3d^{10}4s_{1/2} - 3d^{10}$	1	0	E1	6.366	6.365	6.366	6.3713(4)
^{74}W^{46+}	$3d^9_{3/2}4f_{5/2} - 3d^{10}$	1	0	E1	5.686	5.685	5.682	5.692(3)
	$3d^9_{5/2}4f_{7/2} - 3d^{10}$	1	0	E1	5.872	5.873	5.871	5.875(4)
	$3p^5_{3/2}3d^{10}4s_{1/2} - 3d^{10}$	1	0	E1	6.149	6.149	6.150	6.156(4)

---

[a] Ref. [107]: Fritzsche & Dong, 1999

[b] Ref. [108]: Quinet & Biemont, 1991

[c] Ref. [110]: Zigler *et al.*, 1980

[d] Experiment; the number in braces gives the uncertainty in the last digit

where τ is the life time of the excited state. Interpreting the "≥" as "=" we get

$$\Delta E = \hbar \Delta\omega = \frac{\hbar}{2\tau} \tag{2.11}$$

or

$$2\Delta\omega = \frac{1}{\tau} \tag{2.12}$$

where $\Delta\omega$ is the half width at half maximum (HWHM). The life-time τ is given by

$$\frac{1}{\tau} = \sum_j A_{ij} \tag{2.13}$$

the sum of the transition probabilities of all possible spontaneous decays from the upper state [25]. The relative natural line width can then be calculated by

$$\frac{\Delta\omega}{\omega} = \frac{\sum_j A_{ij}}{2} \frac{\hbar}{E}. \tag{2.14}$$

To give a rough number, let us assume that there are no further spontaneous decays from the upper state than the observed and in Tabs. 2.1 and 2.2 tabulated lines. In this case, the $\sum_j A_{ij} = A_{ij} \sim 4 \times 10^{14}$/s for the Ta $3d^9_{3/2}4f_{5/2} - 3d^{10}$ transition, whose transition wavelength $\lambda = 5.90$ Å= 2100 eV, and

$$\frac{\Delta\omega}{\omega} \sim 6 \times 10^{-6}.$$

This linewidth is broadened by two main effects:

Doppler broadening: The Doppler broadening arises straightforwardly from the Doppler shift caused by thermal particle motion. A Maxwellian velocity distribution gives rise to a Gaussian line profile [25]

$$I(\omega) = I(\omega_0) \exp\left(-\frac{(\omega-\omega_0)^2 m_a c^2}{2\omega_0^2 k_B T}\right) \tag{2.15}$$

where m_a is the mass of the atom and $k_B T$ the thermal energy. The resulting relative HWHM is

$$\frac{\Delta\omega}{\omega} = \sqrt{2\ln(2)\frac{k_B T}{m_a c^2}}. \tag{2.16}$$

Inserting the appropriate value for Ta, *i.e.* $m_a = 180.9\ \mathrm{au} = 3.0 \times 10^{-19}$ kg and assuming a thermal energy of 1 keV, we get

$$\frac{\Delta\omega}{\omega} = 9 \times 10^{-9},$$

i.e. compared to a natural line width which is in the order of $10^{-5} - 10^{-6}$ on the one hand and the spectral resolution of the instrument which is in the order of $10^{-3} - 10^{-4}$ on the other hand, we can neglect the Doppler broadening completely.

Resonance broadening: The dominating contribution to the line width is caused by a shorten of the life time of the excited states due to interaction with other ions in the plasma. This broadening is called *collisional* or *Stark broadening* and is proportional to the number of ions per unit volume, since the probability of a collision increases the more ions are around, *i.e.* the higher the plasma density is.

Again, we get the width of the spectral line due to collisions via the Heisenberg uncertainty relation as

$$\Delta\omega = \frac{1}{2\tau} \tag{2.17}$$

where $\Delta\omega$ is the half width at half maximum on the ω-scale and τ is the life-time of the state. This time is equal to the average number of collisions per second and can be calculated by the kinematical gas theory as [23, 24]

$$\frac{1}{\tau} = \pi\rho^2 N\bar{v} \tag{2.18}$$

where N is the density of ions, $\bar{v}$ is the relative velocity of the collision partners and ρ is the distance of the collision partners during the collision, *i.e.* the sum of the radii of the collision partners. This parameter is also called collision- or Weisskopf-parameter in the literature.

It is hard to predict the value of the Weisskopf parameter since we don't know what happens exactly during the collision. However, one can give estimations for the collision parameter. Weisskopf estimates ρ via the mean frequency shift of two classical oscillators which are coupled by their dipole interaction. It is [24]

$$\rho = \sqrt{\frac{1}{2\bar{v}} \frac{c^2 r_e}{\omega_0} f} \tag{2.19}$$

with ω_0 the center frequency and $r_e = e^2/((4\pi\varepsilon_0)m_e c^2) = 2.82 \times 10^{-15}$ m is the classical electron radius and f the oscillator strength.

Combining Equations (2.17), (2.18) and (2.19) we get

$$\Delta\omega = \frac{\pi}{2} \frac{r_e c^2}{\omega_0} f N \tag{2.20}$$

or

$$N = \frac{2}{\pi} \frac{\omega_0}{r_e c^2 f} \Delta\omega. \tag{2.21}$$

There are many more sophisticated ways to estimate the collision parameter (*cf.* Ref. [26] and references herein). However, all estimations assume neutral atoms and are not valid for the present case of highly ionized atoms. For the ionized case, "the detailed calculations are extremely complicated and have been done in detail only for a few atoms. ... Full calculations give the constant of proportionality." [25, p 220]. Therefore, the numbers presented here should be considered as relative numbers.

Calculation by the intensity ratio of the emission lines

For completeness, it should be mentioned that it is also possible to obtain the electron density by comparing the observed emission line intensity with the theoretical expectation by the Boltzmann equation. Due to self-absorption or 'optical thickness', which depends on the electron density, temperature, wavelength and size of the plasma, the observed emission line intensity will differ from this expectation. Thus, it is possible to calculate the electron density by an appropriate model for the self-absorption: When knowing the emission line ratio and the electron temperature as well as the size of the plasma and wavelength of the emission line, the electron density is the only free parameter in the model. This method is described in more detail and applied by Nantel *et al.* in Ref. [105].

The advantage of this method is that it is easy to observe the emission line ratio which is independent of the broadening of the emission line. However, the theoretical effort is considerable and one needs to know the electron temperature of the plasma to be able to compute the Boltzmann equation for the theoretical emission of the X-ray without absorption. But the electron temperature is also obtained from the Boltzmann distribution. Thus, on the one hand, one needs two spectral lines with the same optical thickness for the calculation of the temperature and two other emission lines with strong different optical thicknesses for the calculation of the electron density [105]. Even though simple formulae for the estimation of the opacity for blackbody radiation exist [111, 112], they are of limited use for the charaterization of the line spectra since they are independent of the wavelength. The detailed calculation of the opacities as a function of the wavelength is far beyond the frame of this work and public accessible codes like TOPS [113] are restricted to $Z \leq 30$.

Since on the one hand, the values for the opacities are not accessible and on the other hand, the measured temperature in this work has a very high uncertainty, not at least due to the self-absorption, this method was not applied in this work.

2.3 The Spectrometer

2.3.1 Requirements

For the observation of the $4f-3d$ emission lines, a new spectrometer was designed which should fulfill the following requirements at once: The spectral range of the spectrometer is given by the $4f$–$3d$ transition lines of ^{70}Yb – ^{74}W, which are lying between 5–7 Å so that the spectrometer should cover this range.

The spectra should be recorded either time integrated but spatially resolved or time resolved but spatially integrated. In spatial resolution operation mode, either the homogeneity of the plasmas along the lasing axis or the plasma parameters in blow-off direction should be observed, *i.e.* at which distance from the target and at which density and temperature lasing occurs, while the temporal resolved spectra should be used to observe the influence of the pumping pulse train on the plasma parameters.

For the spatially resolved operation mode, a CCD camera with a pixel size of 22.5 μm should be used, while the time resolved spectra should be recorded with a streak camera with 100 μm spatial resolution for the recording of the spectra. The spectrometer should provide a spatial resolution of $\sim 0.1 - 0.2$ mm since the size of the expanding plasma is in the order of 1–2 mm. In both cases the spectral resolution of the instrument should be $\Delta\lambda/\lambda \lesssim 10^{-3}$.

The spectra should be sufficiently bright to give a reasonable streak camera image with $\Delta t \sim 20$ ps temporal resolution. Due to the use of the streak camera, the spectrometer had to be mounted outside the target chamber, *i.e.* the minimum distance from the source to the spectrometer was given by the radius of the target chamber as about $\gtrsim 750$ mm. Another important aspect for the spectral resolution is the source size which is typically 5–30 mm in XRL experiments and which can not be assumed as point sources.

As explained in the next Sections, only a spectrometer using a toroidally bent crystal can meet all these requirements at once, since one can design the crystal according to the geometrical experimental conditions and the spectral resolution is almost independent of the source size.

2.3.2 The principle of the Johann-type spectrometer

For the diagnostic of the laser produced plasma, a modified version of the Johann spectrometer [114, 115] was used, which offers the possibility to record the whole spectrum at once. This can be done by setting the source inside or outside the Rowland circle [116]. In the only considered case here, where the crystal is placed outside the Rowland circle, the X-rays coming from the source pass the Rowland circle over a large section. Each crossing point can be considered as a point source which is imaged on the opposite side of the Rowland circle (Fig. 2.4).

While the bending radius in the meridional (dispersion) plane R_m is used for spectral focalization, the crystal can be bent perpendicularly to the dispersion plane, too, which can be used for 1-dimensional imaging:

For imaging, the distance from the source to the crystal a and the distance from the crystal to the image b is related by the well-known lens equation [70]

$$\frac{1}{f} = \frac{1}{a} + \frac{1}{b}, \tag{2.22}$$

where f is the focal length of the lens or mirror (crystal). For the bending radius in the sagittal plane R_s, *i.e.* perpendicular to the dispersion plane, f can be approximately expressed by [70]

$$f_s = \frac{R_s}{2\sin\theta} \tag{2.23}$$

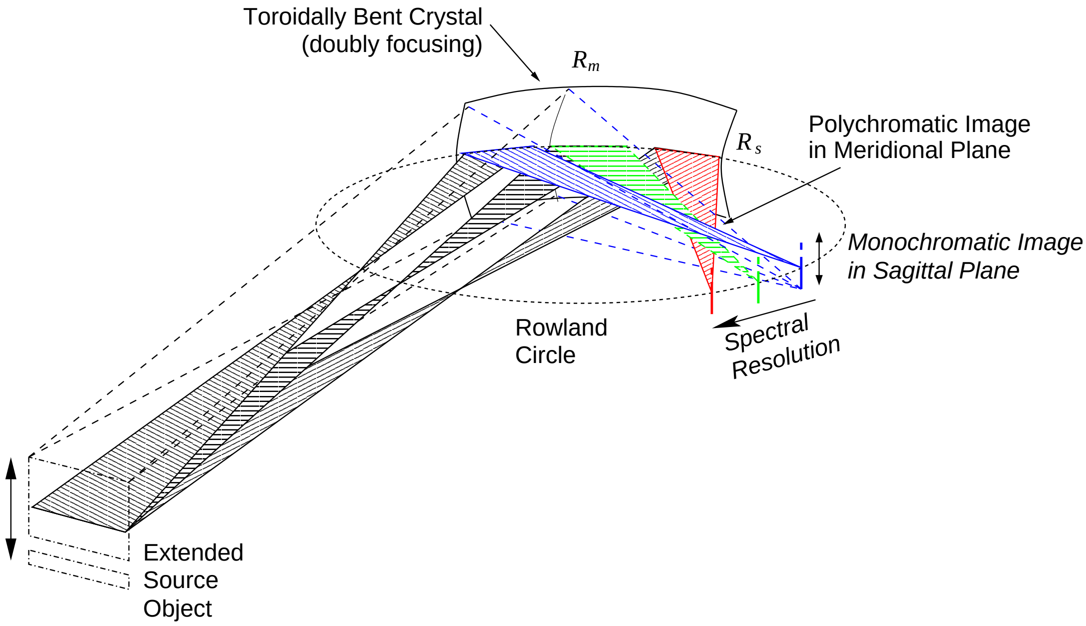

Figure 2.4. Principle of the Johann-type spectrometer

where θ is the angle of incidence. The distance b is given as the distance from the center of the crystal to the focal point of the spectral line on the Rowland circle

$$b = R_m \sin\theta. \tag{2.24}$$

Combining Eqs. (2.22)–(2.24), we find the relation

$$R_s = \frac{2R_m \sin^2\theta \cdot a}{R_m \sin\theta + a}. \tag{2.25}$$

In order to enable the crystal to ‘reflect’ X-rays, θ has to fulfill the Bragg-equation [71, 72]

$$2d \sin\theta = n\lambda, \tag{2.26}$$

too. Here, d is the interplanar lattice spacing, θ the angle of incidence, λ the wavelength of the incident X-rays, and n is an integer number.

From Eq. (2.25), it is clear that R_m and R_s are different, depending on the angle of incidence (Bragg angle) and the object distance. However, some authors [117–120] use spherical crystals *i.e.* $R \equiv R_s = R_m$ for this kind of spectrometer. Thus, the advantages and disadvantages of spherical and toroidally bent crystals should be briefly discussed here:

Spherical Crystals: The advantage of a spherical crystal is that it is easy to manufacture the spherical shape and to align since azimuthal alignment is not needed.

However, according to Eq. (2.25) one has to select the distance a from the source to the crystal as

$$a = \frac{R\sin\theta}{2\sin^2\theta - 1} = -\frac{R\sin\theta}{\cos 2\theta}. \tag{2.27}$$

which limits the experimental setup: For Bragg angles $\theta_B < 45°$, a becomes negative and focussing is not possible: The rays are divergent. For 45° the sagittal rays are parallel so that only the range above 45° remains for focalization. However, in the range $45° < \theta_B \lesssim 47°$, the distance a becomes very large (~ 4 m for $R = 200$ mm and $\theta_B = 46°$) and for $\theta_B \gtrsim 60°$, the distance $a \sim R = 50 \ldots 300$ mm so that the whole spectrometer has to be placed inside the vacuum chamber. This might cause interference with the incident laser beams as well as with other diagnostics. Also, a streak camera cannot be used inside the target chamber. Moreover one has to evacuate and ventilate the vacuum chamber for operation of the spectrometer. Furthermore, the closer the source comes to the Rowland circle, *i.e.* $a \longrightarrow R_m \sin\theta_0$, the smaller the spectral window. If the source is placed on the Rowland circle, the spectral window is given by the source size and the width of the reflection curve only.

Therefore, the reasonable range of Bragg angles is limited to 47°–60°, which presents a further limitation of the experiment, since one has to find a combination of wavelength and crystal reflection which gives a Bragg angle in this range. This is only rarely possible due to the discrete crystal lattice spacings d, which must be furthermore found in an elastic bendable crystal.

To work around the '45°-problem' mentioned above, Young *et al.* [120] placed the detector outside the Rowland circle at

$$b = \frac{Ra}{2a\sin\theta - R} \tag{2.28}$$

so that the detector is at the image distance in the sagittal plane. Depending on a and R, the critical angle, at which and below imaging is not possible, is now shifted to smaller values but the above mentioned discussion remains valid and the independence of the spectral resolution from the source size is sacrificed since the source is imaged 2-dimensionally at the detector and therefore, the spectral resolution is determined by the size of the image of the source. In the case of quasi-point sources (< 10 μm) this gives still good results but is not applicable for the 5–30 mm long targets used for X-ray laser experiments.

Toroidal Crystals: These problems can be avoided by using a toroidally bent crystal, where both bending radii can be determined independently according to the experimental conditions. The distance a can be freely chosen so that the crystal is outside the target chamber. This is convenient for operation of the spectrometer and excludes interference with other diagnostics or laser beams.

The bending radius R_m has then to be selected as a compromise between magnification, spectral window and spectral resolution, where the magnification

$$M = \frac{b}{a} = \frac{R_m \sin\theta}{a}, \tag{2.29}$$

the spectral window approximately (*cf.* Sec. 1.2.2)

$$\Delta\lambda = A_m \cos\theta \left(\frac{1}{a} - \frac{1}{R_m \sin\theta} \right) \lambda, \tag{2.30}$$

and the spectral dispersion [114]

$$\frac{\mathrm{d}\lambda}{\mathrm{d}s} \approx \frac{\lambda}{R_m \tan\theta}, \tag{2.31}$$

where ds is the length element along the Rowland circle.

When R_m and a are selected and θ is determined by the Bragg angle θ_B resulting of the desired wavelength λ and chosen crystal reflection, R_s can be calculated by Eq. (2.25).

The disadvantage of the toroidally bent crystal is that it is much more difficult to manufacture the toroidal shape. To ensure $\Delta R/R \leq 10^{-3}$ for both bending radii in order to obtain good spectral and spatial resolution, the production process requires extensive and time consuming quality controls during manufacturing of the glas forms [91]. Currently only the X-ray optics group at the University of Jena is able to manufacture such crystals.

In summary, toroidally bent crystals can be designed according to the experimental requirements but are more difficult to manufacture, while for spherical crystals the experiment has to be designed to fit the geometrical requirements of the crystal.

2.3.3 Design

An image of the spectrometer is shown in Fig. 2.5 and the geometry of the spectrometer is summarized in Table 2.4.

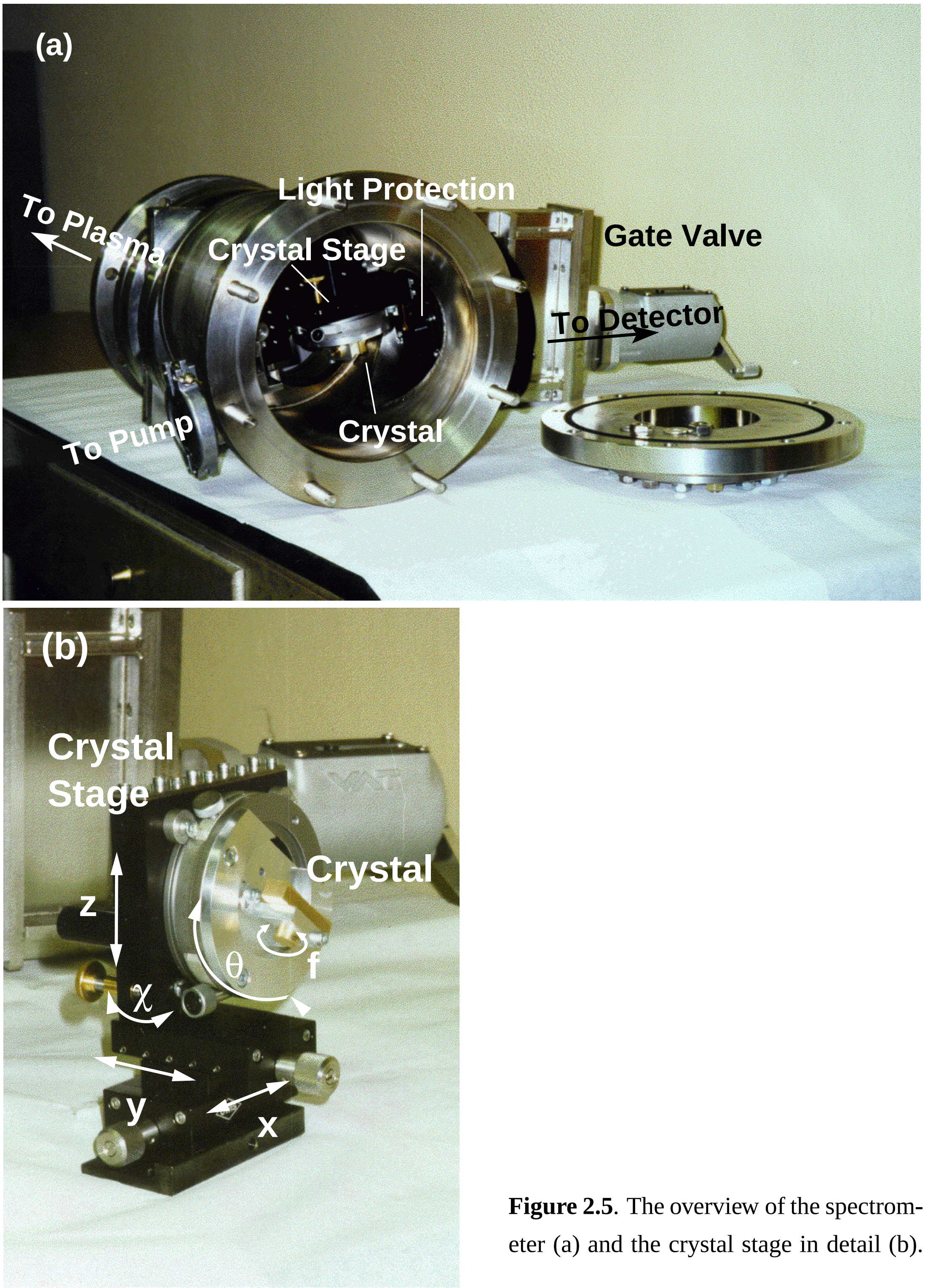

Figure 2.5. The overview of the spectrometer (a) and the crystal stage in detail (b).

As a design value, a central operation wavelength of 6.0 Å of the spectrometer was assumed and a suitable crystal lattice plane was found in the Quartz $(10\bar{1}0)$ reflection with an interplanar distance $d = 4.2548174$ Å, resulting in a central Bragg angle $\theta_{B,0} = 45°$. [1]

For the operation with the CCD-camera, the crystal was bent to a toroidal shape as described in detail by Förster *et al.* [121] with $R_m = 200.0$ mm and $R_s = 177.7$ mm. For the use of the spectrometer in connection with the streak camera, another crystal was prepared with $R_m = 300.0$ mm and $R_s = 278.0$ mm. The larger bending radii here compared to the crystal for the CCD camera was necessary since the distance from the connecting flange to the photo cathode, *i.e.* detector plane, is larger than that for the CCD camera on the one hand, and on the other hand to conserve the high spectral resolution, which is, among others, proportional to the spatial resolution of the detector divided by the distance to the crystal at the same Bragg angle.

These bending radii were chosen so that the crystal can be placed conveniently outside at the target chamber wall at a distance of 1162 mm from the source while having enough space to mount the detector on the spectrometer.

The crystal was mounted on a goniometer which again was mounted on a translation stage so that the crystal can be shifted in direction of the plasma, in direction to the detector and perpendicular to this plane. Moreover, the crystal can be tilted due to a tilting mechanism between the goniometer and the translation stages.

In the central position, *i.e.* at a central Bragg angle of 45°, the spectral window reaches from 5.536 Å to 6.458 Å for the crystal with $R_m = 200$ mm. In order to access the full required range from 5–7 Å, the central Bragg angle can be shifted according to the used target material. However, when rotating the crystal off the design position, the detector will be no longer on the Rowland circle. Thus the crystal has to be shifted in direction of the optical axis, too. Table 2.3 gives the amount of the necessary shift in each direction relative to the 45°–position together with the resulting spectral window. *I.e.* in the center position the spectral window reaches from 5.536 Å to 6.458 Å. This window is appropriate for the Ta- and W-spectrum, where the $4f-3d$ emission lines reach from 5.68 Å to 6.37 Å. In order to be able to observe the Ni-like Yb $4f-3d$ emission lines, which are lying in the range from 6.62 Å to 6.92 Å, the crystal has to be turned by 7° so that the central angle of incidence is 52° which gives a spectral

---

[1] Note, that it is impossible to construct such an imaging spectrometer by means of spherical crystals, since the central Bragg angle is 45° (*cf.* Sec. 2.3.2).

$\theta_{B,0}$ [°]	a [mm]	Δa [mm]	b [mm]	Δb [mm]	$\theta_{B,\mathrm{min}}$ [°]	$\theta_{B,\mathrm{max}}$ [°]	λ_{min} [Å]	λ_{max} [Å]
40	1141.4	−20.6	128.6	−14.4	35.54	44.41	4.946	5.955
41	1145.1	−16.9	131.2	−11.1	36.55	45.41	5.068	6.060
42	1149.0	−13.0	133.8	−8.23	37.56	46.40	5.187	6.162
43	1153.1	−8.9	136.4	−5.3	38.57	47.39	5.305	6.262
44	1157.5	−4.5	138.9	−2.6	39.58	48.38	5.422	6.362
45	**1162.0**	**±0.0**	**141.4**	**±0.0**	**40.59**	**49.37**	**5.536**	**6.458**
46	1166.7	+4.7	143.9	+2.5	41.60	50.36	5.649	6.553
47	1171.7	+9.7	146.3	+4.5	42.60	51.36	5.760	6.647
48	1176.7	+14.7	148.6	+6.5	43.61	52.35	5.870	6.738
49	1182.0	+20.0	150.9	+8.2	44.62	53.34	5.977	6.827
50	1187.4	+25.4	153.2	+9.7	45.63	54.34	6.083	6.914
51	1193.0	+31.0	155.4	+10.9	46.63	55.33	6.186	7.000
52	1198.7	+36.7	157.6	+11.9	47.64	56.33	6.288	7.082
53	1204.5	+42.4	159.7	+12.6	48.65	57.32	6.388	7.163

Table 2.3. The spectral window of the spectrometer and the necessary shift of the crystal for different central Bragg angles $\theta_{B,0}$. Note the difference in $\Delta b \neq 141.4 - b$. Δb is the shift parallel to the normal of the CCD, while $b = R_m \sin\theta_{B,0}$ gives the distance from the center of the crystal to the detector.

window from 6.29 Å to 7.08 Å. In order to ensure that the detector is again on the Rowland circle and to obtain a sharp image of the source, the crystal as to be shifted additionally 11.9 mm perpendicular to the detector plane away from the detector and 36.7 mm away from the source.

Two 10 μm thin Mylar foils (Mylar: $C_{10}H_4O_8, \rho = 1.39$ g/cm^3) each with 200 nm Al on it were mounted between the crystal and the CCD array to protect the CCD from saturation by visible light.

The total throughput of the spectrometer, *i.e.* the total number of transmitted photons compared to the number of emitted photons from the plasma in 4π, for the 35×10 mm^2 large crystal as a function of the wavelength is shown in Fig. 2.6 together with the integrated reflectivity of the crystal and the transmittivity of the light protection foil. The integrated reflectivity of the crystal was calculated using the Takagi-Taupin equation [83, 84] while the total throughput was obtained by the ray-tracing code T-Ray [81] under use of the transmission coefficient of the light protection foil which was calculated by the XPower code [122–124] based on the Evaluated Photon Data

Type of detector		CCD-Array	Streak-Camera
Picture element size of detector		22.5 μm	100 μm
Crystal		Quartz $(10\bar{1}0)$	Quartz $(10\bar{1}0)$
Lattice spacing	d	4.2548174 Å	4.2548174 Å
Central Wavelength	λ_0	$\sim$ 6.0 Å	$\sim$ 6.0Å
Central Bragg-angle	$\theta_{B,0}$	$\sim$ 45°	$\sim$ 45°
Bending radius in meridional plane	R_m	200.0 mm	300.0 mm
Bending radius in sagittal plane	R_s	177.7 mm	278.0 mm
Size in meridional plane	A_m	35 mm	30 mm
Size in sagittal plane	A_s	10 mm	10 mm
Object distance	a	1162.0 mm	1162 mm
Image distance	b	141.4 mm	212.1 mm

Table 2.4. The design parameters of the spectrometer.

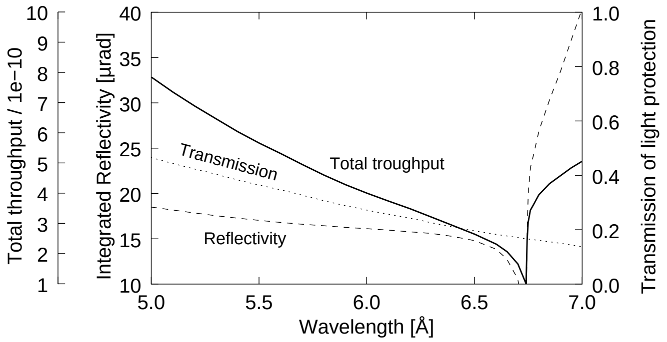

Figure 2.6. The integrated reflectivity of Quartz $(10\bar{1}0)$ (- - -), the transmittivity of the light protection foil (······) and the absolute throughput of the spectrometer (——). The Si K-absorption edge is at 6.7420 Å.

Library [125]. Knowing the total throughput, it is possible to measure the absolute number of emitted photons from the source when using a calibrated detector.

The throughput of the spectrometer can be controlled by changing the aperture size of the crystal in the sagittal plane by means of a slit, which can be easily made by a copper foil for instance and mounted on the crystal. This has the advantage that the throughput can be controlled independently from the spectral sensitivity of the spectrometer contrary to the use of filters, where the amount of transmission depends on the wavelength.

A critical point of the spectrometer might be the Si K-absorption edge at 6.742 Å of the Quartz crystal, where the reflectivity of the crystal decreases considerably. All here presented data, however, are taken below this absorption edge.

2.3.4 Characterization of the performance of the spectrometer

In the case of the original Johann spectrometer with a cylindrically bent crystal and the source on the Rowland circle, the spectral resolution is, beside the width of the reflection curve, the vertical divergence, and the thickness of the film, limited by the Johann error only, which is almost negligible [114]. Neglecting the Johann-error, each point of the source is imaged on the opposite side of the crystal, *i.e.* the polychromatic image of each source point is lying on the opposite side of the Rowland circle. The spectral range of this polychromatic image is given by the width of the reflection curve, only. When bending a film along the Rowland circle it is ensured that each image point is lying on the detector.

However, when placing the source outside the Rowland circle, the geometry becomes more complicated, and a ‘modern’ detector like a CCD- or streak camera cannot be bent along the Rowland circle. Thus, the detector has to be placed *e.g.* perpendicular to the central beam. In the following, the analysis of the influence of these geometrical aspects is discussed.

General

The simulations in this section are restricted to a central Bragg angle of 45° and the here accessible spectral range of 5.7 Å to 6.4 Å with the source placed outside the Rowland circle at a distance of 1162 mm away from a Quartz $(10\bar{1}0)$ crystal with bending radii of $R_m = 200$ mm and $R_s = 177.7$ mm and the detector at a distance of

141.4 mm (*cf.* Tab. 2.4 for the case of the CCD array). This restriction is made because on the one hand, this is the only configuration used in this work and on the other hand, the crystal has to be turned and shifted in order to access the full range from 5–7 Å so that the discussion of the resulting new spectral window is analogue to the following discussion except that the central Bragg angle is shifted.

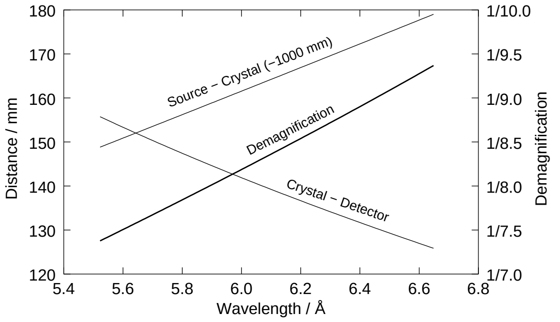

Figure 2.7. Distances of the spectrometer in the meridional plane as a function of the wavelength together with the resulting demagnification.

Figure 2.7 gives a summary of the distances of the spectrometer geometry for a point source in the meridional plane. Depending on the wavelength, the X-rays are diffracted on different places on the crystal (*cf.* Fig. 2.4), *i.e.* the distance from the source point to the point of reflection on the crystal varies between 1179 mm to 1149 mm for 6.648 Å to 5.522 Å, respectively. *I.e.* the longer the wavelength, the longer the distance. The distance from the point of reflection to the point of intersection with the detector, however, changes in the opposite way from 126 mm to 156 mm for the same wavelength range. *I.e.* the longer the wavelength, the shorter the distance. Thus, the (de)magnification of the image in the sagittal plane changes accordingly from 1/9.4 to 1/7.4 for 6.648 Å to 5.522 Å, respectively (Fig. 2.7).

Monochromatic point source

For the characterization of the spectral and spatial resolution of the spectrometer, the problem is restricted first to the spectroscopy of a monochromatic point source:

Since the crystal ‘reflects’ not only X-rays of a single wavelength under a single angle, the above (Section 2.3.2) mentioned consideration of the extended source as a point source on the Rowland circle is not correct. Rather, the imagined source on the Rowland circle will have a finite width, given by the angular range of acceptance of the crystal together with the distance from the surface of the crystal to the Rowland circle and the slope of the Rowland circle relative to this ‘ray’. Thus, the image of the imagined ‘point source’ on the Rowland circle will have a finite width, too, which limits the spectral resolution of the spectrometer. Even a point source outside the Rowland circle has to be considered as an extended source on the Rowland circle, due

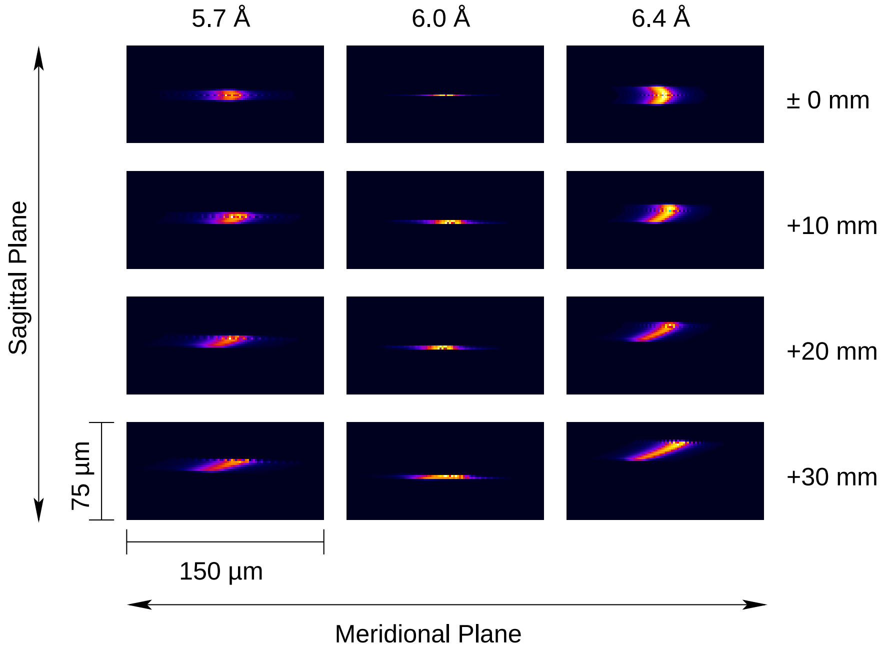

Figure 2.8. The calculated point spread function of the spectrometer for selected wavelengths and displacements of the source in the sagittal plane for the crystal with $R_m = 200$ mm (*cf.* Tab. 2.4). Note, that this simulation was calculated with a pixel size of 1.5 μm while the real CCD-array has a pixel size of 22.5 μm.

to this angular range of acceptance.

For the case of a monochromatic point source, the imagined source size on the Rowland circle will be about 15 μm for the here considered case at 6.0 Å, corresponding to $\Delta\lambda/\lambda \sim 1.1 \times 10^{-4}$ (*cf.* Fig. 2.8 top middle). This broadening is directly due to the width of the reflection curve.

However, the spectral resolution depends on the wavelength, too. For the point source in the meridional plane, the 'monochromatic focus' becomes smaller for longer wavelengths. The reason for this is that the cross section of the Rowland circle through the angular range of acceptance of the crystal, *i.e.* the imagined source size, is smaller for longer wavelengths due to the steeper angle at which the Rowland circle crosses the opening angle. In consequence, the image of the imagined source will be smaller, too.

Figure 2.8 shows representative calculated images of a point source on the detector for three wavelengths. The corresponding quantitative numbers for the full width at half maximum (FWHM) of the spot size in the meridional and the sagittal planes are

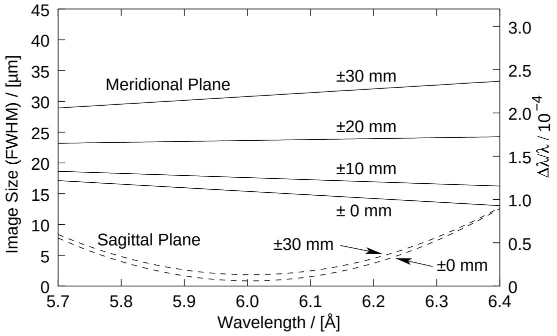

Figure 2.9. Resolution of the spectrometer for a point source. The solid lines show the image size in the meridional plane for different displacements perpendicular to it together with the corresponding spectral resolution (right ordinate) and the dashed lines mark the spatial resolution of the spectrometer in the sagittal plane.

shown in Fig. 2.9 as a function of the wavelength together with the corresponding spectral resolution of the spot size in the meridional plane on the right hand ordinate.

In the sagittal plane, however, the image is broadened for all wavelengths beside the design wavelength, since only in that case, the image of the source is lying in the detector plane. In all other cases, the image is lying in front of or behind the detector plane, which causes in each case a broadening of the image.

When the point source is now shifted perpendicular to the meridional plane, the size of the spot on the detector increases, since the deviation of the optimal focus from the detector plane increases. In the sagittal plane, this broadening is small, but it is much larger in the meridional plane, as shown in Figs. 2.8 and 2.9. For a deviation of ±20 mm away from the meridional plane, this increasing of the broadening of the image due to the de-focalization compensates the above described narrowing due to the smaller imagined source size, and for a deviation of ±30 mm, this broadening towards longer wavelengths exceeds the above described narrowing in this wavelength direction (Fig. 2.9).

Monochromatic extended line source

For the next step of the characterization of the spectrometer, a monochromatic line source with the extension in the diffraction plane is assumed: The source has no extension in the sagittal plane, since there the crystal is used in imaging geometry (*cf.* Sec. 1.2.2) so that the image of a point is the appropriate description of the spatial resolution. In the meridional (diffraction) plane, the consideration of an extended source is necessary since there, the radiation emitted at different source points incidents onto the crystal under different angles. This has two effects for a monochromatic source: First, the radiation coming from another point of the source cannot be reflected at the crystal

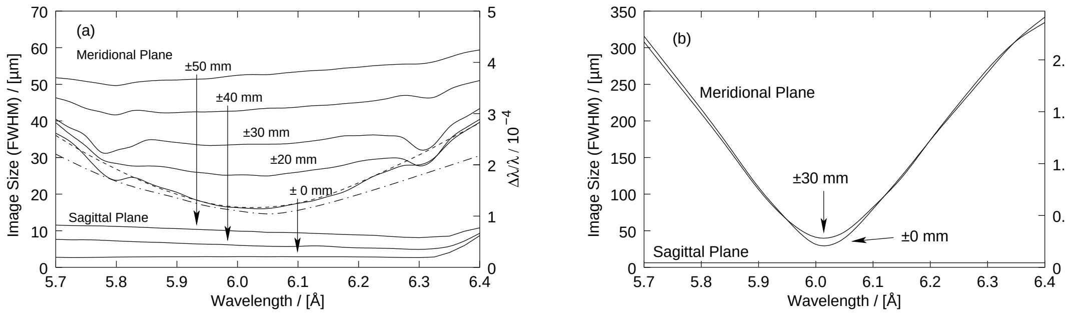

Figure 2.10. The size in both the meridional and the sagittal plane of the image of a line source. (a) length 2 mm, (b) length 20 mm. The different lines refer to different deviation of the source from the meridional plane. While the solid and dotted line refers to a sagittal aperture size of 10 mm, the dash-dotted and dashed lines refers to a the sagittal aperture size of 1 mm and a shift of ±0 mm and ±50 mm, respectively.

in the meridional plane, since there the Bragg condition (Eq. (2.26)) cannot be fulfilled. However, second, the Bragg condition can be fulfilled off the meridional plane [22]. This causes an influence in the ‘image’ on the detector in both, the meridional and the sagittal plane.

In other words: If the crystal would have just an extension in the meridional plane, the source size would be limited by the angular width of the reflection curve of the crystal. Consequently, the case of the monochromatic point source would apply, because the X-rays, which would come from a source point outside this ‘acceptance angle’, would not be diffracted at the crystal. For a two dimensional extended bent crystal however, the X-rays from a source point outside the ‘opening angle’ in the meridional plane can be incident in the sagittal plane under the correct Bragg angle relative to the surface of the crystal (*cf.* Ref. [22, 73]) and there be diffracted. Since this point of intersection will not lie perpendicular to the Bragg-angle position in the meridional plane, the considerations in Section 2.3.2 are no longer valid, because they assume a clear distinction for the spectral focalization in the meridional and the imaging in the sagittal plane. For the case of an extended source which is diffracted at an extended crystal in the sagittal plane, this clear distinction is not given anymore.

The distortion of the image of a point source due to the extended crystal can be observed in Fig. 2.8. However, even though the broadening of the image size relative to the center position (*i.e.* 6.0 Å on the optical axis) is large as shown in Fig. 2.9, it is small compared to the requirements and the resolution of the CCD array.

For an extended source however, the resulting FWHM of the 'image' size on the detector might become a complicated shape. In Fig. 2.10(a) the FWHM for a 2 mm long line source, lying in the meridional plane, is shown for several deviations of the source perpendicular to the meridional plane. In the X-ray laser experiment, this source size is realized when the longitudinal extension of the plasma is perpendicular to the meridional plane as shown in Fig. 2.15. The solid lines in Fig. 2.10(a) are the results of the ray-tracing calculation for a the sagittal crystal aperture of 10 mm. For 'small' deviations a parabolic basic shape is obtained for the FWHM of the image size in the meridional plane with dips at $\sim$ 5.8 Å and $\sim$ 6.3 Å. These dips are due to the complicated beam cross section coming from the outer region of the crystal (*cf.* Section 1.2.4 and there particularly Fig. 1.8 on page 24). An analytical description of this relation can be found at Dirksmöller [74]. If the source is deviated farther away from the the meridional plane, the FWHM of the image on the detector in the meridional plane is more and more broadened, and the dips are superpositioned by other influences.

However, even though the influences of the source size on the image on the detector are large, the broadening of the image is still comparable to the resolution of the CCD array: The size of the image on the detector in the meridional plane varies between 16 μm (at 6.0 Å, where the detector intersects with the Rowland circle, and without deviation from the meridional plane) and 60 μm (6.4 Å and 50 mm deviation from the meridional plane), corresponding to 1–3 pixels of 22.5 μm size, or $\Delta\lambda/\lambda \sim (1.1 - 4.2) \times 10^{-4}$. In the sagittal plane, the maximum image size amounts 11.6 μm, which is smaller than the size of one pixel so that the resolution here is limited by the pixel size only.

To get some evidence that the broadening and complicated shape is due to the sagittal aperture of the crystal, the calculations were carried out again with the same parameters but the sagittal aperture of the crystal was reduced to 1 mm. The resulting FWHM of the image in the meridional plane is shown in 2.10(a), too, for a deviation of the source from the meridional plane of $\pm$0 mm (dash-dotted line) and $\pm$50 mm (dashed line) respectively. As expected, the dips at $\sim$ 5.8 Å and $\sim$ 6.3 Å vanish, which are due to the outer regions of the toroidal shape of crystal surface. Also, the image size in the meridional plane is reduced, *i.e.* the spectral resolution is increased. Moreover, the difference between the FWHM of the image in the meridional plane for the case with and without a deviation of $\pm$50 mm is reduced.

Figure 2.10(b) shows the FWHM of the image size of a 20 mm long line source lying in dispersion plane as a function of the wavelength. This case is given, if the spectrometer is aligned so that the longitudinal extension of the plasma column is lying in the dispersion plane and the blow-off direction of the plasma is imaged, *i.e.* similar to the set-up of Fig. 2.12.

Here, the size of the focal spot in the meridional plane is dominated by the source size, which makes the fine structures (dips) in the curve invisible. The behavior of the curve can be understood as the deviation of the detector plane from Rowland circle towards or away from the polychromatic image of the source in the meridional plane (*cf.* 1.2.2, and there Eq. (1.16)). This polychromatic image is desired for the 2-D imaging, but here for the spectrometer rather a nuisance. At 6.0 Å, where the detector intersects with the Rowland circle, the image size on the detector has its minimum, and ideally (for the case that the FWHM of the reflection curve would be zero), the FWHM should become zero here according to Section 2.3.2. For longer and shorter wavelengths, the detector is deviated from the Rowland circle, where the bunch of diffracted X-rays becomes larger (*cf.* Fig. 2.4 on page 61). The image size in the meridional plane varies between 35 μm and 334 μm for 6.0 Å and 6.4 Å, respectively (*cf.* Fig. 2.11). The corresponding spectral resolution amounts to 2.5×10^{-4} to 2.4×10^{-3}, respectively.

Figure 2.11 shows the influence of the sagittal aperture of the crystal for a 20 mm long line source which is deviated by 30 mm off the meridional plane. The upper part shows the ray-tracing results for a sagittal crystal aperture of 1 mm and the lower part the results for 10 mm sagittal crystal aperture. The intensity in each image is scaled to its maximum, whereas the maximum intensity as well as the integrated intensity is reduced by a factor ten for the image calculated for 1 mm sagittal aperture compared to 10 mm sagittal aperture.

At a sagittal aperture of 1 mm, the profiles of the image in the meridional plane for shifts of ±0 mm and ±30 mm, are identical. However, amazingly, if the sagittal aperture is reduced from 10 mm to 1 mm, the FWHM of the image in sagittal plane increases from a FWHM of about 6 μm for 10 mm sagittal aperture to 66–87 μm for 1 mm sagittal aperture, depending on the wavelength. This broadening in the sagittal plane at a smaller aperture size is counter-intuitive but can be understood as follows. Due to the smaller sagittal aperture, the diffracted intensity is decreased and the image is sharper. However, the main reduction in intensity is in the focus so that the maxi-

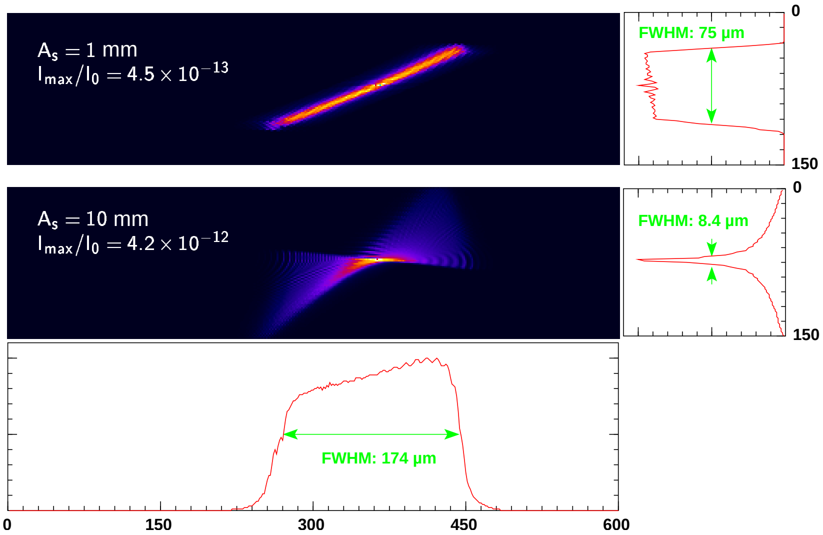

Figure 2.11. The image of a 20 mm long line source for a sagittal aperture $A_s = 1$ mm and $A_s = 10$ mm. The wavelength is 6.2 Å, and the deviation from the meridional plane amounts +30 mm. In both cases, the same profile in the meridional plane is obtained.

mum intensity is reduced and accordingly the full width of the image at the reduced maximum intensity is enlarged.

However, even for the very large plasma sizes expected in the X-ray laser experiments, the influence of the source size discussed here on the spectral and spatial resolution is relatively small compared to the resolution of the detector, the size of the plasma, and its huge deviation from the meridional plane. Even for the very large 20 mm long plasma column in dispersion plane deviated by 30 mm, a spectral resolution of better than 3×10^{-3} can be obtained, which is in the required range of about $10^{-3} - 10^{-4}$. The spatial resolution, however, is better than the real resolution of the CCD array, which is at least two pixels.

Measurement of the spatial resolution

Figure 2.12 presents the experimental demonstration of the spatial resolution of the spectrometer. Figure 2.12(a) shows the raw CCD image of the Al calibration spectrum, which was taken with the CCD array at the intended distance and Fig. 2.12(b) shows the spatial profile of the plasma, integrated over the full recorded spectrum: The incident laser beam comes from the left hand side, in which the plasma is expanded. On the right hand side of the profile, the solid target edge is visible. Using this edge,

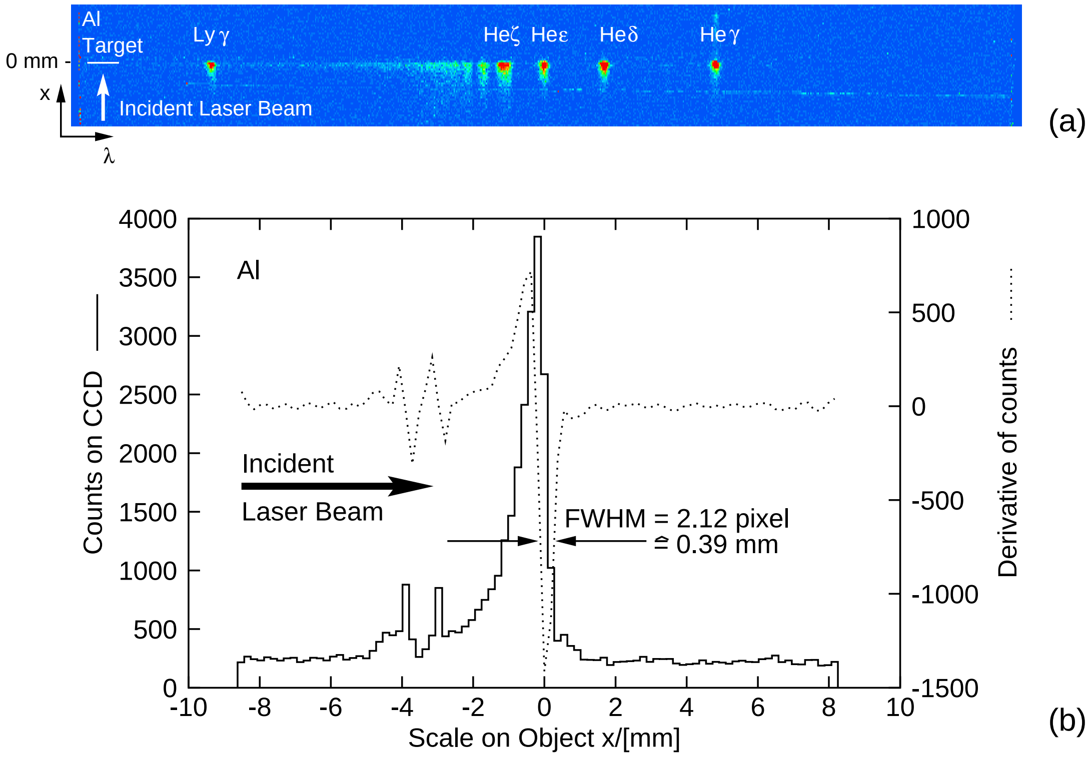

Figure 2.12. Demonstration of the spatial resolution of the instrument (raw data). The spikes in (b) at the left hand side of the spatial profile are due to defects in the CCD array.

the real spatial resolution can be measured as the FWHM of the derivative of the edge with respect to x (dotted line in Fig. 2.12(b)). From the presented data in Fig. 2.12, a spatial resolution of Δx = 2.12 pixel = 47.7 μm on the CCD array or 393 μm on the target was obtained, which is in accordance with the physical resolution of the CCD array of about two pixels.

2.3.5 Calibration

The spectral dispersion relation of the spectrometer was calculated by a ray-tracing code, which was developed especially for this purpose: A ray starting at the source point hits the crystal, is symmetrically reflected there and hits the detector. The position of the point of intersection on the detector in relation to the angle of incidence and reflection on the crystal gives the dispersion relation, where the angle of incidence equals the Bragg angle (neglecting the refraction inside the crystal). The corresponding wavelength can be obtained then from the Bragg angle using the well-known Bragg equation (Eq. (2.26)). Thus, the dispersion relation is well-defined, when knowing the geometrical distances and angles of the spectrometer. The advantage of this method compared to a single analytical formula is that this is much easier to obtain and it takes automatically into account all imaging errors like the Johann error or distortion of the image. Additionally, this approach is very easy to modify in order to test several set-ups or to apply it to another geometry.

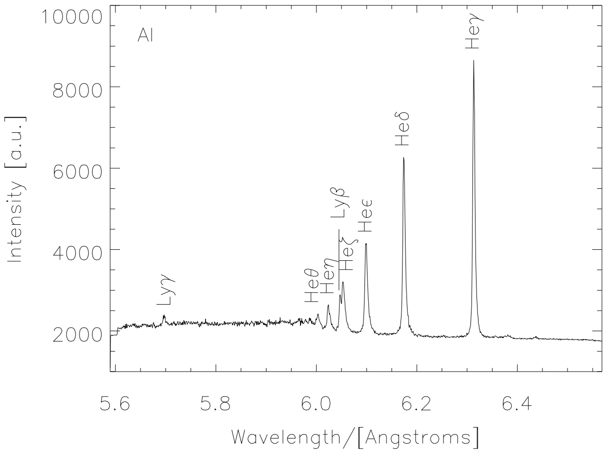

Figure 2.13. The Al-spectrum used for the *in-situ* calibration of the spectrometer

In order to obtain the precise values of the essential parameters, the observed positions of the H- and He-like transition lines of an Al-reference spectrum (Fig. 2.13) were compared with the tabulated wavelengths in Ref. [126] using the Levenberg-Marquardt method [127]. Knowing these parameters, the dispersion relation is well defined. Table 2.5 summarizes the observed pixel position on the CCD array together with the corresponding wavelength and the in turn numerically computed values λ_{Fit}

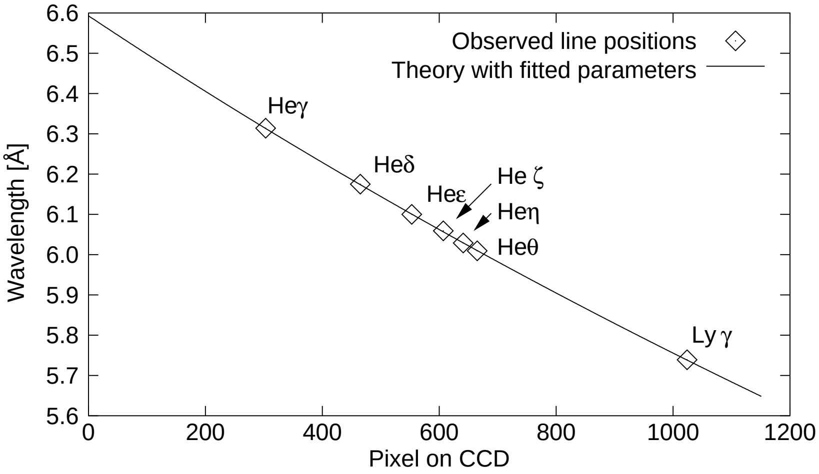

Figure 2.14. The observed line position from Fig. 2.13 and the dispersion relation with fitted parameters (Tab. 2.6) of the instrument

from the calibrated dispersion relation, which is plotted in Fig. 2.14 together with the used reference lines.

As a side effect, from the fitted distances of the spectrometer it could be observed that the detector was placed $\sim$ 12 mm off the Rowland circle (*cf.* Tab. 2.6) in the first experimental campaign, due to a misunderstanding of the distances of the CCD camera in the construction phase. This misalignment was leading to blurred images with a spatial resolution of only 887 μm on the detector and 6.7 mm in the object plane. After fixing this problem by re-constructing the connector flange between CCD camera and spectrometer vessel, the spatial resolution was limited by the resolution of the CCD array (*cf.* Fig. 2.12).

2.4 Experimental setup

The experimental setup is shown in Fig. 2.15. The experiments were carried out at the GEKKO XII laser facility at the Institute of Laser Engineering, Osaka University, in collaboration with Japanese, French, and Chinese laboratories as well as the X-ray optics group at Jena University. The wavelength of the laser was 1.053 μm in 100 ps mode. Single or double targets were used. The centers of the targets were separated by 30 mm. The targets were irradiated by two opposing laser beams with a time delay of 100 ps for quasi-traveling-wave pumping. The length of each target was 8 mm so

Line	Pixel	λ_{Ref}/Å	$\lambda_{\mathrm{Fit}}/Å$	$\Delta\lambda$/Å
Al He γ	303	6.314	6.3141	-0.0001
Al He δ	465	6.175	6.1745	$+0.0005$
Al He ε	553	6.100	6.1014	-0.0014
Al He ζ	607	6.059	6.0574	$+0.0016$
Al Ly β	614	6.053	6.0517	$+0.0013$
Al He η	641	6.0294	6.0300	-0.0006
Al He θ	665	6.0095	6.0109	-0.0014
Al Ly γ	1024	5.739	5.7389	$+0.0001$

Table 2.5. The tabulated wavelengths $\lambda_{\mathrm{Ref.}}$ of the Al H- and He-like transition from Ref. [126], the observed pixel-positions on the detector (*cf.* Fig. 2.13) and the fitted wavelengths λ_{Fit} as well as the deviation of the fitted wavelength from the reference wavelength $\Delta\lambda$. The average deviation $< \Delta\lambda >= 2.5 \times 10^{-6}$.

Parameter		Design	Fit result
Image distance	b	141.4 mm	153.5 mm
Central Bragg angle	$\theta_{B,0}$	45.0°	45.356°
Tilt of CCD array	χ	0.0°	−0.9352°
Offset on CCD array		12.96 mm	13.760 mm

Table 2.6. The output from the fit routine of the first experimental campaign with a misplaced detector. The other parameters are kept fix as of Tab. 2.4.

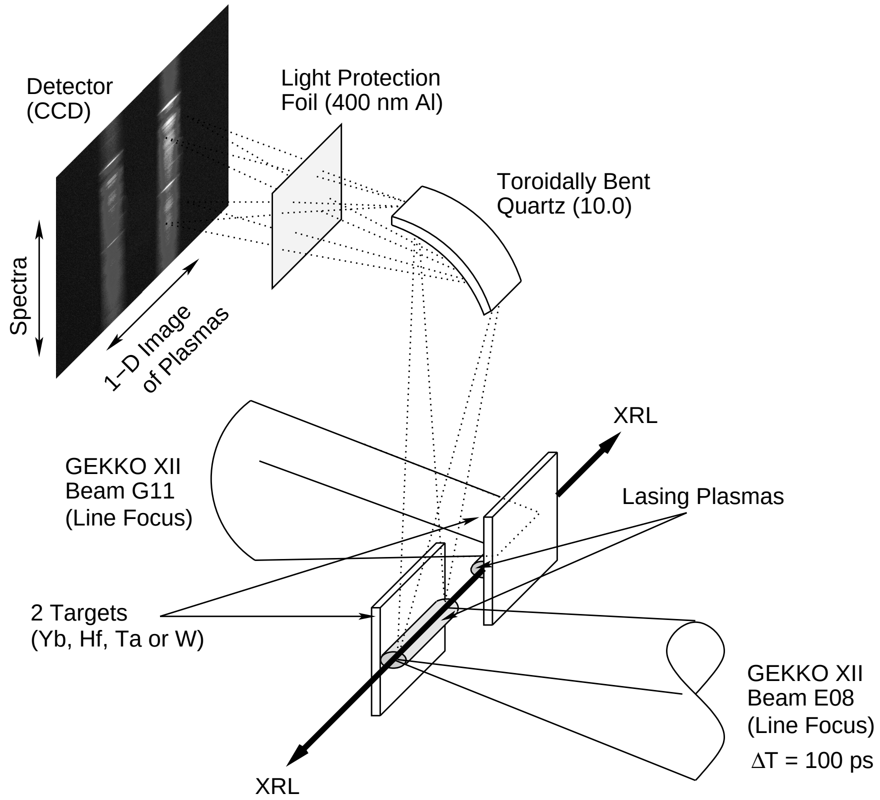

Figure 2.15. The setup of the experiment

that the total target lengths amounted to 16 mm.

The target material was Yb, Hf, Ta or W. The total pump laser energy was varied between 50 J and 360 J per target in 100 ps pulse duration. The intensity in the line-focus was varied between 2.4×10^{14} W/cm^2 and 1.7×10^{16} W/cm^2 with 0 % to 102.2 % prepulse. The time delay between prepulse and main pulse was varied between 0.6 ns and 3 ns.

A flat-field grazing-incidence spectrometer was placed on the X-ray laser axis as described in Ref. [128] in order to detect the X-ray lasing. In front of the spectrometer, 100-μm–diameter fiducial wires were placed at 0, 4.5, 8, and 10 mrad, where the on-axis line focus was defined as 0 mrad. which allowed us to determine the deflection and the beam divergence angle of the X-ray laser in the horizontal plane. No filters were placed in the spectrometer. However, the first collecting mirror in the spectrometer was covered with a thin carbon contamination; therefore the carbon K edge was clearly visible in the XRL spectra [100].

A varied-spacing 2400–lines/mm toroidal grating focused the spectrum onto a flat field perpendicular to the grating surface, covering the wavelength from 2 to 13 nm. Time integrated spectra with an angular distribution were recorded with a back-illumination-type CCD camera whose pixel size was 24 μm $\times$ 24 μm [100].

The toroidally bent crystal spectrometer was mounted at 1162 mm from the plasma at 65° subtended by the plane that included the axes of the pump lasers and the X-ray laser beam, which were on the horizontal plane. Therefore the spectrometer looked down onto a horizontally expanding plasma at 65° to its expansion direction to reduce the opacities for the resonance lines. A front-side illuminated CCD camera (Princeton Instruments, model TEA/CCD – 1242 E/3) with a pixel size of 22.5 μm was used as a detector.

2.5 Processing of the raw data

The raw experimental data were processed as follows in order to obtain the intensity in the spectral line and the line width: All steps were performed automatically according to objective criteria.

1. The structure of the background from the CCD was obtained by reading-out the CCD-array un-illuminated. This dark-image was smoothed (averaging over 3×3 pixels) and subtracted from the raw-data image.

   This subtraction gave a constant background, which was again subtracted. The amount of the uniform background was determined as the average value over a large un-illuminated area.

2. The pixel values were summed up over the spectral dispersion direction in order to obtain the spatial profile (“1D image”) of the illuminated targets.

3. Since in the first experimental campaign, the CCD array was misaligned by $\sim$ 12 mm and thus the spatial resolution decreased to $\sim$ 887 μm on the detector, the detected intensity was integrated over the spatial direction:

   For each 1D-image of the target, the maximum intensity was searched and the positions to where the intensity had decreased to 10 %.

   These 10 %-positions were used as the boundaries for the integration over the spatial direction in order to obtain the spectra.

4. The detected intensity of the spectra were corrected by the calculated throughput of the spectrometer, which depends on the wavelength of the X-rays (Fig. 2.6).

5. Since the inner photo effect was used for the detection of the X-ray photons, the detected counts (*i.e.* photo electrons) are proportional to the photon energy. Therefore, the data were corrected by dividing the count rates by the photon energy.

6. The so corrected spectra were searched for the local (*i.e.* in a certain range around the expected position) maxima which were assumed to be the wavelength of the transition under consideration. Comparisons with Gaussian fits for random samples have shown that the maximum value is in very good agreement with the center of the gauss profile.

7. On both sides of the local maximum the local absolute minima (*i.e.* the absolute minimum within a specified range around the position of the local maximum, marked by arrows in Fig. 2.16 (b)–(d)) were searched. These minima were assumed to be the background of the pseudo-continuum, which again is assumed to be linear within the range under consideration (area under the dotted line in Fig. 2.16 (b)–(d)).

8. The intensity in the spectral line (*cf.* the hatched area in Fig. 2.16 (b)–(d)) was obtained by the integral between both local minima over the peak, subtracting the background of the pseudo-continuum.

9. The width of the line was obtained as the full width at half maximum (FWHM); corrected by the linear pseudo continuum. The half-maximum value was searched from the peak towards the tales. The measured values around the half-maximum value were linear interpolated in order to find a more precise value for the FWHM.

A sample spectrum has been deconvoluted to test the broadening of the spectral line due to the instrument function. The instrument function was generated by the ray-tracing code T-RAY and the deconvolution was performed using the Fast Fourier Transform. The result was that the non-deconvoluted lines were about 5 % broader than the deconvoluted lines.

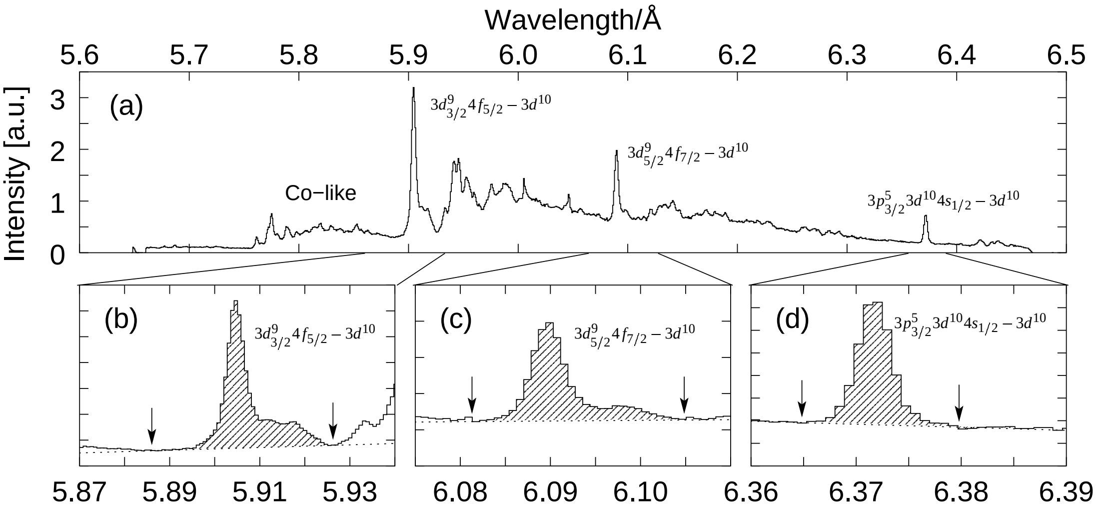

Figure 2.16. A sample spectrum from Ta. Fig. (a) shows the full recorded spectrum and (b)–(d) shows the spectral lines under consideration in detail: The dotted line marks the assumed background from the pseudo continuum, which was determined by the local minimum (arrows in (b)–(d)) and the hatched area demonstrates the integrated intensity of the transition.

Since the instrument function affects only the shape, *i.e.* the width, of the spectral line but not the integrated intensity, and the width of the line is only interesting for the calculation of the density, which can be estimated only very roughly as pointed out in Sec. 2.2.2, the detailed deconvolution for each spectrum was omitted.

2.6 Results

2.6.1 General

Figure 2.17 shows a typical processed CCD image from the spectrometer with spatial resolution along the X-Ray lasing axis of a double target Ta X-ray laser plasma, together with the corresponding profile plots integrated over both plasma columns in the spatial and spectral direction, respectively. Since the CCD was misaligned by $\sim$ 12 mm, no structure is visible in the spatial profile.

Figure 2.18 shows the Ni-like Yb, Hf, and Ta lasing lines at 5.0, 4.6, and 4.5 nm, respectively, which are close to the water window. The upper wavelength is marked by the Carbon *K*-absorption edge. The spectra in Fig. 2.18 were recorded by the flat-field grazing-incidence spectrometer in the X-ray lasing axis. The spectrum in Fig.

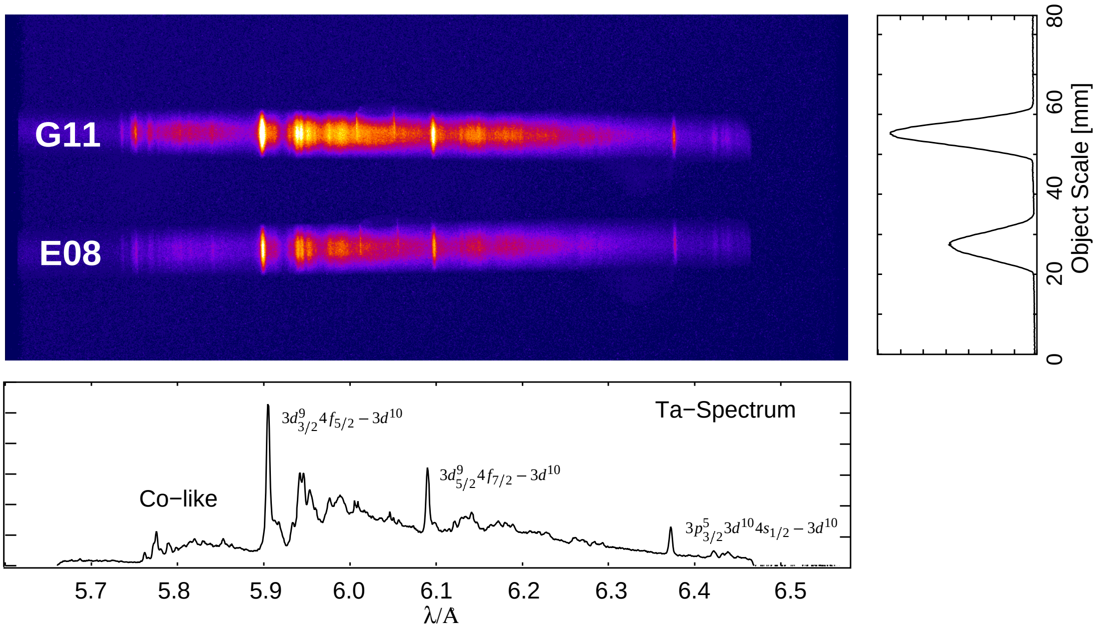

Figure 2.17. A representative CCD image of a double Ta target shot. The upper part of the picture shows the image of the target related to laser beam G11 and the lower part to beam E08.

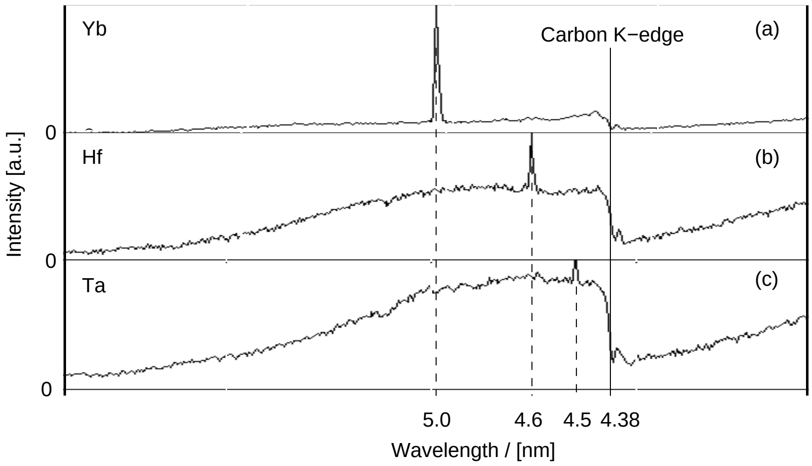

Figure 2.18. Line graphs of the X-ray laser spectra. The carbon *K* edge at 4.38 nm represents the edge of the water window. The maximum counts for the lasing lines are 8011, 3181, and 159 for Yb, Hf, and Ta, respectively [98, 100].

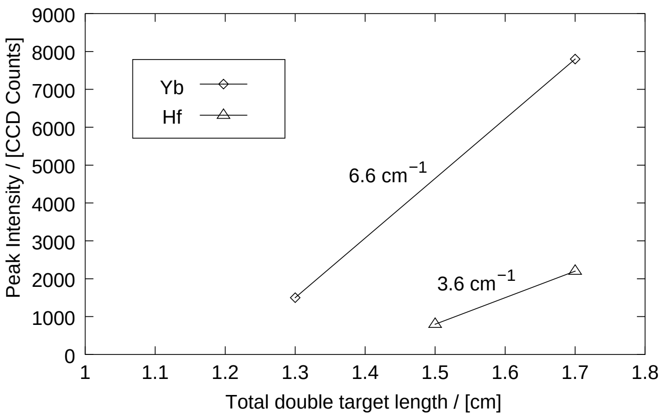

Figure 2.19. The peak X-ray laser intensity detected by the CCD as a function of the total double target length. The diamonds and the triangles represent the measured Ni-like Yb and Hf lasing intensities, respectively. The gain coefficients of the Ni-like Yb and Hf are 6.6 cm^{-1} and 3.6 cm^{-1}, respectively [98, 100].

2.18(a) shows the Ni-like Yb laser at 5.0 nm with a fairly narrow beam divergence of 1.5 mrad [98, 100]. Figure 2.18(b) shows the Hf lasing pulse at 4.6 nm with a similar divergence. Fig. 2.18(c) shows the Ni-like Ta lasing line at 4.5 nm which is at the longer wavelength edge of the water window. A relatively weak and large divergence beam has been obtained. The atomic number scaling seems to be fairly strong probable due to the 1–μm laser pumping which can not create high density and high temperature plasma as predicted by the hydrodynamic simulation [100]. Typical X-ray laser signals in the forward and the backward direction showed that the narrow-divergence and strong X-ray lasing signal was obtained in the forward direction, while the weaker and much higher divergence beam was obtained in the opposite direction [98, 100].

Figure 2.19 shows the peak intensity of the X-ray laser as a function of the length of the double target. The slab target at the right hand side acts as an oscillator and the target at the left hand side acts as an amplifier. The length of the target at the left-hand side was changed. At the forward traveling wave side, a higher intensity X-ray laser was measured than that of the opposite side. The gain coefficient of the Ni-like Yb was 6.6 cm^{-1} which corresponded to a gain length product of 11. The gain coefficient of Ni-like Hf laser was 3.6 cm^{-1} and the corresponding gain length product was approximately 6.

For the Hf laser, the gap separation of the double target, which was transverse to the on-axis of the X-ray laser, was changed. An intense soft X-ray laser with narrow divergence was obtained around the optimum separation of 150 μm.

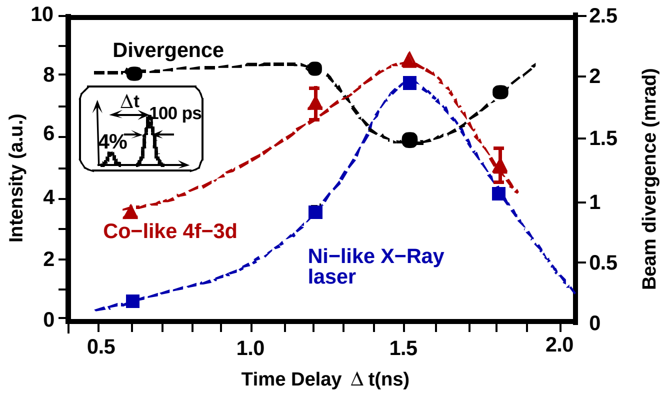

Figure 2.20. Intensities of the Yb X-ray laser and the Co-like Yb $af-3d$ transition and the X-ray laser beam divergence as a function of the prepulse to main pulse time delay [98, 100].

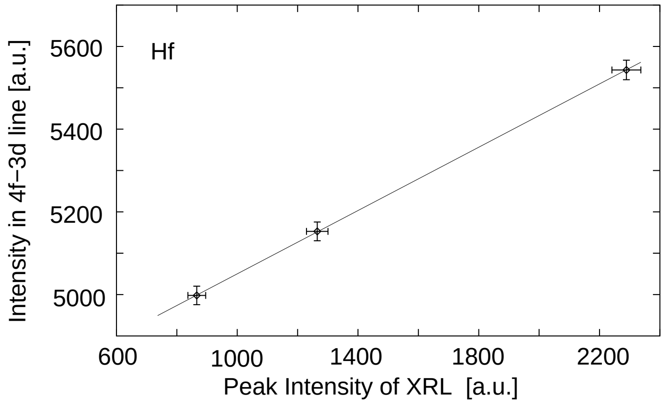

Figure 2.21. Correlation between the $4f-3d$ emission line intensity and the $4d-4p$ -XRL emission intensity observed in Hafnium.

2.6.2 Comparison of the $4d \rightarrow 4p$ and $4f \rightarrow 3d$ transition

Figure 2.20 shows the intensity of the Yb X-ray laser, its beam divergence and the intensity of the strongest Co-like line as a function of the time interval between the prepulse and the main pulse. The strong dependency of the X-ray laser intensity on the time delay can be seen. The optimum time delay was approximately 1.5 ns, corresponding to the maximum Co-like abundance, where the X-ray laser intensity maximized and the minimum beam divergence was realized.

Figure 2.21 shows the correlation of the detected Ni-like $4f-3d$ transition to the Hf X-ray laser signal. Only data with obtained lasing are considered. Thus, several parameters are changed in the here presented data. However, the correlation between both signals is linear in the presented data set. This is astonishing, since the $4f-3d$ intensity depends only on the population of the ionization state while the XRL intensity depends also on parameters like the alignment of the targets, the length of the target, etc. which do not affect the ionization and thus the $4f-3d$ intensity.

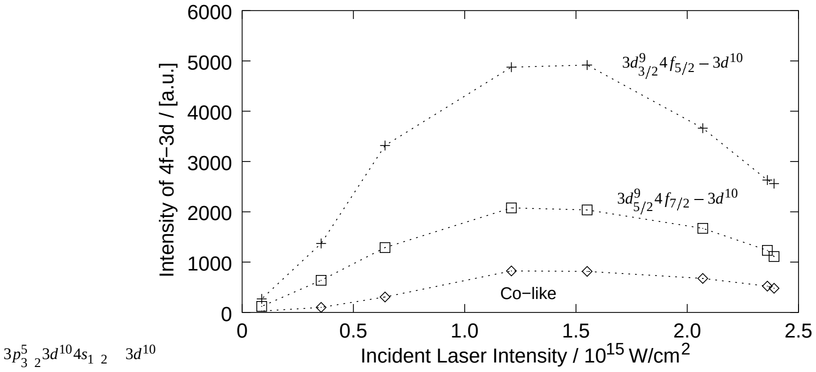

Figure 2.22. The optimal pump laser intensity of the Ta plasma in dependency of the incident laser intensity. The maximum emission of the Ni-like and Co-like lines appeared at about 1.3×10^{15} W/cm^2

2.6.3 Studies on tantalum plasmas (point focus)

Parallel to the aim of observing amplified emission towards the water window, a series of point focus experiments were carried out in order to study the influence of the parameters of the incident laser beam on the plasma parameters. The experiments were carried out immediately after the main X-ray laser experiment by using the remaining laser beams. Despite the reduced set of parameters, it is possible to find the optimal plasma conditions, before optimizing the set-up of the X-ray laser experiment, *i.e.* finding the best radius of curvature of the slab target, the best gap between the double targets, etc.

The target material was mainly Ta. The total pump laser energy was varied between 50 J and 180 J in 100 ps mode while the focal spot was varied between 1.36×10^{-5} cm^2 and 7.85×10^{-3} cm^2. The so varied resulting incident laser intensity was between 8.8×10^{13} W/cm^2 and 3.5×10^{16} W/cm^2.

Figure 2.22 shows the intensity of the Ni-like $4f - 3d$ emission lines as well as the strongest Co-like line as a function of the incident laser intensity at 4 % prepulse. The maximum emission was found for all three lines at about 1.3×10^{15} W/cm^2. For lower intensities, the incident laser is not sufficient to produce this ionization state while at higher laser intensities, the plasma is much higher ionized. Thus, one can conclude that at 1.3×10^{15} W/cm^2 the amount of $4p$ ions, the upper level of the lasing transition, reaches its maximum, too. However, such high intensities could not be achieved in the line-focus X-ray laser plasmas, which was only about 3×10^{14} W/cm^2, *i.e.* about a factor four lower.

Figure 2.23 shows two Ta spectra taken at 1.2×10^{15} W/cm^2 incident laser intensity, *i.e.* around the optimum intensity, but different amount of prepulse. Figure 2.23(a) was taken without prepulse and (b) was taken with 4 % prepulse 3 ns in advance of the

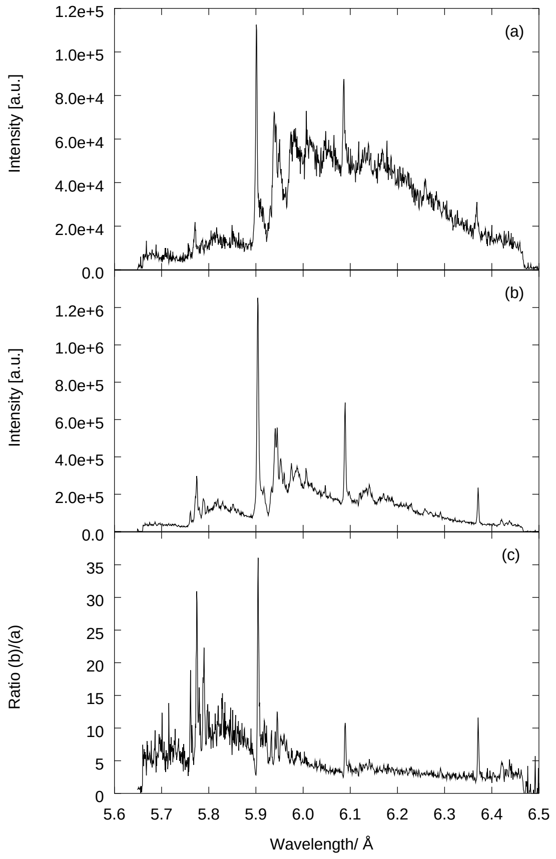

Figure 2.23. The Ta spectrum without prepulse (a), with 4% prepulse (b) and the ratio with prepulse to without prepulse (c). In the Ni-like emission lines, an up to 35× higher intensity could be observed in spectrum taken with prepulse compared to the spectrum without prepulse, while the pseudo-continuum is only enlarged by a factor four. (Note the different scale of the ordinates).

main pulse. Figure 2.23(c) shows the ratio of both spectra. With prepulse, the $4f-3d$ line is about 35 times more intense than without prepulse, indicating that there are about 35 times more $4f$ ions and, in conclusion, $4p$ ions in the plasma.

An interesting fact is that there is an almost constant factor of about four between the quasi-continuum of both spectra above $\sim$ 6.0 Å, while the emission in the spectral lines increases and the (Co-like) quasi-continuum of the spectrum taken with prepulse is over-proportionally enhanced below 6.0 Å.

Figure 2.24 shows the calculated temperatures of the plasma as a function of the incident laser intensity. The target was Ta foil and the laser focus was kept to 333 μm in diameter which correspond to 8.7×10^{-4} cm^2 illuminated area on the target, while the energy in the pulse was varied between between 31 J and 180 J, so that all shots are taken at the same plasma size. This is important since otherwise, different cooling effects will influence the result. The prepulse amounts to 4 % of the main pulse and came 3 ns in advance. The duration of each pulse was 100 ps.

The temperature of the plasma was obtained by Eq. (2.9). The different plots in Fig.

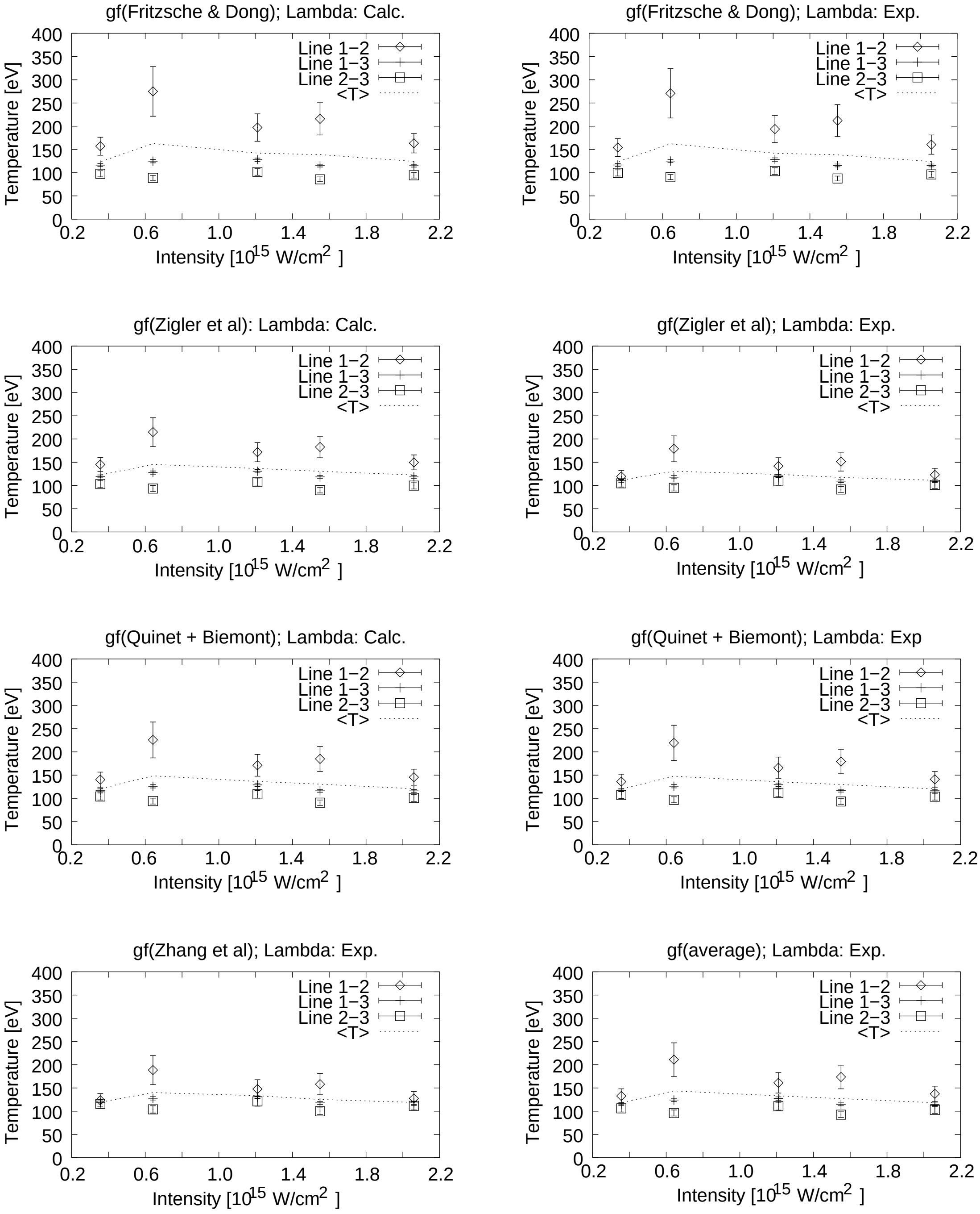

Figure 2.24. The temperatures of the Ta plasmas for different incident laser intensities and different calculation of the gf-factor while keeping the experimental conditions constant, except the pulse energy. The labels 'Line *i*–*j* stands for the calculation of the temperature by comparing 'Line *i*' with 'Line *j*', where 'Line 1' stands for $3d^9_{3/2}4f_{5/2} - 3d^{10}$, 'Line 2' for $3d^9_{5/2}4f_{7/2} - 3d^{10}$ and 'Line 3' for $3p^5_{3/2}3d^{10}4s_{1/2} - 3d^{10}$. The dotted line marks the average value of the comparison of the three lines.

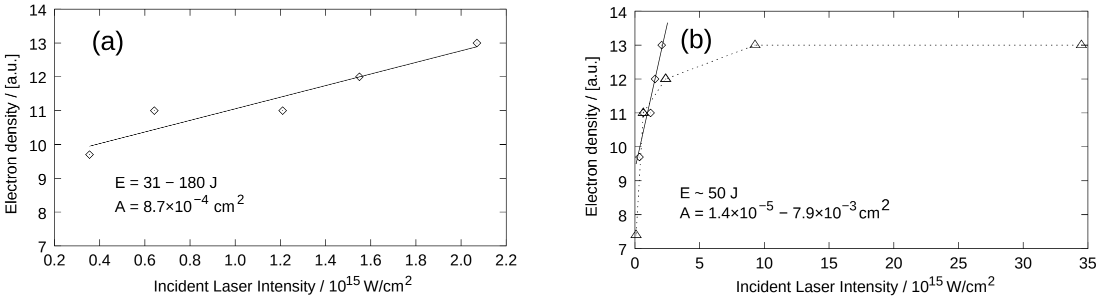

Figure 2.25. The density of the Ta plasma in dependency of the incident laser intensity obtained from the temporal and spatial integrated spectra: (a) intensity varied by changing the energy in the pulse (◇) together with the linear fit (—) and (b) intensity varied by changing the focal spot (△). For comparison, the data of (a) are plotted in (b), too.

2.24 are due to different calculations of the gf-factors (*cf.* Tab. 2.1) as well as the use of the calculated and experimental wavelengths (*cf.* Tab. 2.2). From Fig. 2.24 one sees that the average temperature is almost constant about 120 eV even though the incident laser intensity was varied by about a factor of ten. While the obtained temperatures of the comparison of the three lines is in good agreement for the gf–factors by Zhang *et al.* [109] and Zigler *et al.* [110] in conjunction with the experimental wavelengths, the gf–factors from Fritzsche *et al.* [107] and Quinet *et al.* [108] give large differences between the three comparisons. A detailed discussion of the temperature is given in Sec. 2.7.

Figure 2.25 shows the calculated electron density of the plasma as a function of the incident laser intensity. The unit of the density in Fig. 2.25 is arbitrary, since for ionized gases, the detailed calculation of the density is extremely complicated, have been done in detail only for a few atoms [25], and is far beyond the frame of this work. However, full calculation give a proportional relation to the width of the spectral line (*cf.* Eq. (2.21) and Ref. [25, p 220]). Thus, the data shown in Fig. 2.25 represent the behavior of the density.

Figure 2.25(a) shows the electron density for a constant focal spot size but varied pulse energy. The relation between the electron density and the incident laser intensity appears to be linear in the observed range. In Fig. 2.25(b) the incident laser intensity was varied by keeping the energy in the pulse constant at about 50 J but changing the spot size of the laser beam. Here, the density is increasing very steeply at the beginning but goes then in saturation. The data from Fig. 2.25(a) are plotted in Fig. 2.25(b), too, for a direct comparison of both cases.

Using the high resolution character of the instrument, the positions of the emission lines were measured, too. The data are summarized in Table 2.2 together with the theoretical values from the literature and the calculated wavelengths by S. Fritzsche and Dong which were kindly done to support this work [107]. The calculation of the wavelengths were done using the unpublished prototype version of the GRASP92 code, which is named GRASP2 [129, 130]. The uncertainty in the last digit (standard error) of the experimental values is given in braces in Tab. 2.2. The average error (standard deviation) is $\Delta\lambda/\lambda = 9.4 \times 10^{-5}$, $\Delta\lambda/\lambda = 6.6 \times 10^{-5}$, and $\Delta\lambda/\lambda = 5.9 \times 10^{-4}$ for Hf, Ta, and W, respectively. The higher error in the W values is due to the small data base of only three shots.

Depending on the calculation and the transition line, the agreement between the calculation and the experiment is excellent to fair. On the other hand, the measured wavelengths are compared to the transition energies of the Al H- and He-like ions. The resulting error in the dispersion relation is calculated as 2.6×10^{-6} Å(*cf.* Tab. 2.5).

2.7 Discussion of the temperature

The here applied way of calculating the temperature is highly sensitive to errors in the parameters. This is due to the fact that the temperature is inverse proportional to the logarithm of all parameters (*cf.* Eq. (2.9)). At high temperatures, the dependency of the temperatures on the parameters becomes very steep so that small changes in the parameters causes large changes in the calculated temperature.

The error bars in the temperature plots were estimated by the following set of equations:

$$\frac{\partial(k_B T)}{\partial E_{10}} = -\frac{\ln\left(\frac{gf_{10}E_{10}^2 I_{20}}{gf_{20}E_{20}^2 I_{10}}\right) E_{10} + 2E_{20} - 2E_{10}}{\ln\left(\frac{gf_{10}E_{10}^2 I_{20}}{gf_{20}E_{20}^2 I_{10}}\right)^2 E_{10}} \tag{2.32a}$$

$$\frac{\partial(k_B T)}{\partial E_{20}} = \frac{\ln\left(\frac{gf_{10}E_{10}^2 I_{20}}{gf_{20}E_{20}^2 I_{10}}\right) E_{10} + 2E_{20} - 2E_{10}}{\ln\left(\frac{gf_{10}E_{10}^2 I_{20}}{gf_{20}E_{20}^2 I_{10}}\right)^2 E_{20}} \tag{2.32b}$$

$$\frac{\partial(k_B T)}{\partial gf_{10}} = -\frac{E_{20} - E_{10}}{\ln\left(\frac{gf_{10}E_{10}^2 I_{20}}{gf_{20}E_{20}^2 I_{10}}\right)^2 gf_{10}} \tag{2.32c}$$

$$\frac{\partial(k_B T)}{\partial g f_{20}} = \frac{E_{20}-E_{10}}{\ln\left(\frac{g f_{10} E_{10}^2 I_{20}}{g f_{20} E_{20}^2 I_{10}}\right)^2 g f_{20}} \tag{2.32d}$$

$$\frac{\partial(k_B T)}{\partial I_{10}} = \frac{E_{20}-E_{10}}{\ln\left(\frac{g f_{10} E_{10}^2 I_{20}}{g f_{20} E_{20}^2 I_{10}}\right)^2 I_{10}} \tag{2.32e}$$

$$\frac{\partial(k_B T)}{\partial I_{20}} = -\frac{E_{20}-E_{10}}{\ln\left(\frac{g f_{10} E_{10}^2 I_{20}}{g f_{20} E_{20}^2 I_{10}}\right)^2 I_{20}} \tag{2.32f}$$

For the calculation, an uncertainty of 0.8 mÅ in the transition wavelength, ± 0.1 in the gf-factor and 5 % error in the intensity was assumed.

Another influence in the error might be the optical thickness, *i.e.* the self-absorption of the emitted intensity in the plasma. This optical thickness depends beside the wavelength and the size of the plasma on the electron density, and might be different for the three different emission lines, as pointed out in Sec. 2.2.2. Due to this change in the self absorption, the emitted spectrum might not represent the Boltzmann-distribution, as it was applied, but has to be corrected by the appropriate expression for the optical thickness, which might change the intensity ratio of the emission lines and will therefore lead to a wrong temperature. Even though there are formulae for simple estimates for the opacity for blackbody radiation [111, 112], these equations are of limited use here since they are independent of the wavelength. *I.e.* the obained opacity cannot describe a variation of the ratio of the intensities as a function of the wavelength. A detailed calculation however is extremely difficult and cannot be found in public for $Z > 30$ [113,131]. However, it is important to be aware that the observed emission line ration depends on both, the electron temperature and density. This altered line ratio of the emission lines could explain that the temperature is with $\sim$ 150 eV about a factor ten smaller than expected from Fig. 2.2.

Also, from Fig. 2.24 one sees that the average temperature is almost constant even though the incident laser intensity was varied by about a factor of ten. This is astonishing (or wrong) since one expects a much higher temperature for a much higher intensity.

One reason for the constant temperature might be the time integrated measurement of the temperature. To check this possibility, in another experimental campaign, carried out in May 2000, the spectra should be recorded time resolved using a streak camera. However, due to technical problems with the laser system and the streak camera, no data could be obtained within the available beam time.

The simulation using the one-dimensional MEDUSA code [132] shows, that the arithmetic mean temperature varies almost linear between 219 keV and 589 keV for $I_{\text{inc}} = 2 \times 10^{14}$ W/cm^2 and $I_{\text{inc}} = 2 \times 10^{15}$ W/cm^2, respectively. At the time of the main pulse, the temperature raises briefly to 3.5 keV and 10 keV for $I_{\text{inc}} = 2 \times 10^{14}$ W/cm^2 and $I_{\text{inc}} = 2 \times 10^{15}$ W/cm^2, respectively.

Of course, this arithmetic mean value does not represent the averaging of the spectrometer, but gives an idea of the variation of the temperature. For a correct simulation of the averaging of the spectrometer, the absolute number of emitted photons in the resonances have to be calculated for every temperature, time and spatial distance. The generated photons have to be summed up and then compared with each other. However, a simulation code for the spectra for such heavy materials as Ta could not be found in public.

In comparison with other works, Nantel *et al.* [105] measured for the same pump laser wavelength but Ne-like ^{30}Zn at $(1-2) \times 10^{13}$ W/cm^2 in 800 ps a constant temperature of 335 ± 25 eV, which appeared to be independent from the amount of the prepulse. For comparison, the MEDUSA code was run with the values from Ref. [105], where the arithmetic mean value for the temperature is 375 eV for 2×10^{13} W/cm^2.

Another interesting question arises from the large difference in the used gf-values in the literature, which give very different agreements of the three calculated values from one spectrum (Fig. 2.24). While temperatures obtained from the gf-factors provided by Zhang *et al.* [109] are in good consistence, the temperatures obtained from the gf–factors calculated by Fritzsche *et al.* [107] differ by a factor of two. Therefore, it would be interesting to measure the gf-factors from the experimental data set.

The idea for basic approach for the measurement of the gf-factors was to use Equation (2.9) for three different shots $j = 1, 2, 3$, *i.e.* three different temperatures, taken under the same experimental conditions except the varied incident laser intensity. The energies E_i and intensities $I_i^{(j)}$ are taken from the spectra:

$$T_1 = T_1(gf_{10}, gf_{20}, I_1^{(1)}, I_2^{(1)}, E_1, E_2)\Big|_{\text{Shot 1}} \tag{2.33a}$$

$$T_1 = T_1(gf_{10}, gf_{30}, I_1^{(1)}, I_3^{(1)}, E_1, E_3)\Big|_{\text{Shot 1}} \tag{2.33b}$$

$$T_2 = T_2(gf_{10}, gf_{20}, I_1^{(2)}, I_2^{(2)}, E_1, E_2)\Big|_{\text{Shot 2}} \tag{2.33c}$$

$$T_2 = T_2(gf_{10}, gf_{30}, I_1^{(2)}, I_3^{(2)}, E_1, E_3)\Big|_{\text{Shot 2}} \tag{2.33d}$$

$$T_3 = T_3(gf_{10}, gf_{20}, I_1^{(3)}, I_2^{(3)}, E_1, E_2)\Big|_{\text{Shot 3}} \tag{2.33e}$$

$$T_3 = T_3(gf_{10}, gf_{30}, I_1^{(3)}, I_3^{(3)}, E_1, E_3)\Big|_{\text{Shot 3}} \tag{2.33f}$$

i.e. six equations with six unknown parameters (T_1, T_2, T_3, gf_{10}, gf_{20}, gf_{30}). Setting equal the two equations for the same temperature this system of equation reduces to three equations with the three unknown parameters gf_{10}, gf_{20}, and gf_{30}:

$$T_1(gf_{10}, gf_{20}, I_1^{(1)}, I_2^{(1)}, E_1, E_2) = T_1(gf_{10}, gf_{30}, I_1^{(1)}, I_3^{(1)}, E_1, E_3) \tag{2.34a}$$

$$T_2(gf_{10}, gf_{20}, I_1^{(2)}, I_2^{(2)}, E_1, E_2) = T_2(gf_{10}, gf_{30}, I_1^{(2)}, I_3^{(2)}, E_1, E_3) \tag{2.34b}$$

$$T_3(gf_{10}, gf_{20}, I_1^{(3)}, I_2^{(3)}, E_1, E_2) = T_3(gf_{10}, gf_{30}, I_1^{(3)}, I_3^{(3)}, E_1, E_3) \tag{2.34c}$$

However, when trying to isolate the expressions for the gf–factors, one finds, that this system of equations has no solution.

Summary and Outlook

In the present work, the conception, design and appliance of toroidally bent crystals for the X-ray optical diagnostics of laser produced plasmas is discussed.

The first part of this work deals with the development, design and characterization of an X-Ray microscope for the observation of Rayleigh-Taylor instabilities, which act against the confinement and ignition of the fuel in the inertial confinement fusion (ICF) process.

The aim of this work was the development and test of an X-ray microscope which satisfies the high demands on this kind of experiment, *i.e.* two-dimensional monochromatic imaging with high luminosity, high resolution ($\lesssim 3\ \mu$m) as well as 400 μm focal depth. The microscope should be applied in the frame of the HIPER research program at the Institute of Laser Engineering (ILE) at Osaka University/Japan.

The basis of the X-ray microscope is a toroidally bent quartz crystal of 7×7 mm^2 which should be operated at 30× magnification and later 70× magnification.

The simulation of the constructed microscope by ray-tracing calculations shows that the required specifications cannot only be fulfilled but even exceeded: The simulation gives an expected resolution of less than $< 1\ \mu$m at a crystal aperture of 3.5 mm and 30× magnification.

However, the experimental evidence could not be demonstrated due to technical problems and limited beam time at GEKKO XII. The highest demonstrated resolution in this work was 6 μm.

Being aware of the very limited beam time at ILE and the great interest in the demonstration of the sub-micrometer resolution, another demonstration experiment is proposed in detail, which can be carried out in a small laboratory using an X-ray generator.

First data could be obtained from the Rayleigh-Taylor instability experiment and are discussed qulitatively. For a detailed analysis, however, the obtained data set is too small and the signal too weak to be clearly distinguished from the noise of the streak- or CCD-camera due to focal problems with the probe laser.

Since on the one hand, the investigation of the Rayleigh-Taylor instabilities are of greatest importance in the nuclear fusion research and on the other hand, the here developed microscope is the main diagnostic for this kind of experiment, the work started here will be continued in the future beyond the frame of this work.

The aim of the second part of the present work was the diagnostic of the lasing medium for amplified spontaneous emission (ASE) close to the water window. For this purpose, an one-dimensionally (1–D) imaging X-ray spectrometer based on toroidally bent quartz crystals was developed for the observation of the Ni-like $4f-3d$ transition of Yb, Hf, Ta, and W ions, which should be related to the amplified $4d-4p$ emission, since the $4f$ niveau is very close to the $4d$ niveau. Thus, the $4f-3d$ transition can serve as an indicator for the population of the $4d$ niveau.

The spectrometer was designed for the recording of the spectra either 1–D spatially resolved but time-integrated by using a CCD camera, or time-resolved but spatially integrated by using a streak camera.

The characteristics of the spectrometer are discussed in detail for the used range of operation, *i.e.* 5.7–6.4 Å, by using ray-tracing calculations. It was found that the spectral resolution of the spectrometer is almost independent of the source size and the deviation of the source from the diffraction plane. Even for 20 mm large plasma columns as they are used for X-Ray laser experiments and shifts of the source of 30 mm off the diffraction plane, a spectral resolution of better than 3×10^{-3} can be obtained. Also the spatial resolution is almost independent of the source size and limited in the present case by the resolution of the CCD array, which could be demonstrated in the experiment. However, the ray-tracing calculation shows that the spatial resolution decreases the smaller the sagittal aperture of the crystal is. This is due to the decreased peak intensity and increased imaging errors relative to the peak reflectivity.

The spectrometer was calibrated *in-situ* by comparing the observed line positions of the well-known Al plasma with tabulated values. From the comparison, the actual distances of the set-up can be obtained, which define the dispersion relation completely. When using a calibrated CCD camera, too, the absolute number of emitted photons from the plasma can be obtained.

The experiments were carried out at the GEKKO XII Nd:glas-laser-system at the Institute of Laser Engineering at the University of Osaka/Japan in a Japanese, Chinese, French, and German collaboration. The experiment confirms the expected relation between the Ni-like $4f - 3d$ transition and the amplified $4d - 4p$ transition. For Ta, the optimal pump-laser intensity was found at $\sim 1.5 \times 10^{15}$ W/cm^2, a pre-pulse of 4 % increases the population of the $4f$ niveau by a factor of up to $35\times$. The estimation of the temperature from the time-integrated spectra by using the ordinary Boltzmann-distribution gives an electron temperature of ~ 150 eV which was observed as independent of the incident pump-laser intensity. One reason for this independence might be the averaging by time integration. Thus, the time resolved observation of the spectra is necessary in order to get some evidence of this result, what could not be done yet in the available beam time.

The analysis of the electron density of the plasma shows a linear relation between the intensity of the pump laser and the electron density when keeping the focal spot constant. Also, the transition wavelength of the $4f - 3d$ lines could be measured. The agreement with theoretical values from the literature is at a difference of $\pm(< 1 \ldots 10)$ mÅ, depending on the author and the spectral line, excellent to good.

For the next experimental campaign, the time-resolved observation of the $4f - 3d$ transition is planned, which should give answers to such important questions as: What is the influence of the pulse train on the ionization? At which time of pulse train is the maximum ionization reached? At which time is reached the maximum electron temperature and -density?

Bibliography

[1] G. M. Weyl, “Physics of laser-induced breakdown: An update,” in *Laser-Induced Plasmas and Applications*, L. J. Radziemski and D. A. Cremers, eds., ch. 1, pp. 1–67, Marcel Dekker, Inc., New York, 1989.

[2] L. A. Artsimowitsch and R. S. Sagdejew, *Plasmaphysik für Physiker*, B. G. Teubner, Stuttgart, 1983.

[3] J. H. Nuckolls, L. Wood, A. Thiessen, and G. B. Zimmerman, “Laser compression of matter to super-high densities: thermonuclear (CTR) applications,” *Nature* **239**, pp. 139–142, 1972.

[4] J. J. Duderstadt and G. A. Moses, *Inertial Confinement Fusion*, John Wiley & Sons, Inc., 1982.

[5] C. Yamanaka, *Introduction to Laser Fusion*, vol. 10 of *Laser Science and Technology*, Harwood Academic Publishers, Chur, Switzerland, 1990.

[6] J. Lindl, “Development of the indirect-drive approach to intertial confinement fusion and the target physics basis for ignition and gain,” *Phys. Plasmas* **2**, pp. 3933–4024, 1995.

[7] J. D. Lindl, *Inertial Confinement Fusion: the quest for ignition and energy gain using indirect drive*, Springer-Verlag, 1998.

[8] M. B. Hooper, ed., *Laser Plasma Interactions 5: Interial Confinement Fusion*, Institute of Physics Publishing, 1994.

[9] H. Takabe, “Laboratory astrophysics with intense and ultra-intense lasers,” in *Superstrong Fields in Plasmas*, M. Lontano *et al.*, eds., p. 560, The American Institute of Physics, 1998.

[10] B. A. Remington, D. Arnett, R. P. Drake, and H. Takabe, “Modeling astrophysical phenomena in the laboratory with intense lasers,” *Science* **284**, pp. 1488–1493, 1999.

[11] Y.-G. Kang, H. Nishimura, H. Takabe, H. Azechi, T. Norimatsu, M. Nakai, H. Nagatomo, A. Sunahara, K. Fujita, M. Nakatsuka, K. Mima, H. G. Kim, and K. H. J., “Hydrodynamic model experiment of the collision of supernova 1987A with its circumstellar ring using high power laser,” in *High Power Lasers in Energy Engineering*, K. Mima, G. L. Kulcinski, and W. Hogan, eds., *SPIE Proceedings* **3886**, pp. 489–494, (San Diego, CA), 2000.

[12] S. Atzeni, “Selected topics in ICF target design.” Lecture notes, held at ILE, Jul. 1994.

[13] D. L. Matthews, P. L. Hagelstein, M. D. Rosen, M. J. Eckart, N. M. Ceglio, A. U. Hazi, H. Medecki, B. MacGowan, J. E. Trebes, B. L. Whitten, E. M. Campbell, C. W. Hatcher, A. M. Hawryluk, R. L. Kauffman, L. D. Pleasance, G. Rambach, J. H. Scofield, G. Stone, and T. A. Weave, “Demonstration of soft X-ray amplifier,” *Phys. Rev. Lett.* **54**, pp. 110–113, 1985.

[14] B. MacGowan, S. Maxon, P. L. Hagelstein, C. J. Kean, R. A. London, D. L. Matthews, M. D. Rosen, J. H. Scofield, and D. A. Whelan, “Demonstration of soft X-ray amplifier in Ni-like ions,” *Phys. Rev. Lett.* **59**, pp. 2157–2160, 1987.

[15] B. MacGowan, S. Maxon, L. B. DaSilva, D. J. Fields, C. J. Keane, D. L. Matthews, L. Osterheld, J. H. Scofield, G. Shimkaveg, and G. F. Stone, “Demonstration of x-ray amplifiers near the carbon *K*–edge,” *Phys. Rev. Lett.* **65**, pp. 420–423, 1990.

[16] H. Daido, S. Ninomiya, T. Imani, Y. Okaichi, M. Takagi, R. Kodama, H. Takabe, Y. Kato, F. Koike, J. Nilsen, and K. Murai, “Atomic number scaling of the Ni-like soft x-ray lasers,” *Int. Journ. Mod. Phys. B* **11**, pp. 945–990, 1997.

[17] *Proceedings of the 6th International Conference on X-Ray Lasers*, vol. 159 of *Conference Series*, (Bristol/UK), Institute of Physics, 1999.

[18] R. Kauffmann, “X-ray radiation from laser plasma,” in *Physics of Laser Plasma*, A. M. Rubeninchik and S. Witkowski, eds., vol. 3 of *Handbook of Plasma Physics*, ch. 3, pp. 111–162, North-Holland, 1991.

[19] W. Goldstein, C. Hooper, J. Gauthier, J. Seely, and R. Lee, eds., *Radiative Properties of Hot Dense Matter*, World Scientific, 1991.

[20] U. Teubner *et al. Phys. Rev. E* **54**, pp. 4767–4177, 1996.

[21] T. Feurer *et al. Phys. Rev. E* **56**, pp. 4608–4614, 1996.

[22] T. Missalla, I. Uschmann, E. Förster, G. Jenke, and D. von der Linde, “Monochromatic focussing of subpicosecond x-ray pulses in the keV range,” *Rev. Sci. Instrum.* **70**, pp. 1288–1299, 1999.

[23] V. Weisskopf and E. Wigner, “Berechnung der natürlichen Linienbreite auf Grund der Diracschen Lichttheorie,” *Z. Phys.* , pp. 54–73, 1930.

[24] V. Weisskopf, “Die Breite der Spektrallinien in Gasen,” *Phys. Z.* **34**, pp. 1–24, 1933.

[25] I. H. Hutchinson, *Principles of Plasma Diagnostics*, Cambridge University Press, 1987.

[26] H. R. Griem, *Principles of Plasma Spectroscopy*, Cambridge University Press, 1997.

[27] M. Dirksmöller, O. Rancu, I. Uschmann, P. Renaudin, C. Chenais-Popvics, G. J. C., and E. Förster, “Time resolved x-ray monochromatic imaging of a laser-produced plasma at 0.6635 nm wavelength,” *Optics Communications* **118**, pp. 379–387, 1995.

[28] I. Uschmann, E. Förster, H. Nishimura, K. Fujita, Y. Kato, and S. Nakai, “Temperature mapping of compressed fusion pellets obtained by monochromatic imaging,” *Rev. Sci. Instr.* **66**, pp. 734–736, 1996.

[29] M. Vollbrecht, I. Uschmann, E. Förster, K. Fujita, Y. Ochi, H. Nishimura, and K. Mima, “Five channel x-ray imaging of laser fusion plasmas,” *J. Quant. Spectrosc. Radiat. Transfer* **58**, pp. 965–974, 1997.

[30] I. Golovkin, R. Mancini, Y. Ochi, K. Fujita, H. Nishimura, H. Shiraga, N. Miyanaga, H. Azechi, R. Butzbach, I. Uschmann, E. Förster, J. Delettrez, J. Koch, R. W. Lee, and L. Klein, “Determination of dynamic gradients in high energy density plasmas,” *Phys. Rev. Lett.* . to be submitted.

[31] I. Uschmann, K. Fujita, I. Niki, R. Butzbach, H. Nishimura, J. Funakura, M. Nakai, E. Förster, and K. Mima, "Ten channel time resolved monochromatic imaging of inertial confinement fusion plasmas," *Applied Optics* , 2000. in print.

[32] J. Koch, O. Landen, T. Barbee, Jr., P. Celliers, L. Da Sivla, S. Glendinning, B. Hammel, D. Kalantar, C. Brown, J. Seeley, G. Bennett, and W. Hsing, "High-energy x-ray microscopy techniques for laser-fusion plasma research at the National Ignation Facility," *Applied Optics* **37**, pp. 1784–1795, 1998.

[33] Y. Aglitskiy, T. Lehecka, O. S., B. S., C. Pawley, K. Gerber, J. Sethian, B. C. M., J. Seely, U. Feldmann, and G. Holland, "High resolution monochromatic x-ray imaging system based on spherically bent crystals," in *Technical Programme and Book of Abstracts of the XXV Eclim*, (Formia/Italy), May 1998.

[34] E. Förster, R. Butzbach, P. Gibbon, I. Uschmann, H. Daido, K. Fujita, and H. Nishimura, "Diagnostics and applications of laser produced plasmas," in *High-Power Lasers in Energy Engineering*, K. Mima, G. L. Kulcinski, and W. Hogan, eds., vol. 3886, pp. 342–352, SPIE, 2000.

[35] F. J. Marshall and G. R. Bennett, "A high-energy x-ray microscope for inertial confinement fusion," *Rev. Sci. Instrum.* **70**, pp. 617–619, 1999.

[36] P. Kirkpatrick and A. V. Baez, "Formation of optical images by x-rays," *J. Opt. Soc. Am.* **38**, pp. 766–774, 1948.

[37] R. Kodama, H. Shiraga, M. Miyanaga, T. Matsushita, M. Nakai, H. Azechi, K. Mima, and Y. Kato, "Study of laser-imploded core plasmas with an advanced kirkpatrick-baez x-ray microscope," *Rev. Sci. Instrum.* **68**, pp. 824–827, 1997.

[38] J. H. Underwood, J. T. W. Barbee, and C. Frieber *Appl. Opt.* **25**, p. 1730, 1986.

[39] W. B. Peatman, *Gratings, Mirrors and Slits*, ch. 5.5, pp. 139–144. Gorden and Breach Science Publishers, 1997.

[40] Z. Chang, A. Rundquist, J. Zhou, M. M. Murnane, H. C. Kapteyn, X. Lui, B. Shan, X. Lui, L. Nui, M. Gong, and X. Zhang, "Demonstartion of a sub-picosecond x-ray streak camera," *Appl. Phys. Lett.* **69**, pp. 133–135, 1996.

[41] D. K. Bradley, P. M. Bell, J. D. Kilkenny, R. Hanks, O. Landen, P. A. Jaanimagi, P. W. McKenty, and C. P. Verdon, "High-speed gated x-ray imaging for icf target experiments," *Rev. Sci. Instrum.* **63**, pp. 4813–4817, 1992.

[42] U. Schumacher, "Fusionsforschung," 1993.

[43] R. Scherm and B. Fåk, "Neutrons," in *Theory, Instruments and Methods*, J. Baruchel, J.-L. Hodeau, M. S. Lehmann, J.-R. Regnard, and C. Schlenker, eds., vol. I of *Neutron and Synchrotron Radiation for Condensed Matter Studies*, ch. V, pp. 113–143, Springer-Verlag & Les Editions de Physique, 1993.

[44] E. Teller, "ithe work of many people," *Science* **121**, pp. 267–275, 1955.

[45] R. W. Hardin, "World's largest laser shoots photonics to a new level," *Photonics Spectra* **5/98**, pp. 104–114, 1998.

[46] Y. Ochi, M. Fukao, A. Sunahara, H. Nishimura, K. Fujita, T. Kawamura, H. Shiraga, N. Miyanaga, H. Azechi, H. Takabe, K. Mima, T. Yamanaka, S. Nakai, R. Butzbach, I. Uschmann, and E. Förster, "X-ray spectroscopic analysis of the influence of the low-modal non-uniformity on the formation of the hot spark," in *High-Power Lasers in Energy Engineering*, K. Mima, G. L. Kulcinski, and W. Hogan, eds., *Proc. SPIE* **3886**, pp. 481–488, 2000.

[47] Y. Ochi, K. Fujita, I. Niki, H. Nishimura, N. Izumi, A. Sunahara, S. Naruo, T. Kawamura, M. Fukao, H. Shiraga, H. Takabe, S. Mima, K. Nakai, I. Uschmann, R. Butzbach, and E. Förster, "Time- and space-resolved x-ray spectroscopy for observation of the hot compressed core region in a laser driven implosion," *J. Quant. Spect. Rad. Trans.* **65**, pp. 393–404, 2000.

[48] M. Tabak, J. Hammer, M. E. Glinsky, W. L. Kruer, S. C. Wilks, J. Woodworth, E. M. Campbell, M. D. Perry, and R. J. Mason, "Ignition and high gain with ultrapowerful lasers," *Phys. Plasmas* **1**, pp. 1626–1634, 1994.

[49] Lord Rayleigh, "Investigation of the character of the equilibrium of an incrompressible heavy fluid of variable density," *Proc. London Math. Soc.* **14**, pp. 170–177, 1883.

[50] G. I. Taylor, “The instability of liquid surfaces when accelerated in a direction perpendicular to their planes. I,” *Proc. Royal Soc. (London)* **A 201**, pp. 192–196, 1950.

[51] H. J. Kull, “Rayleigh–Taylor instability: Modes and nonlinear evolution,” *Laser Part. Beams* **4**, pp. 473–493, 1986.

[52] S. Chandrasekhar, *Hydrodynamic and Hydromagnetic Stability*, Oxford University Press, Glasgow, 1961.

[53] D. H. Munro *Phys. Rev. A* **38**, p. 1433, 1988.

[54] S. Bodner, “Rayleigh–Taylor instability and laser-pellet fusion,” *Phys. Rev. Lett.* **33**, pp. 761–764, 1974.

[55] H. Takabe, K. Mima, L. Montierth, and R. L. Morse, “Self-consistent grwoth rate of the Rayleigh-Taylor instability in an ablatively accelerated plasma,” *Phys. Fluids* **28**, pp. 3676–3682, 1985.

[56] J. D. Kilkenny, S. G. Glendinning, S. W. Haan, B. A. Hammel, J. D. Lindl, B. A. Remington, S. V. Weber, J. P. Knauer, and C. P. Verdon *Phys. Fluids* **1**, p. 1379, 1964.

[57] R. Betti, V. N. Goncharov, R. L. McGrory, P. Sorotokin, and C. P. Verdon, “Self-consistent stability analysis of ablation fronts in inertial confinement fusion,” *Phys. Plasmas* **3**, p. 2122, 1996.

[58] K. Shigemori, H. Azechi, M. Nakai, M. Honda, K. Meguro, N. Miyanaga, H. Takabe, and K. Mima, “Measurement of Rayleigh–Taylor growth rate at planar targets in direct drive by partially coherent light,” *Phys. Rev. Lett.* **78**, pp. 250–253, 1997.

[59] B. A. Remington, S. W. Haan, S. G. Glendinning, J. D. Kilkenny, D. H. Murno, and R. J. Walance, “Large growth Rayleigh–Taylor experiments using shaped laser pulses,” *Phys. Rev. Lett.* **67**, pp. 3259–3262, 1991.

[60] S. Nakai, K. Mima, T. Yamamanaka, Y. Izawa, Y. Kato, K. Nishihara, H. Azechi, N. Miyanaga, H. Takabe, T. Sasaki, M. Nakatsuka, M. Yamanaka,

T. Kado, R. Kodama, A. Nishiguchi, T. Kanabe, and C. Yamanaka, “Fermi degeneracy of high density imploded plasma and stability of hollow shell pellet implosion,” *Plasma Physics and Controlled Nuclear Fusion Research* **III**, p. 13, 1992.

[61] H. Azechi, M. Nakai, K. Shigemori, N. Miyanaga, H. Shiraga, H. Nishimura, M. Honda, R. Ishizaki, J. G. Wouchuk, H. Takabe, K. Mima, A. Nishiguchi, and T. Endo, “Direct-drive hydrodynamic instability experiments on the GEKKO XII laser,” *Phys. Plasmas* **4**, pp. 4079–4089, 1997.

[62] H. Takabe *et al.*, “Sclaing of implosion experiments for high neutron yield,” *Phys. Fluids* **10**, pp. 2884–2893, 1988.

[63] M. Nakatsuka, H. Azechi, H. Shiraga, H. Nishimura, T. Kanabe, N. Miyanaga, M. Nakai, H. Fujita, T. Jitsuno, and K. Fujita, “The HIPER project report,” in *Annual Progress Report*, pp. 18–21, Institute of Laser Engineering, Osaka University, 1998.

[64] Glendinning *et al.*, “Measurement of a dispersion curve for linear-regime Rayleigh–Taylor growth rates in laser-driven planar targets,” *Phys. Rev. Lett.* **78**, pp. 3318–3321, 1997.

[65] B. Yaakobi, D. Shvarts, F. J. Mashall, R. Epstein, and Q. Su, “Target imaging and backlighting diagnosis,” *Rev. Sci. Instr.* **66**, pp. 731–733, 1995.

[66] B. Yaakobi, D. Shvarts, R. Epstein, and Q. Su, “X-ray backlighting imaging of mixed imploded targets,” *Laser and Particle Beams* **14**, pp. 81–91, 1996.

[67] J. C. Dainty and R. Shaw, *Image Science*, Academic Press, New York, 1994.

[68] J. Silk, “Characterization of the effects of scattering on imaging x-ray optics performance,” *SPIE Proceedings* **257**, 1980.

[69] J. Morse, “Detectors for synchrotron radiation,” in *Theory, Instruments and Methods*, J. Baruchel, J.-L. Hodeau, M. S. Lehmann, J.-R. Regnard, and C. Schlenker, eds., vol. I of *Neutron and Synchrotron Radiation for Condensed Matter Studies*, ch. VI, pp. 95–112, Springer-Verlag & Les Editions de Physique, 1993.

[70] M. Born and E. Wolf, *Principles of Optics*, Pergamon Press, Oxford, 1993.

[71] W. H. Bragg and W. L. Bragg, “The reflection of x-rays by crystals,” *Proc. Roy. Soc.* **A88**, p. 429, 1913.

[72] M. von Laue, “Interferenzerscheinungen bei Röntgenstrahlen,” *Ann. der Physik* **41**, p. 989, 1913.

[73] T. Mißalla, *Hochauflösende lichtstarke Röntgenspektroskopie laserproduzierter Plasmen*. PhD thesis, Friedrich-Schiller-Universität, Jena/Germany, 1997.

[74] M. Dirksmöller, *Einzel- und Doppelkristallanordnungen zur hochauflösenden röntgenoptischen Abbildung*. PhD thesis, Friedrich-Schiller-Universität, Jena/Germany, 1996.

[75] K. Schwarzschild, “Untersuchungen zur geometrischen Optik.,” *Abhandlungen der königlichen Gesellschaft der Wissenschaften zu Göttigen* **4**(1 & 2), 1905.

[76] Y. Aglitskiy, T. Lehecka, S. Obenschein, S. Bodner, C. Pawley, K. Gerber, J. Sethian, C. Brown, J. Seely, U. Feldmann, and G. Holland, “High resolution monochromatic x-ray imaging system based on spherically bent crystals.,” *Applied Optics* **37**, pp. 525–533, 1998.

[77] Y. Aglitskiy, T. Lehecka, S. Obenschain, C. Pawley, C. M. Brown, and J. Seely, “X-ray crystal imagers for inertial confinement fusion experiments,” *Rev. Sci. Instr.* **70**, pp. 530–535, 1999.

[78] S. A. Pikuz, T. A. Shelkovenko, V. M. Romanova, D. A. Hammer, A. Y. Faenov, V. A. Dyakin, and T. A. Pikuz, “High-luminosity monochromatic x-ray backlighting using an incoherent plasma source to study extremely dense plasmas,” *Rev. Sci. Instrum.* **68**, pp. 740–744, 1997.

[79] M. Sanchez del Rio, A. Y. Faenov, V. M. Dyakin, T. A. Pikuz, S. A. Pikuz, V. M. Romanova, and T. A. Shelkovenko, “Ray-tracing for a monochromatic x-ray backlighting scheme based on spherically bent crystals,” *Physica Scripta* **55**, pp. 735–740, 1997.

[80] C. J. Pawley, S. E. Bodner, J. P. Dahlburg, S. P. Obenschain, A. J. A. J. Schmitt, J. D. J. D. Sethian, C. A. Sullivan, J. H. Gardner, Y. Aglitskiy, Y. Chan, and

T. Lehecka, “Observation of Rayleigh–Taylor growth to short wavelengths on Nike,” *Phys. Plasmas* **6**, pp. 565–570, 1999.

[81] M. Dirksmöller, O. Rancu, I. Uschmann, P. Renaudin, C. Chenais-Popovics, J. Gauthier, and F. E., “Time resolved x-ray monochromatic imaging of laser-produced plasma at 0.6635 nm wavelength,” *Optics Communications* **118**, pp. 379–387, 1995.

[82] D. Taupin, *Théorie dynamique de la diffraction des rayons X par les cristeaux déformés*. PhD thesis, Faculté des Sciences de l’Université de Paris Centre d’Orsay, 1964.

[83] S. Takagi *Acta Cryst.* **15**, p. 1311, 1962.

[84] D. Taupin, “Théorie dynamique de la diffraction des rayons X par les cristeaux déformes,” *Bull. Soc. franc. Miner. Crist.* **87**, pp. 469–511, 1964.

[85] F. Chukhovskii, W. Z. Chang, and E. Förster, “X-ray focussion optics. i+ii.,” *J. Appl. Phys.* **77**, pp. 1843–1845, 1995.

[86] M. Krisch, *Spektrale und fokale Eigenschaften von gebogenen Bragg-Kristallen*. PhD thesis, Universität Dortmund/Germany, 1993.

[87] K. Gäbel, *Hochauflösende Röntgenspektroskopie und mikroskopie mit gebogenen Kristallen im Wellenlängenbereich* < 1 *nm*. PhD thesis, Jena University, 1991.

[88] I. Uschmann. private communication.

[89] K. Fujita, *Investigation of implosion stability with x-ray spectroscopic methode*. PhD thesis, Osaka University, 1998.

[90] M. Laerz. private communication.

[91] M. Vollbrecht, *Einsatz und Weiterentwicklung von gebogenen Kristallen zur Plasmadisgnose im Wellenlängenbereich von 0,3–2,66 nm*. PhD thesis, Friedrich-Schiller-Universität Jena, 1998.

[92] R. Guenter, *Modern Optics*, John Wiley & Sons, 1990.

[93] T. Hahn, ed., *International Tables for Crystallography*, Kluwer Academic Publishers, Dorndrecht/Boston/London, 1989.

[94] V. Honkimäki, J. Sleight, and P. Suortti, "Characteristic x-ray flux from sealed Cr, Cu, Mo, Ag, and W tubes," *J. Appl. Cryst.* **23**, p. 412, 1990.

[95] H. Kuchling, *Taschenbuch der Physik*, Verlag Harry Deutsch, 1986.

[96] W. H. Zachariasen, *Theory of X-ray diffraction in crystals*, Dover Publ., New York, 1945.

[97] K. Fujita. private communication.

[98] S. Sebban, H. Daido, N. Sakaya, T. Norimatsu, T. Jitsuno, K. Mima, Y. Kato, S. Wang, Y. Gu, G. Huang, H. Tang, K. Murai, A. Klisnik, P. Zeitoun, R. Butzbach, I. Uschmann, M. Vollbrecht, E. Förster, G. Zhang, T. Desai, H. Takenaka, and F. Koike, "Studies on collisional pumping of soft x-ray laser at ILE," *IEEE J. Sel. Top. Quant. Elect.* **5**, pp. 1460–1468, 2000.

[99] B. MacGowan, S. Maxon, R. A. London, D. L. Matthews, and D. A. Whelan, "Soft x-ray amplification at 50.3 å in nickellike ytterbium," *J. Opt. Soc. Am. B* **5**, pp. 1858–1863, 1988.

[100] H. Daido, S. Sebban, N. Sakaya, Y. Tohyama, T. Norimatsu, K. Mima, Y. Kato, S. Wang, Y. Gu, G. Huang, H. Tang, K. Murai, R. Butzbach, I. Uschmann, M. Vollbrecht, and E. Förster, "Experimental characterization of short wavelength Ni-like soft x-ray lasers towards the water window," *J. Opt. Soc. Amer. B* **16**, pp. 2295–2299, 1999.

[101] C. D. Decker and R. A. London, "Design for a compact Ni-like-tungsten x-ray laser," *Phys. Rev. A* **57**, pp. 1395–1399, 1998.

[102] G. Yuan, K. Murai, H. Daido, R. Kodama, and Y. Kato, "Two dimensional beam characteristics of triple-pulse pumping Ne-like Ge soft x-ray laser at 19.6 nm," *Phys. Rev. A* **52**, pp. 4861–4866, 1995.

[103] J. Nilsen, B. J. MacGowan, L. B. Da Silva, and J. C. Moreno, "Prepulse technique for producing low-z Ne-like x-ray laser," *Phys. Rev. A* **48**, pp. 4682–4685, 1993.

[104] C. G. F., C. L. S. Lewis, M. J. Lamb, A. G. MacPhee, D. Neely, P. Norreys, M. H. Key, S. B. Healy, P. Holden, G. J. Pert, G. J. Plowes, J. A. andTallens, and A. Demir, “Using low and high prepulses to enhance the $j = 0 - 1$ transition at 19.6 nm in the Ne-like germanium XUV laser,” *Opt. Commun.* **123**, pp. 777–789, 1996.

[105] M. Nantel, A. Klisnick, G. Jamelot, P. B. Holden, B. Rus, A. Carillon, P. Jaeglé, P. Zeitoun, G. Tallents, A. G. MacPhee, C. L. S. Lewis, S. Jacquemont, and L. Bonnet, “Spectroscopic characteriazation of prepulsed x-ray laser plasmas,” *Phys. Rev. E* **54**, pp. 2852–2862, 1996.

[106] P. H. Heckmann and E. Träbert, *Introduction to the Spectroscopy of atoms*, North-Holland Press, 1989.

[107] S. Fritzsche and Dong, *Wavelengths and transition probabilities of* $3d^9\ 4f\ (J = 1)$ – $3d^{10}\ (J = 0)$ *transition in Ni–like Yb, Hf, Ta and W ions*. Internal report, University of Kassel, Kassel, Germany, 1999.

[108] P. Quinet and E. Biémont, “Transition rates and wavelengths in the x-ray spectra of nickel-like ions (Ag XX–Pb LV),” *Physica Scripta* **43**, pp. 150–157, 1991.

[109] H. L. Zhang, D. H. Sampson, and C. J. Fontes, “Relativistic distorted-wave collision strengths and oscillator strengths for the 33 Ni-like ions with $60 \leq Z \leq 92$,” *Atomic Data and Nuclear Data Tables* **48**, pp. 91–163, 1991.

[110] A. Zigler, H. Zmora, N. Spector, M. Klapisch, J. L. Schwob, and A. Bar-Shalom, “Identification of the spectra of Hf XLV, Ta XLVI, W XLVII, and Re XLVIII isoelectronic to Ni I in laser-produced plasmas,” *J. Opt. Soc. Am.* **70**, pp. 129–131, 1980.

[111] B. H. Armstrong and R. W. Nicholls, *Emission, Absorption and Transfer of Radiation in Heated Athmospheres*, Pergamon Press, Oxford, 1972.

[112] G. D. Tsakiris and K. Eidmann, “An approximate methode for calculating planck and rossland mean opacities in hot, dense plasmas,” *J. Quant. Spectrosc. Radiat. Transfer* **38**, pp. 353–368, 1987.

[113] Los Alamos National Laboratory, *TOPS – Code for the Calculation of Opacities,* (`http://www.t4.lanl.gov/cgi-bin/opacity/tops.pl`), 2000.

[114] H. H. Johann, "Die Erzeugung lichtstarker Röntgenspektren mit Hilfe von Konkavkristallen," *Z. Phys.* **69**, pp. 185–206, 1931.

[115] T. Johannsson, "Über ein neuartiges, genau fokussierendes Röntgenspektrometer," *Z. Phys.* **82**, pp. 507–528, 1933.

[116] Y. Cauchois *R. C. Acad. Sci. Paris* **223**, p. 82, 1946.

[117] A. Y. Faenov, I. Y. Skobelev, S. A. Pikuz, G. A. Kyrala, R. D. Fulton, J. Abdallah, Jr., and D. P. Kilcrease, "High-resolution x-ray spectroscopy of a subpicosecond-laser-produced silicon plasma," *Phys. Rev. A* **51**, pp. 3529–3533, 1995.

[118] A. Y. Faenov, B. A. Bryunetkin, V. M. Dyakin, T. A. Pikuz, I. Y. Skobelev, S. A. Pikuz, J. Nilsen, A. L. Osterheld, and U. I. Safronova, "High-resolution measurement of Mg XII and Cu XX resonance and satellite transitions and the resonance defect in the Mg-pumped Cu x-ray laser scheme," *Phys. Rev. A.* **52**, pp. 3644–3650, 1995.

[119] M. Bitter, K. W. Hill, A. L. Roquemore, P. Beiersdorfer, S. M. Kahn, S. R. Elliott, and B. Fraenkel, "Imaging x-ray crystal spectrometers for the National Spherical Torus Experiment," *Rev. Sci. Instrum.* **70**, pp. 292–295, 1999.

[120] B. K. F. Young, A. L. Osterheld, D. F. Price, R. Shepherd, R. E. Stewart, A. Y. Faenov, A. I. Magunov, T. A. Pikuz, I. Y. Skobelev, F. Flora, S. Bollanti, P. Di Lazzaro, T. Letardi, A. Grilli, L. Palladino, A. Reale, A. Scafati, and L. Reale, "High-resolution x-ray spectrometer based on spherically bent crystals for investigations of femtosecond plasmas," *Rev. Sci. Instr.* **69**, pp. 4049–4053, 1998.

[121] E. Förster, K. Gäbel, and I. Uschmann, "X-ray microscopy of laser-produced plasmas with the use of bent crystals," *Laser and Particle Beams* **9**, pp. 135–148, 1991.

[122] R. J. Dejus and M. Sanchez del Rio, “XOP: A graphical user interface for spectral calculations and X-ray optics utilities,” *Rev. Sci. Instrum.* **67**, p. 3359, 1996.

[123] M. Sanchez del Rio and R. J. Dejus, “XOP: A multiplatform graphical user interface for synchrotron radiation spectral and optics calculations,” *SPIE proceedings* **3152**, pp. 148–157, 1997.

[124] M. Sanchez del Rio and R. J. Dejus, “XOP: Recent developments,” *SPIE proceedings* **3448**, pp. 340–345, 1998.

[125] D. Cullen *Nucl. Instr. and Meth. in Phys. Res.* **B101**, pp. 499–510, 1995.

[126] R. E. Kelly, “Atomic and ionic spectrum lines below 2000 angstroms: Hydrogene through krypton, part i,” *Journal of Physical and Chemical Reference Data* **16**, 1987. Supplement No. 1.

[127] W. H. Press *et al.*, *Numerical Recipes in C*, Cambridge University Press, 1989.

[128] H. Daido, S. Ninomiya, M. Takagi, Y. Kato, and F. Koike, “Wavelength measurements of the Ni-like soft x-ray lasing lines and their comparison to the atomic physics calculation,” *J. Opt. Soc. Am. B* **16**, pp. 296–300, 1999.

[129] F. Parpia, F. Fischer, and I. P. Grant *Comp. Phys. Commun.* **94**, p. 249, 1996.

[130] K. G. Dyall, I. P. Grant, C. T. Johnson, F. A. Parpia, and E. P. Plummer *Comp. Phys. Commun.* **55**, p. 425, 1998.

[131] P. Gibbon, 2000. private communication.

[132] J. P. Christiansen, D. E. T. F. Ashby, and K. V. Roberts, “MEDUSA: A one-dimensional laser fusion code,” *Computer Phys. Comm.* **7**, pp. 271–287, 1974.

Ehrenwörtliche Erklärung der Selbstständigkeit

Ich erkläre hiermit ehrenwörtlich, daß ich die vorliegende Arbeit selbstständig, ohne unzulässige Hilfe Dritter und ohne Benutzung anderer als der angegebenen Hilfsmittel und Literatur angefertigt habe. Die aus anderen Quellen direkt oder indirekt übernommenen Daten und Konzepte sind unter Angabe der Quelle gekennzeichnet.

Bei der Auswahl und Auswertung folgenden Materials haben mir die nachstehend aufgeführten Personen in der jeweils beschriebenen Weise unentgeltlich geholfen:

Eckhart Förster: Themenstellung, Auswahl von Literatur, Diskussion, Verbesserungsvorschläge zur Dissertation

Hiroaki Nishimura: Themenstellung (Rayleigh-Taylor Instabilities), Auswahl von Literatur, Diskussion

Hiroyuki Daido: Themenstellung (Röntgenlaser), Auswahl von Literatur, Diskussion

Yoshiaki Kato: Diskussion

Ingo Uschmann: Einführung in die Themen, Auswahl von Literatur, Diskussion, Hilfe bei der Konstruktion des HIPER Kristalls

Manfred Lärz: Konstruktion der Instrumente

Markus Vollbrecht: Konstruktion des Spektrometers

Joseph Nilsen: Literaturhinweise

Kazuhisa Fujita: Gemeinsame Auswertung und Diskussion

Stéphan Sebban: Einführung in Röntgenlaser

Stephan Fritzsche: Vorschlag und Einführung zur Temperaturbestimmung, Berechnung der gf-Faktoren, Diskussion

Fumihiro Koike: Berechnung der gf-Faktoren, Diskussion

Ortrud Wehrhan: Einführung in die Kristallographie, Diskussion

Paul Gibbon: Einführung in den Medusa-Simulationscode, Diskussion der plasmaphysikalischen Ergebnisse

Weitere Personen waren an der inhaltlich-materiellen Erstellung der vorliegenden Arbeit nicht beteiligt. Insbesondere habe ich hierfür nicht die entgeltliche Hilfe von Vermittlungs- bzw. Beratungsdiensten (Promotionsberater oder andere Personen) in Anspruch genommen. Niemand hat von mir unmittelbar oder mittelbar geldwerte Leistungen für Arbeiten erhalten, die im Zusammenhang mit dem Inhalt der vorgelegten Dissertation stehen.Die Arbeit wurde bisher weder im In- noch im Ausland in gleicher oder ähnlicher Form einer anderen Prüfungsbehörde vorgelegt.

Die geltende Promotionsordnung der Physikalisch-Astronomischen Fakultät ist mir bekannt.

Ich versichere ehrenwörtlich. daß ich nach besten Wissen die reine Wahrheit gesagt und nichts verschwiegen habe.

Jena, 23. Oktober 2000

Curriculum Vitae

Name:	Randolf Butzbach	
Birthday, -place:	February 16, 1969	Kassel, Germany
Nationality:	German	
Personal status:	single	
School education:	1975–1979	Auefeldschule Kassel (Grundschule)
	1979–1986	Carl-Schomburg-Schule Kassel (Realschule)
	1986–1989	Jacob-Grimm-Schule Kassel (Gymnasium)
Abitur:	May 19, 1989	
Civil service:	1989–1990	
University education:	1990–1996	University of Kassel Principal subject: Physics
	June 27, 1996	Degree: Diplom-Physiker (Dipl.-Phys.)
Diplomarbeit: (Master thesis)	"*Development of Thin Crystal Monochromators: The Influence of Crystal Thickness on the Tails of the Rocking Curve*" at the European Synchrotron Radiation Facility, ESRF, Grenoble/France (on own initiative)	

Employment:	
1992–1995	Employment at an engineer office as self-responsible software-engineer for commercial software
1995–1996	Employment at the European Synchrotron Radiation Facility in Grenoble/France
1997–2000	Employment as Wiss. Mitarbeiter (Scientific Collaborator, PhD Position) at the X-Ray Optics Group at the Institute of Optics and Quantum Electronics at the University of Jena/Germany, in collaboration with the Institute of Laser Engineering, ILE, at the University of Osaka/Japan.
Stays abroad:	– France (18 months) – Japan (11 months)
Languages:	German, English, French, Modern-Greek – each in speech and writing; some basics in Japanese
Awards:	ILE-Prize for the best scientific work in 1998

Jena, 23. Oktober 2000

Acknowledgments

First of all, honor to whom honor is due, thanks to the almighty God, the creator of heaven and earth and light and atoms and who has always guided my life, for the peek in the interrelations of His wonderful creation, which we will never completely understand.

I like to thank my parents who rendered possible my studies of physics as well as Eckhart Förster, Hiroaki Nishimura, and Hiroyuki Daido who proposed this interesting subjects and for many fruitful discussions.

The many helpful discussions with Ingo Uschmann, as well as his help in many ways, were a great pleasure for which I like to express my sincere thanks.

Very heartily thanks go to Diethard Klöpfel for his help in technical problems and particularly for his moral support during this work.

I am greatful to Markus Vollbrecht who undertook with great competence the design of the spectrometer during the phase of writing his thesis while I was a beginner in this field.

Manfred Lärz undertook then the mechanical construction of the instruments for which I am very greatful.

The assistance in the experimental campaign of Kazuhisa Fujita and Jiro Funakura is greatfully acknowledged.

I am indebted to Stephan Fritzsche and Fumihiro Koike who explained me the required atomic physics and calculated for me the transition wavelengths and gf–factors.

A special thank goes to the workshops of the University of Jena, who built the instruments used in this work in an extremely short time. I appreciate it very much that they set the instruments of this work on the highest priority while delaying all the other orders in order to prepare the required instruments in time.

I also would like to thank all the ILE staff for their hospitality and help in many problems. Furthermore I like to thank all the numerous colleagues from China, France, Korea, India, and Japan, who contributed with their special skills to the here presented experimental campaigns. Without their contribution, this work would not be possible.

Once again, I would like to thank Ortrud Wehrhan, Elke Andersson, Jörg Tschischgale, Ulrich Wagner, and Paul Gibbon who made the stay in Jena a pleasure.

I also wish to express my thanks to the Deutsche Forschungsgemeinschaft who made this work possible.

Last but not least, it is a great pleasure for me to express my sincere thanks to Cecília, who gave me the motivation, strength, and energy in a very disappointing and frustrating phase of this work. To say it with Tang-san's words (Thank you very much, Tang-san!): "Take it easy that all your experiments failed...! At least, you have found *her*..."